FEDERAL UNIVERSITY OF SANTA MARIA
CENTRE OF TECHNOLOGY
ELECTRICAL ENGINEERING
GRADUATE PROGRAM

André Jaques Ramos

VERTICAL AXIS WIND TURBINE CONTROL SYSTEM

Santa Maria, RS, Brazil
2018

André Jaques Ramos

VERTICAL AXIS WIND TURBINE CONTROL SYSTEM

Thesis presented to the Master Course of the Electrical Engineering Graduate Program, in the Energy Processing Area, of the Federal University of Santa Maria (UFSM-RS), in partial fulfillment of the requirements for the **Masters Degree in Electrical Engineering**.

Advisor: Prof. Humberto Pinheiro, Ph.D.

Santa Maria, RS, Brazil
2018

Ficha catalográfica elaborada através do Programa de Geração Automática
da Biblioteca Central da UFSM, com os dados fornecidos pelo(a) autor(a).

Jaques Ramos, André
Vertical Axis Wind Turbine Control System / André Jaques Ramos - 2018
119 p.; 30 cm

Orientador: Humberto Pinheiro
Dissertação (Mestrado) – Universidade Federal de Santa Maria, Centro de Tecnologia, Programa de Pós-Graduação em Engenharia Elétrica, RS, 2018

1.Electric Engineering 2. Vertical Axis Wind Turbine 3. Coefficient of Power 4. Permanent Magnet Synchronous Machine 5. Rotational Speed Obsever I. Pinheiro, Humberto. II. Title.

Endereço: Rua Dona Luiza, Nº 183, Bairro Rosário, Santa Maria, RS, Brasil, CEP: 97010-160;
Fone: (55) 3217-2391; Celular: (55) 99903-2826;
Endereço Eletrônico: jaquesramos92@hotmail.com.

André Jaques Ramos

VERTICAL AXIS WIND TURBINE CONTROL SYSTEM

Dissertação apresentada ao Curso de Mestrado do Programa de Pós-Graduação em Engenharia Elétrica, Área de Concentração em Processamento de Energia, da Universidade Federal de Santa Maria (UFSM), como requisito parcial para obtenção do grau de **Mestre em Engenharia Elétrica**.

Aprovado em 30 de Novembro de 2018:

Humberto Pinheiro, Ph.D. (UFSM)
(Presidente/ Orientador)

Carlos Eduardo de Souza, Dr. (UFSM)

Rodrigo Zelir Azzolin, Dr. (FURG) - Videoconferência

Claiton Moro Franchi, Dr. (UFSM) (Suplente)

Santa Maria, RS, Brasil
2018

DEDICATION

To my father, Walter Luiz Santos Ramos, my mother, Lúcia Jaques Ramos and my sister, Denise Jaques Ramos.

ACKNOWLEDGEMENTS

First of all, I would like to thank my family, for supporting and embracing me in tough moments, my advisor, Professor Humberto Pinheiro, Ph.D., with whom I have learnt a lot about engineering and professional behaviour, to Professors Carlos Eduardo Souza, Dr., Claiton Moro Franchi, Dr., and Frederico Menine Schaf, Dr., for helping me with aerodynamics, instrumentation and data communication aspects, and finally, my classmates, colleagues and friends from the university, for each and every discussion during this period of work.

This study was partially financed by the Coordination of Superior Level Staff Improvement - Brazil (CAPES/PROEX) - Finance Code 001.

“Nunca se prepare quando você precisa estar pronto - **Ricardo Silva Voz**”

RESUMO

SISTEMA DE CONTROLE PARA TURBINA EÓLICA DE EIXO VERTICAL

Autor: André Jaques Ramos
Orientador: Humberto Pinheiro

Esta dissertação apresenta o desenvolvimento de um sistema de controle para uma turbina eólica de eixo vertical com o objetivo de extrair seu máximo desempenho. São revisados os tipos de turbinas de eixo vertical e maneiras de integrá-las ao meio urbano. Também é apresentado um estudo sobre as estratégias existentes para melhorar a eficiência destes aerogeradores. Modelagem e simulação aerodinâmica usando *blade element momentum method* são realizadas para compreender as forças e velocidades que atuam sob rotor e sua influência no desempenho da turbina. A turbina eólica sob teste conta com uma máquina síncrona de ímãs permanentes com capacidade de gerar até 1.5 kW de potência. Para controlar a turbina em seu melhor desempenho, um algoritmo para extração da máxima potência é utilizado em conjunto com um conversor DC-DC. Para testes experimentais o conversor alimentará cargas resistivas. Ainda, devido a impossibilidade do uso de sensores mecânicos para aferir a rotação da máquina síncrona, dois observadores de estados são empregados: um por modos deslizantes para estimar as correntes de fase, e também, um observador adaptativo para a força eletromotriz da máquina; resultando na observação da rotação. Os resultados de simulação são comparados com dados do fabricante e testes experimentais.

Palavras-chave: Coeficiente de potência, Máquina Síncrona de Imãs Permanentes, Observador de Rotação, Turbina Eólica de Eixo Vertical.

ABSTRACT

VERTICAL AXIS WIND TURBINE CONTROL SYSTEM

Author: André Jaques Ramos
Advisor: Humberto Pinheiro

This master thesis presents the development of a control system to vertical axis wind turbine in order to harnessing its maximum performance. Vertical axis turbine designs and how they could be integrated with urban area are studied, together with a review in literature about methods that aim to improve its coefficient of power and start up condition under very low winds. The turbine in test can generate 1.5 kW employing a permanent magnet synchronous machine. In order to extract the maximum performance is used a DC-DC converter in combination with maximum power point tracking algorithm. The converter supplies a resistive load for experimental tests. Due to the rotor be unreachable, there was no way to measure rotor speed, so that, one current sliding mode observer and an adaptive electromotive force observer are combined resulting in rotor speed estimation. Besides, modelling and simulation aspects about rotor velocities and forces using blade element momentum method are presented to understand its behaviour and how they affect the turbine performance. This analysis is compared with manufacturer data and experimental results.

Keywords: Coefficient of Power, Permanent Magnet Synchronous Machine, Rotational Speed Observer, Vertical Axis Wind Turbine.

LIST OF FIGURES

LIST OF TABLES

LIST OF ABBREVIATES AND INITIALS

BEM	Blade Element Momentum
CFD	Computational Fluid Dynamic
CP	Coefficient of Power
DMSTM	Double Multiple Streamtube Model
DSP	Digital Signal Processor
EMF	Electromotive Force
GWEC	Global Wind Energy Council
HAWT	Horizontal Axis Wind Turbine
IEC	International Electrotechnical Commission
MPPT	Maximum Power Point Tracking
NACA	National Advisory Committee for Aeronautics
PI	Proportional-Integral
PMSM	Permanent Magnet Synchronous Machine
PWM	Pulse Width Modulation
RMS	Root Mean Square
RPM	Rotational Per Minute
SMO	Sliding Mode Observer
TSR	Tip Speed Ratio
VAWT	Vertical Axis Wind Turbine
VGOT	Variable Geometry Oval Trajectory

LIST OF SYMBOLS

A_M	Berg's gain
C	Capacitance
C_p	Power coefficient
C_t	Thrust coefficient
C_{torque}	Torque coefficient
D	Drag force
D_1, D_2	duty cycles 1 and 2
E	Energy
E_f	Induced voltage
F	Force
F_0	Wind force
F_n	Normal force
F_t	Thrust force
F_{t0}	Wind thrust force
F_{tan}	Tangential force
F_{torque}	Torque
F_{torque}^{ref}	Reference torque
I_L	Nominal inductor current
L	Lift force/Indutance
L_a, L_b, L_c	Stator inductances
L_d	Direct axis inductance
L_s	Stator inductance
L_q	Quadrature axis inductance
K	Optimal constant
K_e	Back electromotive force
M_{ab}, M_{bc}, M_{ca}	Mutual inductance between stator phases
N_{blade}	Number of blades
N_{st}	Number of streamtubes
N_θ	Number of $\theta's$
P	Power
P_0	Wind Power
P_{cap}	Power available in capacitor
P_{cl}	Cooper loses
P_{em}	Electromechanical power
P_{in}	Input power
P_{out}	Output power
P_{wt}	Generated wind power
Q	Adaptive observer gain
R	Resistence
R_s	Stator resistance

S	Blade's leading/trailing edge velocity square root
T_{em}	Electromechanical torque
T_s	Sample time
V	Lyapunov function
V_G	Nominal rectifier voltage
V_{dc}	Nominal capacitor voltage
V_f	RMS line voltages
V_{out}	Output voltage
a	Induction factor
a_1	Upstream induction factor
a_2	Downstream induction factor
a_c	Auxiliary constant
c	Chord length
c_d	Drag coefficient
c_d^{dyn}	Drag coefficient - Dynamic stall
c_l	Lift coefficient
c_l^{dyn}	Lift coefficient - Dynamic stall
c_l^{mod}	Lift coefficient - Berg modicifafion
$c_{l\alpha}$	Slope of lift coefficent curve
d	Duty cycle
$\tilde{d_1}, \tilde{d_2}$	Small signal duty cycles 1 and 2
e_{vdc}	Voltage error
e_{iL}	Current error
e_α	Alpha axis electromotive force
e_β	Beta axis electromotive force
f	Frequency
f_s	Switching frequency
h	Blade length
h_1, h_2, h_3	Positive gains
i	Auxiliary variable
i_c	Capacitor current
i_L	Inductor current
i_L^{ref}	Reference current
i_{Load}	Load current
i_a, i_b, i_c	Stator currents
i_d	Direct axis current
i_q	Quadrature axis current
i_α	Alpha axis current
i_β	Beta axis current
$\tilde{i_L}$	Small signal inductor current
j	Auxiliary variable
m	Mass flux/slope
n	Rotation

p_0	Freestream preassure
p_{dw}	Downstream pressure
p_e	Rotor midlle preassure
p_{up}	Upstream pressure
p_w	Wake pressure
pp	Pole pairs
r	Radius
t	Time
s_0	Freestream area
s_a, s_b, s_c, s_d	IGBT switches
s_{dw}	Downstream area
s_e	Rotor middle area
s_j	j_{th} sliding surface
s_{rotor}	Rotor area
s_{st}	Streamtube area
s_{up}	Upstream area
s_w	Wake region area
v_0	Wind speed at freestream
v_G	Rectifier output voltage
v_L	Inductor voltage
v_a, v_b, v_c	Stator voltages
v_d	Direct axis voltage
v_{dc}	capacitor voltage
v_{dw}	Downstream wind speed
v_e	Rotor wind speed
v_{ind}	Induced velocity
v_{ind1}	Upstream induced velocity
v_{ind2}	Downstream induced velocity
v_{Load}	Load voltage
v_{rel}	Relative velocity
v_q	Quadrature axis voltage
v_{up}	Upstream wind speed
v_w	Wake wind speed
v_{wind}	Wind speed
v_x	Velocity at x-axis
v_y	Velocity at y-axis
v_α	Alpha axis voltage
v_β	Beta axis voltage
$\tilde{v_{dc}}$	Small signal capacitor voltage
$\tilde{v_G}$	Small signal rectifier voltage
w_{cut1}	Low pass filter cutoff frequency 1
w_{cut2}	Low pass filter cutoff frequency 2
x	x-axis displacement

Δp_e	Rotor pressure variation
ΔE_{Labc}	Stator inductance energy ratio
$\Delta\theta$	Azimuthal angle interval
α	Angle of attack
α_0	Zero lift angle of attack
α_{eff}	Effective angle of atack
α_{ref}	Reference angle of attack
α_{ss}	Stall angle of attack
β	Flight path angle
$\delta\alpha$	Histeresis delay
θ	Azimuthal angle
θ_e	Electrical angular position
$\hat{\theta}_e$	Observed angular position
σ	solidity
ρ	Air density
ω	Angular velocity
ω_e	Electrical angular velocity
ω_m	Mechanical velocity
λ	Tip Speed Ratio
ς	Phase compensator
τ	Time constant
φ_d	Direct axis stator flux
φ_q	Quadrature axis stator flux
$\varphi_a, \varphi_b, \varphi_c$	Stator magnetic fluxes
$\varphi_a^r, \varphi_b^r, \varphi_c^r$	Rotor magnetic fluxes
φ_α	Alpha axis stator flux
φ_β	Beta axis stator flux
φ_α^r	Alpha axis rotor flux
φ_β^r	Beta axis rotor flux
φ_{pm}	Concatenated flux of magnets
Ω	Pitch angle
$\tilde{\omega_e}$	Angular velocity estimation error
$\hat{\omega_e}$	Observed electrical angular velocity
$\mathbf{A_d}$	Discrete-time dynamic matrix
$\mathbf{A_{dq}}$	dq to $\alpha\beta$ transform matrix
$\mathbf{A}_{\alpha\beta}$	abc to $\alpha\beta$ transform matrix
$\mathbf{B_d}$	Discrete-time entrance matrix
$\mathbf{I}$	Identity matrix
$\mathbf{L_{abc}}$	abc stator inductance matrix
$\mathbf{L_{dq}}$	dq stator inductance matrix
$\mathbf{L}_{\alpha\beta}$	$\alpha\beta$ stator inductance matrix
$\mathbf{M}$	Auxiliary matrix
$\mathbf{R_{abc}}$	abc stator resistance matrix

$\mathbf{R_s}$	stator resistance matrix
$\mathbf{R}_{\alpha\beta}$	$\alpha\beta$ stator resistance matrix
$\mathbf{e}_{\alpha\beta}$	$\alpha\beta$ electromotive force
$\mathbf{e}^{\mathbf{eq}}_{\alpha\beta}$	$\alpha\beta$ equivalent electromotive force
$\mathbf{e}^{\mathbf{ref}}_{\alpha\beta}$	Reference electromotive force
$\mathbf{i_{abc}}$	abc stator current matrix
$\mathbf{i_{dq}}$	dq stator current matrix
$\mathbf{i}_{\alpha\beta}$	$\alpha\beta$ stator current matrix
$\mathbf{j}$	Auxiliary matrix
$\mathbf{s}_{\alpha\beta}$	$\alpha\beta$ sliding function
$\mathbf{u}_{\alpha\beta}$	$\alpha\beta$ attraction function
$\mathbf{v_{abc}}$	abc phase voltage matrix
$\mathbf{v_{dq}}$	dq phase voltage matrix
$\mathbf{v}_{\alpha\beta}$	$\alpha\beta$ stator voltage matrix
$\hat{\mathbf{e}}_{\alpha\beta}$	Observed electromotive force
$\hat{\mathbf{i}}_{\alpha\beta}$	$\alpha\beta$ observed stator current matrix
$\tilde{\mathbf{e}_{\alpha\beta}}$	$\alpha\beta$ electromotive force error
$\tilde{\mathbf{i}_{\alpha\beta}}$	$\alpha\beta$ current estimation error
η	Auxiliary matrix
γ	Auxiliary matrix
$\varphi_{\mathbf{abc}}$	abc stator magnet flux matrix
$\varphi^{\mathbf{r}}_{\mathbf{abc}}$	abc rotor magnet flux matrix
$\varphi_{\mathbf{dq}}$	dq stator magnet flux matrix
$\varphi^{\mathbf{r}}_{\mathbf{dq}}$	dq rotor magnet flux matrix
$\varphi_{\alpha\beta}$	$\alpha\beta$ stator magnet flux matrix
$\varphi^{\mathbf{r}}_{\alpha\beta}$	$\alpha\beta$ rotor magnet flux matrix

LIST OF APPENDICES

TABLE OF CONTENTS

1 INTRODUCTION

Nowadays, wind energy is a consolidated way to produce electricity. According to Global Wind Energy Council (GWEC, 2018), the global cumulative installed capacity, until 2017, was approximately 540 MW of power. Currently, the largest market for wind power in the world is the P.R. China with around 35%, followed by the USA, Germany and India. Brazil is in the 8th position, with 13 MW, being the most relevant player in Latin America and the Caribbean.

The first wind turbine applied to generate electricity is dated from 1891 in Denmark, when Poul la Cour built a turbine to electrolyze water producing hydrogen for gas lights (MASTERS, 2004). However, since 1970's with the oil crises, European and North American countries have given financial and regulatory incentives to increase the using of greener energies such as wind, solar, biomass and so on. Since then, wind energy systems are moving from low level to the mainstream power technology (PARFIT; LEEN, 2005).

Wind farm projects can be installed onshore and offshore. In general, the areas of good wind energy resources are found far from urban centres and new transmission circuits are needed to connect these wind farms to main power grid (ANAYA-LARA et al., 2009). Recently, small wind turbines have been installed on top of buildings bringing wind energy into the cities.

Table 1.1 shows some applications of wind turbine technologies in relation to power.

Table 1.1 – Applications of wind energy.

Small ($\leq$ 10 kW)	Intermediate (10 - 500 kW)	Large ($\geq$ 500 kW)
Homes and Telecom sites	Village power	Wind power plants
Farms	Hybrid systems	Distributed power
Battery charging	Distributed systems	On/offshore wind generation

Source: Adapted from (ELLIOTT, 2002).

There is a great variety of wind turbine architectures and, over the years, most of these have already been explored (HEIER, 2008). Commercially, two designs stand out regarding axis rotation: horizontal-axis wind turbines (HAWT) and vertical-axis wind turbines (VAWT). The first ones are widely used because their power coefficient is higher ($\approx$ 0.5) compared with vertical axis wind turbine ($\approx$ 0.4) (HAMEED; AFAQ, 2013). HAWT type experiences relatively higher load at the hub. Its blades suffer less damage with cyclic aerodynamic loading, but tower shadows or yaw errors may cause dynamic stall effects to become significant, even in moderate wind (ASHWILL; SUTHERLAND; BERG, 2012). HAWT also needs a yaw mechanism to align the rotor towards wind direction.

On the other hand, VAWT have easy maintenance, simple design, their opera-

tion is independent of wind direction, they are stall regulated, so no yaw mechanism is demanded and they present higher efficiency in turbulent flow fields (KIRKE, 1998) in relation to HAWT. Besides, there are cases in which VAWT efficiency can achieve 0.6 or 0.7 (THOENNISEN et al., 2016; INSTITUTE, 2018). The main disadvantage is that, typically, it does not have the capability of self starting at low winds (BERG, 1996).

Among several VAWT designs (AMBROSIO; MEDAGLIA, 2010; TJIU et al., 2015), they are divided into two categories: lift-based and drag-based wind turbine. The main drag-based design is Savonius. Its best characteristics are the simplicity and very low noise production. It can operate with a reasonable quality at low wind speeds, because the torque is very high in those conditions (AMBROSIO; MEDAGLIA, 2010). Despite these features, its efficiency is smaller compared to Darrieus's lift-based wind turbine.

As mentioned, HAWT are widely used, mainly because of their good performance. However, recent studies have propose solutions to overcome the main Darrieus turbine difficulties, the self-starting and efficiency (KIRKE, 1998; PARASCHIVOIU; TRIFU; SAEED, 2009; SVENDSEN; MERZ, 2013; ABU-EL-YAZIED et al., 2015; SINGH; BISWAS; MISRA, 2015; ASR et al., 2016).

This master thesis presents the development of a control system to vertical axis wind turbine in order to achieve its maximum performance. Vertical axis turbine designs are studied, as well as how they could be integrated in urban areas, together with a review about methods that aim to improve their power coefficient and start up conditions under very low winds. Also, aerodynamic equations are introduced to study wind turbine velocities and forces, and how they influence turbine efficiency. The aerodynamic study contributes to design and simulate the control technique for later comparison with manufacturer data and experimental results. The objectives of this work are presented below.

1.1 OBJECTIVES

The goal of this work is to develop a control system to extract better performance of a VAWT. Also, a performance comparison among aerodynamics simulation, power electronics simulation, experimental and manufacturer data are highlighted. To understand aerodynamics and how to model VAWT behavior, a review about different types of VAWT and methods to describe velocities and forces around the rotor besides its power coefficient are introduced. Simulation with double multiple streamtube model (DMSTM) is applied to analyze these issues. Regarding power electronics, a DC-DC converter is designed and controlled in combination with a Maximum Power Point Tracking (MPPT) algorithm, which uses results from aerodynamic simulation, in order to harnessing maximum VAWT performance and obtain experimental power curve. The turbine used in this

study does not allow the installation of mechanical sensors to measure the generator's speed. Sliding mode and adaptive observers, based on the generator's phase voltages and currents, are employed to deal with this problem. These observers add reliability to the measure, because, depending on the load (inductive/capacitive) that the system supplies, the wave form of the generator's voltages and currents are going to be distorted, resulting in imprecise measurement, in case the speed is calculated by measuring voltage or current frequency. The experimental tests are made according to International Electrotechnical Commission (IEC) 61400-12-1.

The next session presents how this master thesis is organized.

1.2 WORK STRUCTURE

This thesis is divided in 7 chapters. Chapter 2 introduces a background about vertical axis wind turbines discussing their positive features, as well as drawbacks. In addition, a literature review about what has been studied in order to improve vertical axis wind turbine performance is described. Chapter 3 brings the modelling of aerodynamics of VAWT, and analyses methods to estimate their power production. A case study is presented in chapter 4, where all tested characteristics of vertical axis wind turbines are highlighted, as well as a site description. Chapter 5 presents modelling and control of PMSM and power electronic converters. Finally, chapters 6 and 7 expose the results, contributions and conclusions with a reflection about the established objectives.

2 VERTICAL AXIS TECHNOLOGY

2.1 INTRODUCTION

In this chapter, a background about vertical axis wind turbines (VAWT) is presented, discussing their positive features, as well as drawbacks. Besides, a comparison among horizontal axis wind turbine (HAWT) and new architectures of vertical axis wind turbines are presented. Finally, a literature review about what has been studied in order to improve vertical axis wind turbine performance is analyzed.

2.2 VERTICAL AXIS DEVELOPMENT

People have used the harnessing of the wind since old ages (MANWELL; MCGOWAN; ROGERS, 2010). Hence, only in the beginning of the twentieth century wind energy started to be applied for electricity generation. The first use of a wind turbine to produce electric energy is dated to 1891, by Poul la Cour in Denmark, utilizing windmills for it, as it is seen in Figure 2.1.

Figure 2.1 – Poul la Cour wind tests.

Source: (WINDPOWER.ORG, 2003).

Since then, many investments have been made in HAWT, resulting in large scale HAWT plants. On the other hand, initial researches about VAWT indicate that VAWT were not suitable for large scale electricity generation (BHUTTA et al., 2012) due to their low economical value, i.e. high specific cost of energy (TJIU et al., 2015). However, at the same time architectures of VAWT were proposed by Savonius (SAVONIUS, 1929; SAVONIUS, 1930) in 1922 and Darrieus in 1925 (DARRIEUS, 1931), respectively. Savonius wind turbines are composed by hollow cup-shaped half-cylinders fixed with a central shaft. The greatest advantage of Savonius wind turbines is their ability to self-start at low winds (AYMANE, 2017). However, the flow energy utilization of Savonius is about 20% lower than Darrieus turbine (GORELOV; KRIVOSPITSKY, 2008a). Savonius cannot rotate faster than wind, which means the turbine is not indicated to large scale power energy generation (AMBROSIO; MEDAGLIA, 2010). In Figure 2.2 an example of Savonius turbine is presented.

Darrieus wind turbines are about 40% more efficient than Savonius rotor. These turbines present low starting torque, so they are not able to start by themselves. The angle of attack changes as the turbine spins, so each blade generates its maximum torque twice at one revolution. This leads to a sinusoidal power cycle that complicates the design. Another problem arises because the majority of mass of the rotating mechanism is at the periphery rather than at the hub, as it is with a propeller. This leads to very high centrifugal stresses on the mechanism, which must be stronger and heavier to withstand them (AMBROSIO; MEDAGLIA, 2010). Different from HAWT, the independence from wind direction is what makes these turbines suitable for sites with high variance of wind direction. In Figure 2.3, the concept of Darrieus turbine is presented.

Figure 2.2 – Savonius wind turbine.

Source: (REUK, 2006).

Figure 2.3 – $4MW$ 100 metre Darrieus wind turbine.

Source: (GMP, 2017).

According to (ERIKSSON; BERNHOFF; LEIJON, 2008), during the 1970's and 1980's, vertical axis machines came back into focus when both Canada and United States built several prototypes of Darrieus turbines. The prototypes proved to be quite efficient and reliable, but the VAWTs fell victims to the poor wind energy market in the USA. The machines worked efficiently, although they had problems with fatigue of the blades, which were designed to be flex. Other important countries are Denmark and Germany that also gave crucial political support (BELLER, 2011).

Since then, many different designs have been developed. In the next section, some of them are presented, as well as how these designs could be integrated into urban regions.

2.3 DESIGNS AND CHARACTERISTICS

Based on Savonius, the Twisted Sweeney VAWT (see Figure 2.4) was proposed by Thomas Sweeney in 1973. This concept is driven by drag/lift force. Tests with this design were made by (NEMOTO; ANZAI; USHIYAMA, 2003), where different blade curvatures were tested. It was noticed that the maximum efficiency was about 0.2. (DRAGOMIRESCU, 2011) simulating its performance adding a cross section runner. As a result, an efficiency of 0.45 it was estimated even at low wind, but practical studies are needed to confirm that estimative.

Other model based on drag force is Sistan VAWT, also known as resistance type. This turbines are similar to first Persian windmills (see Figure 2.5).

Figure 2.4 – Twisted Sweeney rotor.

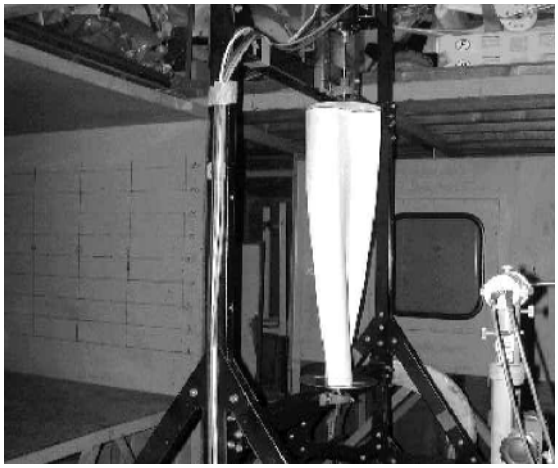

Source: (NEMOTO; ANZAI; USHIYAMA, 2003).

Figure 2.5 – Persian windmills.

Source: (AMBROSIO; MEDAGLIA, 2010).

A typical Sistan (see Figure 2.6) wind turbine is about $6m$ high and $6m$ wide with bundles of reed on typically six wind catching surfaces. The construction is rather simple with direct transmission of the force from the vertical axis onto the millstones, which are housed in a chamber below the mill. The mill's side walls have a shielding with a certain wind guiding function. Vertical axis resistance type energy converts, such as the Sistan windmill, absorb the wind energy with their individual blades, which move slower

than the wind. The differential speed generates a force which drives the blades. Such a machine is usually analyzed by assuming the rotor blades to constitute that flat plates with height to width (aspect ratio) of less than 5 (MULLER; JENTSCH; STODDART, 2009). Theoretical results showed a maximum efficiency around 0.42.

Figure 2.6 – Sistan VAWT.

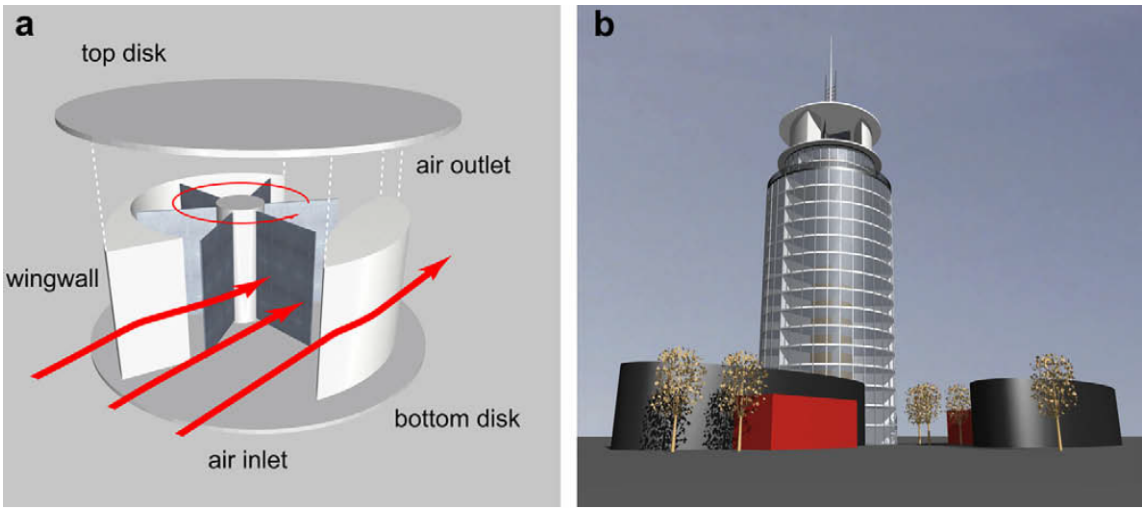

Source: (MULLER; JENTSCH; STODDART, 2009).

Combined technologies can also be verified as presented in Figure 2.7. In the presented figure, there was a three bucket Savonius rotor in the upper part of the rotor model and, in the lower part, there was a three bladed Darrieus rotor. One of the first tests combining these designs was made by (GUPTA; DAS; SHARMA, 2006) with maximum power coefficient of 0.18. (DEBNATH; BISWAS; GUPTA, 2009), the results achieve maximum power coefficient of 0.377. A complete review of such turbine was presented by (RATHOD et al., 2016).

About Darrieus based wind turbines, there are many designs depending on blade (curve or straight), how the pitch angle is controlled (fixed or variable pitch), and the format of rotor. All these variations present a range of efficiency from 0.3 to 0.7 (optimized wind turbines). The straight-bladed wind turbine or H-rotor has its curved blades replaced with straight vertical blades attached to the central tower. This model is much simpler to build, but results in more massive structure than the traditional Darrieus design, and it requires stronger blades (AMBROSIO; MEDAGLIA, 2010). These turbines have good performance in turbulent wind condition. An example is a VAWT-850 with 200 kW installed in Sweden in 1989 (see Figure 2.8).

The H-type VAWT had been studied by Peter Musgrove in the United Kingdom during the 70's, as well as a variation called Musgrove rotor or Variable geometry VAWT (TJIU et al., 2015). The rotor was a modification of the H-type VAWT by employing blades reefing mechanism to prevent the rotor from over-speeding in strong winds. Each

Figure 2.7 – Combined VAWT.

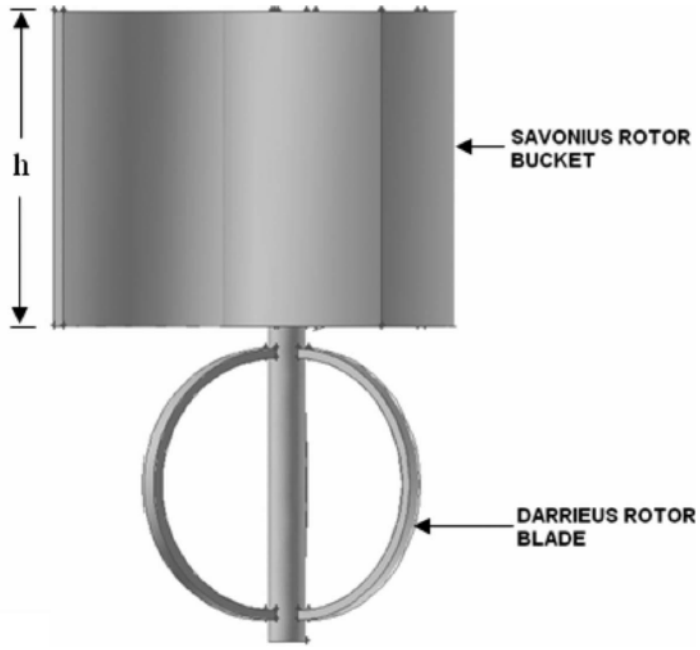

Source: (DEBNATH; BISWAS; GUPTA, 2009).

Figure 2.8 – H-type VAWT.

Source: (AMBROSIO; MEDAGLIA, 2010).

set of the blades consisted of two equal portions feather-able about horizontal beam, for which, in reefed position, they took the shape of a double arrow, thus, reducing the sweep area as well as the lift force of the blades, tangential to the radial line of the rotor (VAAHEDI; BARNES, 1982). An example is presented in Figure 2.9.

Figure 2.9 – Musgrove VAWT.

Source: (PRICE, 2006).

The Giromill (see Figure 2.10) is a VAWT that has straight blades whose angle of attack is controlled so as to maximize wind energy conversion. Each airfoil is rocked during a revolution in order to maintain a constant positive angle of attack over one half revolution and a constant negative value over the other half revolution (MCCONNELL, 1979). Variable pitch blades have the potential to overcome the starting torque issue associated with VAWT. Although having a simple construction, fixed pitch blades have poor starting torque. Variable pitch designs have many advantages over fixed pitch, but the construction of support structures for changing the pitching angle is very complicated, hence reducing the cost-effectiveness of the turbine to either small or large scale applications (BHUTTA et al., 2012).

Two-tier VAWT: A two-tier configuration for straight bladed rotor was suggested by Gorelov and Krivospitsky (GORELOV; KRIVOSPITSKY, 2008). It is called Masgrowe rotor. The turbine assembly is divided into two tiers with two or three blades in each tier. The two-tiers are shifted by 90°. The two-tier configuration facilitates the operation by enabling the turbine to self-start at wind velocity as low as 1.6 to 2 m/s with efficiency of 39 to 40% and thus eliminating the use of variable pitch rotor. Other features are: the unnecessarily complex design of reefing mechanism; large concrete structure is needed; high cost in building the turbine; it is consisted of many components which hindered its cost-effectiveness (BHUTTA et al., 2012). An example is showed in Figure 2.11.

Figure 2.10 – Giromill VAWT.

Source: (AHMADI, 2012).

Figure 2.11 – Two tier VAWT.

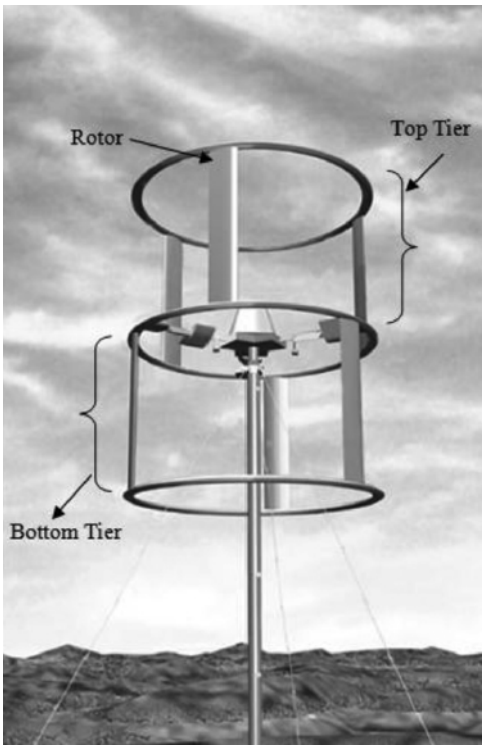

Source: (BHUTTA et al., 2012).

Articulating VAWT (see Figure 2.12) is another variation of Darrieus turbine. This turbine is a combination of helicopter rotor head and wind turbine design. The rotor works

when wind causes rotor tilt, setting the airfoil angle of attack, resulting in aerodynamic lift; this lift creates torque and consequently, rotation. Other feature is self-correction for gyroscopic precession (BOATNER, 2010). The turbine has the following issues: very high torque due to long moment arms, large working areas for more power, dynamic response to wind and load conditions, self-limiting to prevent run-away, no external wind alignment mechanics, self-starting at low wind speeds and very quiet compared to most turbines.

The work principle of the wind turbine is based on gimbal or swashplate-like mechanism, in which the blades are free to oscillate or tilt around hub. Elastomeric dampeners are used to prevent the blades from over-tilting. Pitch control via articulating motion allows the turbine to self-start at light wind, despite having low solidity, higher torque during operation, as well as for aerodynamic brake. Another advantage of articulating motion is that the blades swiftly adapt to the wind force, thus reducing vibration, as often occurs in stiff and fixed blades. The feature is highly advantageous for urban application, where the wind is more turbulent (TJIU et al., 2015).

Figure 2.12 – Articulating VAWT.

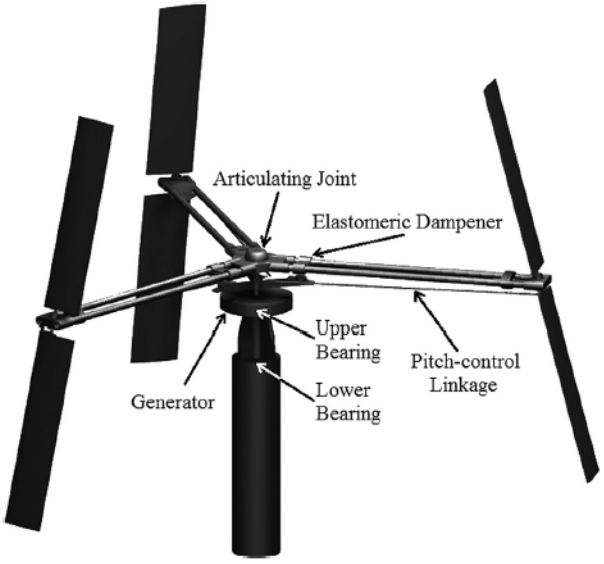

Source: (BOATNER, 2010).

The V-rotor was proposed by Olle Ljungstrom in 1973, projected to mimic the lower half of a phi-rotor. It has the advantage of a shorter tower than a phi or H-rotor and it avoids the horizontal (and therefore dragging) struts and supporting arms of phi and H-rotors. In a recent review of VAWT technologies and economics, Sandia Laboratories concluded that VAWT have significant advantages over HAWT in offshore applications (ASHWILL; SUTHERLAND; BERG, 2012) and that H or V-rotor designs are likely to be more cost-effective (SHIRES, 2013). The variable geometry oval trajectory (VGOT) turbine can be defined as offshore variation of V-rotor (see Figure 2.13). In that design, the blades instead of revolving around a central rotor, move on rails on an elevated rail

track. The wheels attached to the base of the blades are coupled with electrical systems to generate electricity. This design promises the possibility of large scale power generation. It combines the omnidirectional nature of VAWT with high efficiency (as high as 57% at optimum design configurations) and increased structural stability and eliminates the issues of low starting torque. Despite all the predicted benefits, the design has yet to prove its capabilities through a manufactured prototype (BHUTTA et al., 2012).

Figure 2.13 – VGOT VAWT.

Source: (SHIRES, 2013).

The last design to be study is the Gorlov Helical turbine (see Figure 2.14). Originally it was invented for hydraulic purposes by Alexander Gorlov in 1995 (GORLOV, 1995).

Figure 2.14 – Gorlov helical turbine.

Source: (TJIU et al., 2015).

The turbine consists of three vertical airfoil blades, each having a helical twist of 120 degrees. This feature spreads the torque evenly over the entire revolution, thus preventing the destructive pulsations of the straight-bladed Giromill. The wind pushes each blade around on both the windward and leeward sides of the turbine. This rotor has a positive lift at zero angle of incidence enabling it to self-start at favourable wind conditions (where ordinary Darrieus rotor may require auxiliary mechanism for starting). Currently, helix design is getting popularity not only because of better performance, but also for the esthetic value, in which modern elegant design harmonizes the elements in the space; the main drawback of this configuration is the complexity involved in the manufacture of twisted blades, that increase the size of the turbine.

2.3.1 Wind turbines installed on buildings

Not so recently, building rooftops have appeared as a good location for small wind turbines, because of the proximity to the consumer, also taking advantage of faster wind while reducing the cost of support towers. Early studies were presented by (MERTENS, 2003). The study shows the necessary guidelines for sitting small wind turbines on the roof. Guidelines such as height above the roof, behave of wind above the roof and its probability distribution are considered. The study realized that when comparing horizontal and vertical axis turbine, VAWT seems to be more suitable for rooftop than HAWT, because of their larger power output and energy yield in skewed flow. Nevertheless, the wind velocities above the roof are still small in relation to open surrounds. So, for roof turbines, high buildings are necessary to compensate the small wind speed in the built environment and produce an acceptable energy yield.

According to (CASINI, 2016), there are three ways to integrate wind turbines to buildings. The first, the turbines can be located close to the building, on the rooftop (see Figure 2.15) or along the sides: It is possible to exploit the acceleration of the air flow upper corners and the sides of the building. However, this phenomenon is followed by the formation of turbulent areas because of the air flow separation, making VAWT more effective than turbines with HAWT.

The second form is to install the wind turbine between the buildings (see Figure 2.16), but it requires special integration between the formal architectural design and the system solution. By locating buildings with a specific geometric shape at a precise distance, it is possible to make the facade surfaces, exposed to the wind, contribute to channel the prevailing winds. The two buildings can be positioned according to the direction of the wind so they can act as a funnel or as a diffuser, the latter being capable of creating a higher pressure gradient, able to channel the input flow and accelerate it in correspondence with the turbines. This solution is particularly suitable for horizontal

axis turbines that can take advantage of a large section undisturbed air flow, obtaining good yields in the production of electrical energy due to the possibility of installing large rotors.

Finally, the third way of integrating wind turbine into buildings is to insert it inside air conducts (see Figure 2.17), taking advantage of the difference in air pressure generated by the wind, that affects the opposing facades. A building hit by wind builds up the air in motion on the windward side resulting in an area of relatively high pressure. On the leeward side instead, a shadow of the wind with a relatively low pressure is created. The presence of two opposite openings on the windward and on the leeward determines an air current which can be used to power a wind generator. The generated air flow is proportional to the difference in wind pressure existing in correspondence with the entrance and exit apertures, their overall size and the dimensional ratio between the

Figure 2.15 – Rooftop installed VAWT.

Source: Author.

Figure 2.16 – Wind turbine between buildings.

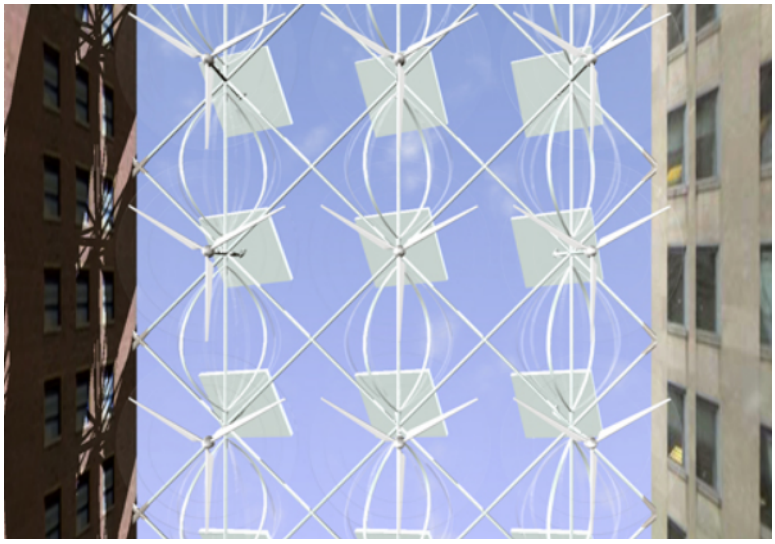

Source: https://landartgenerator.org/blagi/archives/406.

openings.

Figure 2.17 – Wind turbine inside air conducts.

Source: (CASINI, 2016).

2.4 IMPROVEMENT SOLUTIONS

Many studies have been presented in order to improve the overall performance of vertical axis wind turbines. These studies are associated with testing changes in parameters such as solidity, aspect ratio, chord length, number of blades, Reynolds number, wind velocity, tip speed ratio, starting torque; evaluating different airfoil profiles; adding

mechanism into the blades to control airflow through themselves (pitch control); or use wind turbine generator to start it at very low winds.

2.4.1 Design parameters

There are many aspects that could be modified in order to evaluate the performance of VAWT, such as the comparison of theoretical and practical, about the how choice of airfoil can influence the turbine. (JI; SCHLUTER, 2011) studied three different airfoils: NACA 0022, asymmetric S1223 and symmetric SD8020. It was concluded that unsteady flow field had significant influence on upstream blade performance. This is why low power extraction is observed on downstream region. Another author who evaluated the airfoil effect is (SINGH; BISWAS; MISRA, 2015). It was tested H-Darrieus rotor with three S1210 airfoils to study the self-start capability. The studied turbine exhibited high positive static torque coefficient at all rotor angles for all solidity conditions. Positive static torque means the rotor does not have any negative torque band during start up, which is enabled to self-start.

About influence in mechanical features, (HAMEED; AFAQ, 2013) evaluated solidity, aspect ratio, pressure coefficient, deflection and bending stress of VAWT. As a result, bending stress and deflections are not only a function of aerodynamic forces, but also very dominantly controlled by centrifugal forces. Wall thickness of the blade can be optimized by reducing weight of the blade, but maximum stresses and maximum deflection should be in acceptable range.

Authors such as (SUNNY; KUMAR, 2016; LI et al., 2016; RISHMANY et al., 2017) used wind tunnel and multi-body dynamic analysis tool to investigate VAWT performance. During the tests, they realized that wind turbine performance appeared to be slightly dependent on the blade pitch angle and number of Reynolds. Increasing the number of Reynolds, the performance rises, as well. Unfortunately, increasing the tip speed ratio, the wake velocity is reduced. (ABU-EL-YAZIED et al., 2015) evaluated how number of blades and chord length can influence Darrieus turbine performance using CFD analysis. Tests were done for two, three, four and six-bladed, with NACA0021 blade profile. As a result, the peak of power coefficient dropped with the increase of rotor solidity, while it moved to lower tip speed ratio; a larger number of blades allowed to reach the maximum power coefficient for lower angular velocities, but it was penalized as much as efficiency is important; rising chord length and decreasing in number of blades maximize power coefficient. However, after certain increasing in blade, chord length minimized power coefficient; it was found that torque ripple factor for wind turbine was decreased with increasing number of blades and increasing blade chord length. (BATTISTI et al., 2016) compared different small vertical axis wind turbine architectures focusing on the

analysis of VAWT loads, depending on the blade number, airfoil camber and blade inclination. It was noted that three bladed wind turbines exhibit a better performance when compared to two bladed ones. As a consequence, a higher thrust is also registered. A lower variation of both torque and thrust also emerges when compared to a two-bladed rotor. Such behavior could represent a great advantage for three-bladed small VAWT architectures, for which the increased manufacturer and installation costs are not so important as for large rotor. Moreover, the cambered airfoil suggests an increased rotor performance at starting TSR (at low rotor speed, mitigating VAWT start-up problems), but also a marked limitation in exploiting the wind resource at medium to low speeds. Because the fatigue life of VAWT is often considered as important as power production of great interest, it also appears the helical shaped rotor, which further reduces the cyclic oscillation of the aerodynamic loads, thus extending the turbine long-term life and reducing its vibrations for power controller purposes, is the most efficient architecture for the wind energy exploitation. However, the operation of the helical turbine at starting TSR appears less efficient, the blade manufacturing costs are actually higher than the straight blade type and more experimental tests have still to be encouraged, in order to clarify the actual potential and limits of Gorlov wind turbines.

2.4.2 Pitch angle

Regarding blade pitch mechanism to alter blade pitch angle, plenty of methods and structures were proposed. According to (LAZAUSKAS, 1992), pitch systems can be all configured to produce better starting torque, a broader operating range and greater efficiency than fixed pitch vertical axis wind turbine. These characteristics are confirmed by (MIAU et al., 2012; DOUAK; AOUACHRIA, 2015) that have noted an improvement of starting torque and aerodynamic characteristics in relation to fixed blade scheme, mainly at low tip speed ratios. Also, it was observed that the larger the pitch angle is, the easier the wind turbine gets to start to rotate.

As mentioned earlier, there are some methods to control the pitch. These forms are passive or active pitch control. Besides controlling blades collectively or individually, (REYALA, 2012; AGGRAWAL, 2016) applied active individual pitch control to obtain maximum coefficient of power harnessed from the turbine. An improvement of 12.5% was achieved on performance. (THOMSEN; NIEMANN; POULSEN, 2008) described a model and control for an individual pitch method in order to attenuate the effect of asymmetric wind loads. Simulations with a full stochastic wind field illustrate the effectiveness of the individual pitch controller as compared to controlling the pitch collectively.(LIANG et al., 2016) compared collective and individual pitch control for straight-bladed vertical axis wind turbine to improve self-starting capacity. The results indicate that blade pitch

method can increase the power output and decrease the deformation of blade. The total torque coefficient of blade pitch control at tip speed ratio 1.5 is about 2.5 times larger than that of fixed pitch case. (CHOUGULE; NIELSEN, 2014) included into the vertical axis wind turbine a blade pitching mechanism to a 500 W vertical axis wind turbine, trying to solve self-start inability and to improve its power coefficient. A pitch control linkage mechanism for vertical axis wind turbines is modelled from a mathematical model based on double multiple streamtube method. The author noticed that the model with 5° of blade pitch angle amplitude has increased in power coefficient by 12%. (BOUZAHER; HADID, 2015) proposed a dynamic control device which consists in the association to each blade, a couple of flapping wings in order to deal with dynamic stall and the generated vortices by the blades. The proposed scheme ensures an important attenuation in the magnitude of the generated vortices and a rapid mitigation of the generated wakes, then avoiding the interference with the distributed flow caused by previous blades. (KORPRASERTSAK; LEEPHAKPREEDA, 2016) presented the analysis and optimal design of airflow controlling equipment, called booster, for a VAWT. This mechanism threat not only harvest energy with low availability at low wind speed, but also enhance performance of the VAWT at high wind speed. As the result, it was noticed that booster is capable of producing mechanical power that is even higher than the original one. This mechanism helps to overcome the limitations of very low power at weak speed wind. (JAIN; ABHISHEK, 2016) analyzed the aerodynamic performance of a vertical axis wind turbine with pitch control. A method for calculating virtual camber effect for dynamically pitching blades is proposed and validated. The parametric study relates performance of vertical axis wind turbine to rotor solidity, blade airfoil and pitch amplitude. The amplitude of sinusoidal blade pitch must be varied with wind speed and tip speed ratio to maximize the power extraction from turbine. High pitch amplitude, 35°, works best for tip speed ratios below 0.5, at the same time, pitch amplitude should be reduced to 10° for tip speed ratios greater than 2. When aspect ratio is increased, subject to the condition that the blade swept area remains constant, the predicted power increases; a variable pitch VAWT is quite sensitive to the fluctuations in the wind direction. However, it can tolerate wind approaching from the advancing side by up to 15% while maintaining the same level of performance. Beyond this 0-15% range, performance degrades, which requires the phase of pitch amplitude to be aligned with the wind direction by an active/passive control system. By adjusting the direction of the offset link by up to 60% in the direction opposite to the direction of rotation, negative torque can be generated for all tip speed ratio, which can be used for storm protection.

2.4.3 Generator as motor

The use of wind turbine generator as a motor in order to overcome high inertia momentum and extract more energy from wind at very low winds or in shut down schemes. (SVENDSEN; MERZ, 2013) presented the control of Deepwind floating VAWT with emphasis on start-up and shut-down schemes preventing mechanical damages. The results found the behavior of the turbine during start and stop to be fairly smooth. The torque is the only variable control; it is inevitable that peaks in the torque above the nominal value occur for the dimensioning the generator. Other author that utilized this was (MARQUES, 2014), who developed an automatic operation and control system for an experimental vertical axis wind turbine in which uses turbine generator to apply a starting torque, enough to overcome its inertia to harnessing energy at low winds. The system was implemented using a state-machine to manage the operation of the turbine system and a variable speed control method was implemented in order to maximize power extraction. Another example of starting a turbine using its generator is showed in (HOGBERG, 2009) for a 12 kW straight bladed vertical-axis wind turbine. The generator was designed exactly to wind energy, with large overload capabilities and reasonable efficiency at low rotational frequencies. The only way to regulate the power is controlling the rotational speed. The generated electric power is used by radiators warming the control room. The starting strategy is done with a battery bank and DC-AC converter. The last example was presented by (KJELLIN, 2012). The author worked with a 12 kW VAWT that is not self-starting. So that, an electrical starter system has been designed for turbine. The starter system uses the auxiliary winding of the generator as a motor.

2.5 CONCLUSION

This chapter established the basis about the development, designs and aspects in order to extract better performance of VAWTs. It could be noted that VAWT may be integrated on buildings with adequate project, taking advantage from environmental conditions. New designs showed many ways to use the wind in order to harness its energy. Also, it takes into account the proper project regarding number of blades, blade airfoil, solidity, and other parameters or addition of auxiliary mechanism, it is possible to significantly improve VAWT coefficient of power and mitigate structural stresses turn VAWT suitable to be competitive not just to HAWT, but also to other renewable sources. The next chapter, aerodynamic modelling is introduced to understand how velocities and forces act on VAWT.

3 AERODYNAMICS

3.1 INTRODUCTION

To estimate the aerodynamic performance and loads that act on vertical axis wind turbine, many methods can be found (ISLAM; TING; FARTAJ, 2008; JIN et al., 2015). This chapter will present a review of these methods and also apply double multiple streamtube model (DMSTM) to predict the torque behavior and power coefficient. It is possible to divide these algorithms into two categories such as computational fluid dynamics and experimental dynamics (see Figure 3.1).

Figure 3.1 – Aerodynamic models.

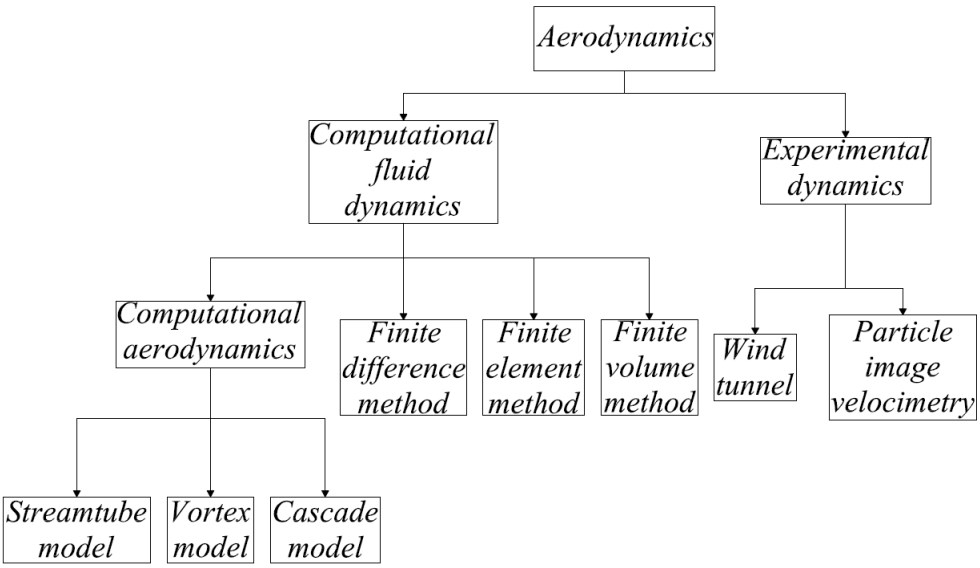

Source: Author.

3.2 AERODYNAMIC MODELS

3.2.1 Streamtube model

The streamtube models are based on the combination of momentum theory and blade element theory, that allow to evaluate flow velocities through the turbine equating the streamwise aerodynamic force on the blades with the change of air momentum (JIN et al., 2015; TCHAKOUA et al., 2015). According to (VANDENBERGHE; DICK, 1987), streamtube models can predict reasonably well the overall performance of wind

turbines, but fail to predict the streamwise variation of the induced velocity and the local aerodynamic forces on the blades. These shortcomings may be overcome using DMSTM. (TCHAKOUA et al., 2015) said that these models, such as single and multiple streamtube models can predict the overall performance of a lightly loaded wind turbine with short computational time. Besides, they provide a good correlation between the prediction and the experimental data. Otherwise, these methods are invalid for large tip speed ratios and for high rotor solidities and cannot give any information about the shape of the near wake, which is important when considering the placement of struts and other structures close to the turbine blade, and it shows some convergence problems (VALLVERDU, 2014; TCHAKOUA et al., 2015; HANSEN, 2015).

3.2.2 Vortex model

This model is based on free-wake vortex model and fixed-wake momentum theory (TCHAKOUA et al., 2015). First, the turbine is divided into various nodes. In each node is applied the assumption that the induced velocity field results from combined effects of bound and wake vorticity distribution. The bound vorticity distribution is related the distribution of circulation on the blade due to the vorticity contained in the boundary layers of the wing. The wake vorticity comes from the distribution of circulation in the wake of the blade section. The shed wake ultimately stems from the bound vorticity distribution which flows blade tips (OKPUE, 2011). According to (VANDENBERGHE; DICK, 1987; TCHAKOUA et al., 2015), vortex model might predict very well the instantaneous blade forces and the wake structure, it is able to include the dynamic stall effect, pitching circulation and added mass effect; it is also capable of providing information about the wake structure near the turbine, because the normal velocity to the airflow is neglected; high-precision prediction capabilities; can be used for highly loaded rotors at large tip speed ratios; naturally addresses perturbations both parallel and perpendicular to the streamwise velocity. However, relies on significant simplifications; convergence problems in some cases; computational accuracy greatly dependent on the potential flow model used in computations (TCHAKOUA et al., 2015; JIN et al., 2015).

3.2.3 Cascade model

This theory is widely used in the turbomachinery for calculating the dynamic forces induced by the flow over blades in turbines and compressors. The cascade refers to an array of blades around the hub of the rotor. The model assumes the airfoil to be unwrapped into an array of blades, having uniform pitch and spacing between them (OKPUE,

2011). (TCHAKOUA et al., 2015) highlighted that, it can predict the overall values of both low and high solidity turbines quite well; highly precise computation with no iterative convergence even at high tip speed ratios and high solidities; incorporates the effect of the Reynolds number variation at different azimuth angles, zero-lift-drag coefficients, finite aspect ratios and flow curvature effect in the calculation process; dynamic stall and flow curvature with blade pitching can be considered; achieves smooth convergence even at high tip speed ratios and high solidity VAWT with quite reasonable accuracy. However, for all these features, reasonable computation time is needed.

3.2.4 Fluid dynamic models

The fluid dynamic based method is used to evaluate the fluid fields, highlighting the presence of a complex vortices pattern. Solving the Unsteady Reynolds Averaged Navier Stokes equation (TCHAKOUA et al., 2015).

According to (JI; SCHLUTER, 2011), fluid dynamic methods can be separate into finite difference method, finite element method and finite volume method. These models differ from each other in governing equation. Among them, the most used is the last one (S.; UK, 2013).

Fluid dynamic methods provide a more precise aerodynamic prediction for VAWT; it can thoroughly visualize the flow near airfoils; it can accelerate the design process and reduce the overall cost of design; there are effective solutions for the analysis of local flow fields around blades, particularly for dynamic stall and wake flow; it is also an attractive solution for performance optimization. Otherwise, it is computationally too expensive and prohibitive for the routine engineering analyses of the local interaction mechanism of wind turbines (TCHAKOUA et al., 2015).

3.2.5 Experimental dynamics

Regarding practical tests, the use of wind tunnels or particle image velocimetry is applied. Wind tunnels mainly focus on studying the operating features and mechanical aspects (ARMSTRONG; FIEDLER; TULLIS, 2012; MCLAREN; TULLIS; ZIADA, 2012; DANAO; EBOIBI; HOWELL, 2013; WORASINCHAI; INGRAM; DOMINY, 2013) and provide a final evaluation, so to improve the efficiency (JIN et al., 2015). Meanwhile, the second one evaluates the flow distribution (FUJISAWA; SHIBUYA, 2001; FERREIRA et al., 2008; TESCIONE et al., 2014). Some applications of particle image velocimetry are observation of stall, the behavior of a flow evolving around the airfoil and the wake flow.

3.2.6 Equivalent electrical model

Proposed by (TCHAKOUA et al., 2015), this model is based on the association between mechanical and electrical circuits being suitable for the design, performance prediction and optimization of Darrieus rotors. The model can be used to simulate the rotor behavior for the case of a mechanical fault on one or more of the blades as well as on rotor-shaft coupling elements. Its major benefit is that computational studies are more economical than such costly experiments. There are various wind turbine computational models, each with their own strengths and weaknesses, which attempt to accurately predict the performance of VAWT. Furthermore, none of the described models with high reliability and accuracy can be efficiently coupled with models of the mechanical and electrical parts of the wind turbine to form a global model for the wind energy conversion system.

3.3 EQUATIONS FOR MOMENTUM THEORY AND STREAMTUBE MODELS

3.3.1 Blade element momentum method

Take into account the Figure 3.2 as a 1-D rotor with a permeable disc. The disc is considered ideal, frictionless and with no rotational velocity in the wake region. Due to the assumption of an ideal rotor, it is possible to derive simple relations among velocities, power and thrust force. These associations are exposed below.

Figure 3.2 – Control volume definition for the BEM method.

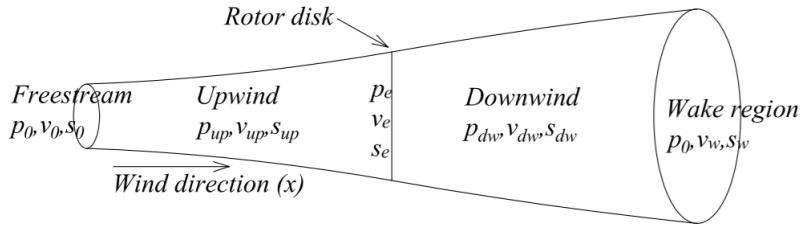

Source: Adapted from (HANSEN, 2015).

Take into account the following assumptions: the fluid is incompressible and it is in steady state, there is an infinite number of blades and the wind speed is constant inside the tube, so $v_0 = v_{up} = v_e = v_{dw} = v_w$. Where v_0, v_{up}, v_e, v_{dw} and v_w are respectively freestream velocity, upwind velocity, rotor velocity, downwind velocity and wake velocity.

The mass flux deviation is defined by:

$$\frac{dm}{dt} = \dot{m} = \rho v_e s_e, \tag{3.1}$$

with ρ and s_e being air density and rotor area.

The force acting on the rotor, because of pressure difference or thrust, is calculated as:

$$F_t = \dot{m}(v_0 - v_w). \tag{3.2}$$

Considering that there is not work done in this system, it is possible to apply Bernoulli's equation before and after rotor, resulting in:

$$p_0 + \frac{\rho v_0^2}{2} = p_{up} + \frac{\rho v_{up}^2}{2}, \tag{3.3}$$

$$p_{dw} + \frac{\rho v_{dw}^2}{2} = p_w + \frac{\rho v_w^2}{2}, \tag{3.4}$$

where p_0, p_{up}, p_{dw} and p_w are freestream pressure, upwind pressure, downwind pressure and wake pressure respectively.

Other expression to obtain the thrust is using:

$$F_t = s_e \Delta p_e, \tag{3.5}$$

where $\Delta p_e = p_0 - p_w$ whereas upstream and downstream were considered the same point $(p_{up}, v_{up}) = (p_{dw}, v_{dw}) = (p_e, v_e)$.Considering p_e as the pressure at the rotor.

So, when isolating p_0 and p_w in equations (3.3) and (3.4), and putting them in equation (3.5), the result is:

$$F_t = \frac{\rho s_e (v_0^2 - v_w^2)}{2}. \tag{3.6}$$

Now, comparing equations (3.2) and (3.5), it is possible to define velocity on rotor region as:

$$v_e = \frac{v_0 + v_w}{2}. \tag{3.7}$$

So that, it is possible to define an induction factor a, that describes the relation between freestream and upstream velocities as:

$$\frac{v_0 - v_e}{v_0} = 1 - \frac{v_e}{v_0} = 1 - a, \tag{3.8}$$

then it concludes,

$$v_e = v_0(1 - a). \tag{3.9}$$

In the same way to right side

$$v_w = v_0(1 - 2a). \tag{3.10}$$

The power extracted from the wind by wind turbine is defined by:

$$P = F_t v_e = \frac{\rho s_e v_e (v_0^2 - v_w^2)}{2}. \tag{3.11}$$

Putting the equations (3.9) and (3.10) in equation (3.11), the result is:

$$P = \frac{\rho s_e (v_0^2 - (v_0(1-2a))^2) v_0 (1-a)}{2} \tag{3.12}$$

$$= \frac{\rho s_e v_0^3 4a(1-a)^2}{2}. \tag{3.13}$$

The term $(\frac{\rho s_e v_0^3}{2})$ is known as the total power available in the wind P_0. So, rewriting equation(3.13), it is obtained:

$$\frac{P}{P_0} = 4a(1-a)^2 = C_p, \tag{3.14}$$

where it is obtained the efficiency of wind turbine or the power coefficient C_p. Its limit is calculated deriving equation (3.14) in relation a, resulting in a $C_p = 0.5926$ ($a = \frac{1}{3}$). It means, the maximum C_p to any type of wind turbine is 59.26%.

In the same way, applying this reasoning to thrust force, it is possible to calculate the thrust coefficient by:

$$C_t = \frac{F_t}{F_{t_0}} = \frac{2\rho s_e v_0^2 a(1-a)}{\frac{1}{2}\rho s_e v_0^2} = 4a(1-a), \tag{3.15}$$

with its maximum equals to $C_t = 1$ ($a = 0.5$), however when $a = 0.5$, $C_t = 0.889$.

These results said that if an ideal rotor was built, so that the velocity of wind at rotor region would be $\frac{2}{3}$ of freestream velocity. Considering the wind turbine operating at its maximum power point tracking, that C_p is know by Betz's Limit.

For (HANSEN, 2015), it can be seen that assumption of an ideal wind turbine is only valid for an induction factor, a, less than 0.4 in equation (3.15). This situation is known by turbulent-wake state. The cited situation is shown in Figure 3.3.

According to (WOOD, 2011) many efforts have been made to correct it. One of them is: replacing C_t equation with:

$$C_t = 4a(a-1) + 2, \tag{3.16}$$

Figure 3.3 – Blade element momentum valid region.

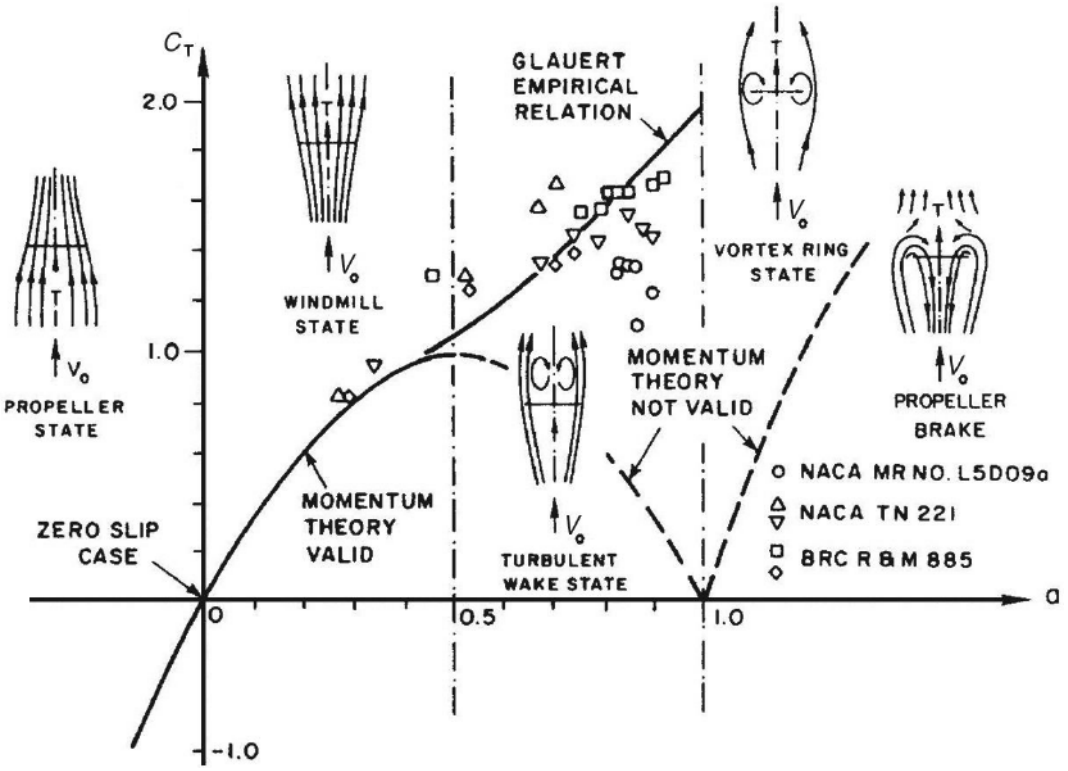

Source: (HANSEN, 2015).

with $a > 0.5$. And the other option for elevated thrust is given by:

$$C_t = \begin{Bmatrix} 4a(1-a) & a \leq a_c \\ 4a_c^2 + (1-2a_c)a & a > a_c \end{Bmatrix}, \tag{3.17}$$

where $a_c = 0.3333$ is an auxiliary constant.

Therefore, this established limit can be exceeded if the turbines use the Shrouded rotor, which means putting wind turbine in a type of diffuser. For detail considerations see (JAMIESON, 2011; HANSEN, 2015).

3.3.2 Streamtube based models

From the presented theory, three methods to predict the performance were developed: single streamtube model (SSTM), multiple streamtube model (MSTM) and double multiple streamtube model (DMSTM) as presented in Figures 3.5 and 3.4.

Figure 3.4 – Actuator disk development.

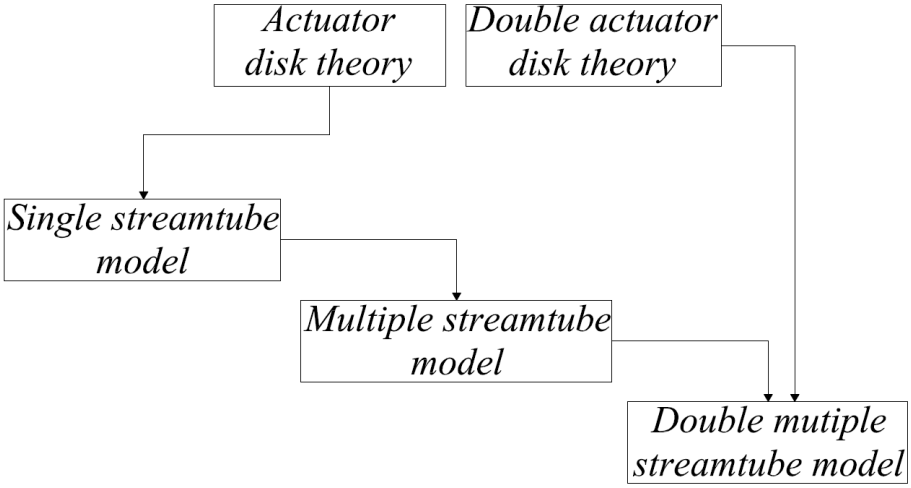

Source: Adapted from (BIADGO et al., 2013).

Figure 3.5 – Diagram of each model.

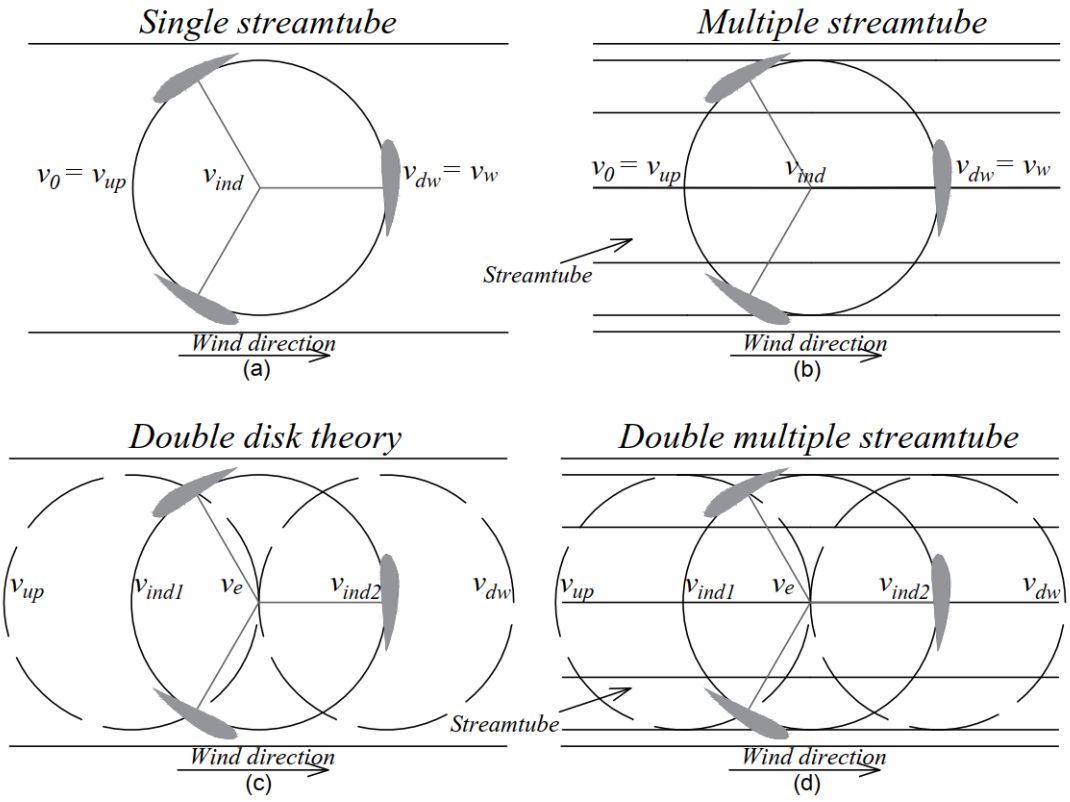

Source: Author.

3.3.2.1 Single streamtube model

Developed by (TEMPLIN, 1974), this model is the simplest method to estimate VAWT performance. It considers the rotor being inside a unique streamtube and applying

the actuator disk principle and blade element for estimating the overall wind turbine performance, as shown in Figure 3.5(a). This model always predicts higher power than the experimental results. However, it cannot be used to predict the wind velocity distribution across the rotor (ISLAM; TING; FARTAJ, 2008). The SSTM considers that there is no loss of velocity from freestream to rotor, or from wake region. So, the induction factor a is considered the same for any position on rotor. In order to calculate the output power of the wind turbine using SSTM, take a look in Figure 3.6.

Figure 3.6 – Velocities and forces in a streamtube.

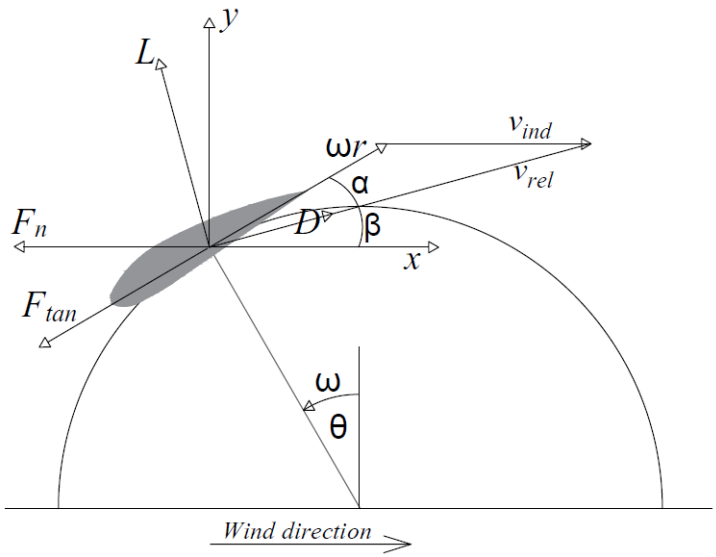

Source: Author.

It is possible to defined the velocity in x-axis and y-axis as:

$$v_x = (\omega r)\, sin(\theta), \tag{3.18}$$

$$v_y = (\omega r)\, cos(\theta) + v_{ind}, \tag{3.19}$$

where r, ωr, θ and v_{ind} are respectively the radius of wind turbine rotor, blade rotational velocity, azimuthal angle and induced velocity on the blade.

The wind speed seen by blade point of view is called relative velocity and it is defined by:

$$v_{rel} = \sqrt{v_x^2 + v_y^2}. \tag{3.20}$$

Substituting equations (3.18) and (3.19) in equation (3.20) result in:

$$v_{rel} = \sqrt{(\omega r)^2 + v_{ind}^2 + 2\,(\omega r)\, v_{ind} \cos(\theta)}. \tag{3.21}$$

The equation (3.21) can be rewritten relating to tip speed ratio λ and induction

factor a by:

$$v_{rel} = v_0\sqrt{\lambda^2 + 2a\lambda\cos(\theta) + a^2}, \tag{3.22}$$

with tip speed ratio calculated as:

$$\lambda = \frac{\omega r}{v_0}. \tag{3.23}$$

The flight path angle is the angle between x-axis and relative velocity and is defined as:

$$\beta = arctan\left(\frac{v_x}{v_y}\right) \tag{3.24}$$

or

$$\beta = arctan\left(\frac{\lambda\sin(\theta)}{\lambda\cos(\theta) + a}\right). \tag{3.25}$$

Computing the flight path and azimuthal angle, makes possible to calculate the angle of attack as being the angle between relative velocity and blade rotational velocity like:

$$\alpha = \left|\frac{\beta - \theta + \pi}{2\pi}\right| - \pi + \Omega, \tag{3.26}$$

with Ω being pitch angle.

After to define velocities, it is possible to calculate the loads that act on the blades. There are two main forces: the first one is the normal, or radial force, also called thrust and the tangential force. They are defined as:

$$F_n = Dcos(\beta) - Lsin(\beta), \tag{3.27}$$

$$F_{tan} = (Dcos(\beta) - Lsin(\beta))(-\cos(\theta)) + (Dsin(\beta) - Lcos(\beta))(-\sin(\theta)), \tag{3.28}$$

where L and D are lift and drag forces described by:

$$L = \frac{1}{2}\rho chv_{rel}^2 c_l, \tag{3.29}$$

$$D = \frac{1}{2}\rho chv_{rel}^2 c_d, \tag{3.30}$$

with c_l and c_d are the lift and drag coefficients. These coefficients depend on what airfoil is utilized. c is the chord length and h is the blade length.

Between normal and tangential forces, the only one that contributes to generate

torque on blades, putting them in movement, is the tangential force. The produced torque is obtain by:

$$F_{torque} = F_{tan} r, \tag{3.31}$$

thus the power generated by all blades is:

$$P_{wt} = \left(\sum_{j=1}^{N_{blades}} F_{torque} \right) \omega, \tag{3.32}$$

N_{blades} is number of blade at wind turbine rotor.

The power coefficient can be calculated by:

$$C_p = \frac{P_{wt}}{\frac{1}{2}\rho s_{rotor} v_{up}^2}, \tag{3.33}$$

where s_{rotor} for straight bladed VAWT is $2rh$.

3.3.2.2 Multiple streamtube model

This method was presented by (WILSON; LISSAMAN; WALKER, 1976; STRICKLAND, 1976). The rotor swept volume is divided into a series of adjacent and aerodynamically independent parallel streamtubes (JIN et al., 2015) and are represented by straight lines in Figure 3.5(b).

To evaluate turbine efficiency, blade element theory is applied in each streamtube. The algorithm is fast, it is more precise in calculating the C_p and distributed effects such as blade forces and rotor wake velocity distributions (STRICKLAND, 1976), however, estimated power is lower than experimental results and also it is not able to differentiate upwind part from downwind part of the rotor as well as single streamtube. The development of equations for this model is based in Figure 3.7.

Now, the total span of tube is separated in i small streamtubes, and then the equations presented earlier are applied to each streamtube. When calculus are done, it obtains the average thrust, torque and power of wind turbine.

After defining the number of streamtubes N_{st}, is calculated $\Delta\theta$ like:

$$\Delta\theta = \frac{\pi}{N_{st}}. \tag{3.34}$$

The number of $\theta_i's$ is given by $N_{\theta_i} = 2N_{st}$. Other modification is relating to area used in equations, because now each streamtube area instead rotor are will be utilized, and it can be obtained with $s_{st,i} = rh\Delta\theta sin(\theta_i)$.

The instantaneous normal force on a single blade at one azimuthal location is given by (3.27). The average thrust considering N_{blades} and noting that each blade spend $\frac{\Delta\theta}{\pi}$

Figure 3.7 – Rotor divided into several minor streamtubes.

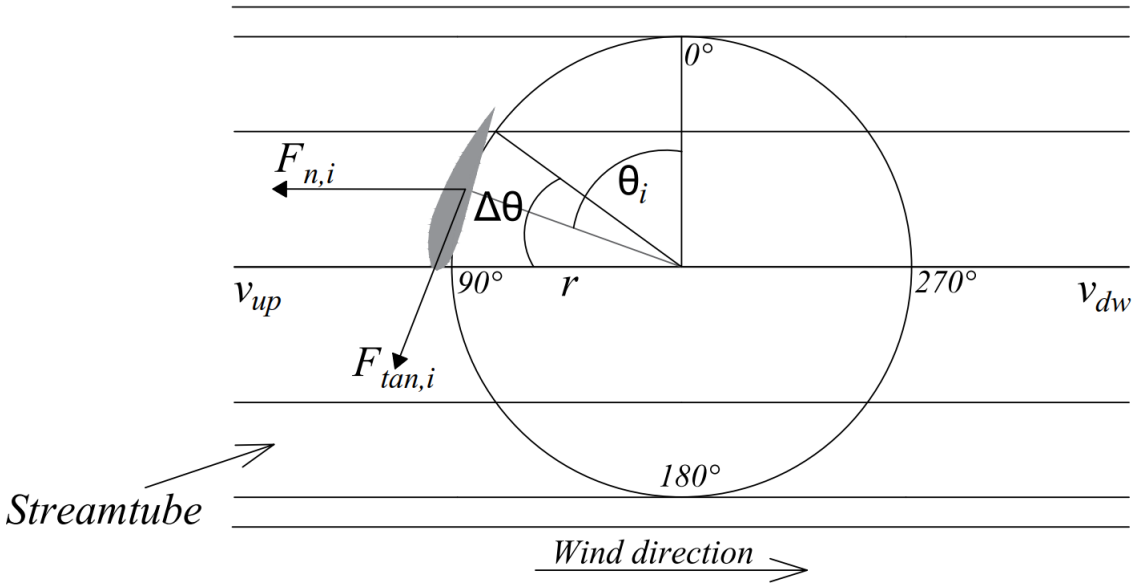

Source: Author.

percent of their time in each streamtube, thus:

$$F_{n,avg} = 2\left(N_{blades}\frac{\Delta\theta}{\pi}F_n\right). \tag{3.35}$$

The thrust coefficient can calculated as presented below:

$$C_t = \frac{F_{n,avg}}{\frac{1}{2}\rho s_{st} v_{up}^2}. \tag{3.36}$$

The average torque can obtain follow equation:

$$F_{torque,avg} = N_{blades}\sum_{i=1}^{N_{\theta_i}}\frac{F_{torque}}{N_{\theta_i}}, \tag{3.37}$$

and the torque coefficient and power coefficient are defined by:

$$C_{torque} = \frac{F_{torque,avg}}{\frac{1}{2}\rho v_{up}^2 (2rh)\, r}, \tag{3.38}$$

$$C_p = \lambda C_{torque}. \tag{3.39}$$

3.3.2.3 Double multiple streamtube model

This method was proposed by (PARASCHIVOIU, 1981) and it combines multiple streamtube and double actuator disk theory, Figure 3.5(c) (LAPLIN, 1975). As presented

in Figure 3.5(d), it is possible to observe multiple streamtubes as presented by MSTM, but in addiction, it is possible to identify upwind and downwind parts of the rotor. This model allows variations of the aerodynamic loads and torque with the blade position for each part of the rotor (PARASCHIVOIU, 1981).

In comparison with the previous two models, double multiple streamtube model gives a better correlation between calculated and experiment results, however, under high solidity and high tip speed ratios, this model shall have its precision further improved (JIN et al., 2015). In the following sections, this model will be discussed thoroughly.

From double actuator disk theory is possible to notice that upstream wind speed v_{up} is not equal to wind speed on blade v_{ind1} (front) and v_{ind2} (back), and also differ from wind speed at central part of rotor v_e, as well as downstream v_{dw} by induction factors a_1 and a_2. In order to obtain these velocities, Figure 3.5(c) is used. As result:

$$v_{ind1} = a_1 v_{up}, \tag{3.40}$$

$$v_e = 2a_1 - 1, \tag{3.41}$$

$$v_{ind2} = a_2 v_e, \tag{3.42}$$

where a_1, a_2 are respectively upstream induction factor, downstream induction factor.

In this method the upstream region is defined by $(0, \pi)$ and downstream region between $(\pi, 2\pi)$. So, each streamtube swept area is different from one side to another, and they are calculated as:

$$s_{1,st} = rh\Delta\theta sin(\theta_i), \tag{3.43}$$

$$s_{2,st} = rh\Delta\theta(-sin(\theta_i)). \tag{3.44}$$

The same idea is applicable from equation (3.18) to equation (3.33). So, using the equations presented in section 3.3.1 in each side of rotor, thrust force coefficients are defined as:

$$C_{t,up,i} = \frac{\sigma}{\pi sin(\theta)} \frac{v_{ind1}^2}{v_{up}^2} \left(c_d cos(\beta) - c_l sin(\beta)\right), \tag{3.45}$$

$$C_{t,dw,i} = \frac{-\sigma}{\pi sin(\theta)} \frac{v_{ind2}^2}{v_{up}^2 \left(2a_1 - 1\right)^2} \left(c_d cos(\beta) - c_l sin(\beta)\right), \tag{3.46}$$

where σ is called solidity $\sigma = \frac{N_{blades} c}{2r}$.

Finally, the total power coefficient can be given by sum of power coefficient from both sides of rotor, as showed below:

$$C_{p,up} = \frac{\sigma\lambda}{2\pi}\sum_{0}^{\pi} C_{torque,up}, \tag{3.47}$$

$$C_{p,dw} = \frac{\sigma\lambda}{2\pi}\sum_{\pi}^{2\pi} C_{torque,dw}, \tag{3.48}$$

$$C_p = C_{p,up} + C_{p,dw}. \tag{3.49}$$

3.3.2.4 Dynamic stall

According to (SCHEURICH, 2011), dynamic stall can occur when the angle of attack transiently exceeds the static angle of the airfoil sections of the rotor blade. Since the maximum angle of attack experienced by the blades increases when the tip speed ratio of the turbine decreases, dynamic stall becomes increasingly important at lower tip speed ratios. The dynamic stall can also occur at high tip speed ratios when the angle of attack on the blade is locally increased by interactions between the blades of the rotor and the vortices within the wake that is generated by the turbine. (ISLAM et al., 2008) said that the dynamic stall is the dominant unsteady phenomenon that affects overall VAWT performance. It occurs when the blade?s angle of attack changes rapidly with time. Dynamic stall prediction methods used by helicopters, aircrafts and wind turbines are based on semi-empirical approaches, initially introduced by (GORMONT, 1973). In the case of vertical-axis Darrieus wind turbines, as the turbine blades rotate, the local angle of attack changes continuously with time. At the lower tip speed ratio, the angle of attack exceeds the staling angle in most of the stations, thus the dynamic stalling effects need to be considered in the analysis.

In this thesis it will be used the modified Gormont model proposed by (BERG, 1983). According to (KOZAC; VALLVERDU, 2014) this model gives a good relation between accuracy and computational expense. The Gormont method consists of applying a hysteresis delay $\delta\alpha$ to the angle of attack. After applying this delay, the resulting reference angle of attack α_{ref} behaves according to the model:

$$\alpha_{ref} = \alpha - K\delta\alpha, \tag{3.50}$$

with K enforcing the asymmetric behaviour of the hysteresis delay:

$$K = \begin{cases} 1 : \dot{\alpha} \geq 0 \\ -0.5 : \dot{\alpha} < 0 \end{cases} \tag{3.51}$$

when the absolute value of the angle of attack is increasing, the hysteresis delay is twice of what observed when it is decreasing, all other variables being the same in

magnitude. The term $\delta\alpha$ is proportional to the non-dimensional rate parameter:

$$S = \sqrt{\left|\frac{c\dot{\alpha}}{2v_{rel}}\right|}, \tag{3.52}$$

with S being interpreted as the square root of the velocity of the blade's leading or trailing edge as it rotates around its half chord point with respect to the relative wind velocity. This serves to take into account the blade's movement to the relative wind when calculating the magnitude of the hysteresis delay. The slope of $\delta\alpha$ vs. S decreases both with thickness over chord ratio. Therefore, as the blade thickness with respect to the chord length increases, the hysteresis delay will drop as well. Once the delayed angle of attack has found α_{ref}, the modified lift and drag coefficients can be calculated. The lift coefficient is calculated using the potential equation with a modified slope m:

$$c_l^{dyn} = c_{l,0}\left(\alpha_0\right) + m\left(\alpha - \alpha_0\right), \tag{3.53}$$

where α_0 is the angle of attack at zero lift, m is the minimum value of either the slope of the linear portion of the lift curve or the value of $\frac{c_l\left(\alpha_{ref}\right)-c_l(\alpha_0)}{\alpha_{ref}-\alpha_0}$. The drag coefficient is obtained simply by using α_{ref} to extract it from the available static data,

$$c_d^{dyn} = c_d\left(\alpha_{ref}\right). \tag{3.54}$$

This method, so far, is purely Gormont's, which was designed for use in modelling helicopter rotor performance. Berg's modification takes into account the fact that helicopter blades operate at much lower angles of attack than that of a VAWT, which typically operates at angles of attack far higher than the stall angle of attack α_{ss}. Therefore, Berg theorized that Gormont's method was likely to over-predict the lift and drag for high angles of attack. As a result, the following modification for lift is introduced, so that it tends to the static values for very high values of α, deep into non linear regime:

$$c_l^{mod} = \begin{cases} c_l + \left[\frac{A_M\alpha_{ss}-\alpha}{A_M\alpha_{ss}-\alpha_{ss}}\right]\left(c_l^{dyn} - c_l\right) : \alpha \leq A_M\alpha_{ss} \\ c_l : \alpha > A_M\alpha_{ss} \end{cases} \tag{3.55}$$

,

with A_M define by user, but Berg defined the best value for the correction parameter is $A_M = 6$.

3.3.3 Algorithm

The procedure applied to simulate VAWT is based on code presented by (VALLVERDU, 2014). Initially based on wind turbine parameters, wind speed and tip speed ratio, the induction factor a is computed for various azimuthal angle between 0 and π,

and then from π to 2π.

The process of convergence for upstream induction factor a_1 starts setting $a_1 = 1$ and then computing induced velocity, relative velocity, flight path angle, angle of attack, lift and drag coefficients. So, the thrust coefficient is calculated according to equation 3.45 and this result is compared to:

$$C_t = \begin{Bmatrix} 4a(1-a) & a \geq 0.7167 \\ 2.0544 - 1.7333a & a < 0.7167 \end{Bmatrix}, \tag{3.56}$$

for a convergence interval between 0 and 1, until these equations become equal using as basis a defined error.

The same procedure is covered to obtain downstream induction factor a_2. However, calculated a_1 is considered, in order to get the induced velocity. Other change is the equation used to defined thrust coefficient, that is equation 3.46.

After both a_1 and a_2 defined, it is possible to obtain induced velocities for entire rotor, as well as the angles. In that stage, the dynamic stall equations are applied to acquire lift and drag coefficients as consequence forces. And finally, the front and back power coefficients are calculated. This explanation is illustrated in Figure 3.8.

3.4 CONCLUSION

In this chapter was discussed about the forces and velocities that act in VAWT rotor. The blade element momentum theory was introduced, together with streamtube model equations, in order to estimate the torque, thrust and power coefficient. Besides, an short review was presented about other models that predict VAWT performance.

Figure 3.8 – Simulation flow chart.

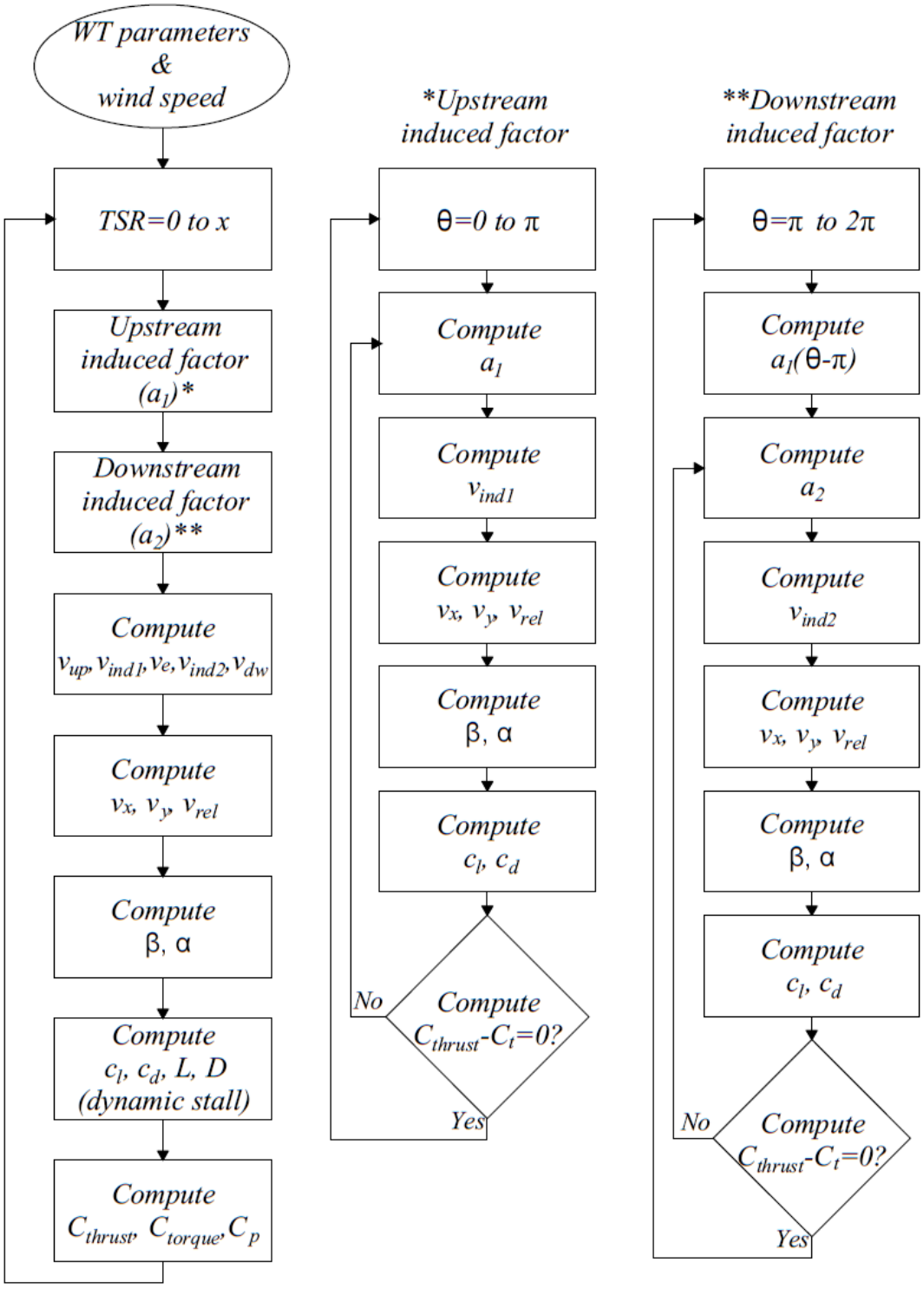

Source: Author.

4 CASE STUDY

4.1 INTRODUCTION

This chapter will introduce the wind turbine used for this work. Curves of power and coefficient of power provided by manufacturer are presented. Also, the initial setup to obtain some parameters of turbine's Permanent Magnet Synchronous Machine (PMSM) such as Back-EMF constant (K_e), number of pole pairs (pp), stator resistance (R_s) and stator inductance (L_s), direct-axis inductance (L_d), quadrature-axis inductance (L_q) are described in detail. Finally, it shows the site and its issues, where wind turbine is installed.

4.2 WIND TURBINE CHARACTERISTICS

This study is based in a straight bladed vertical axis wind turbine (see Figure 4.1). This turbine has a 1.5 kW PMSM and was designed to operate under turbulent envi-

Figure 4.1 – Razec wind turbine.

Source: Author.

ronment conditions, it can receive wind from any point and it has low noise production, being suitable for urban areas (at the rooftop of the buildings). Next, table 4.1 presents some characteristics of the wind turbine.

Table 4.1 – Enersud Razec266 main parameters.

Description	Value
Power	1.5 $kW (at\ 12\ m/s)$
Rotational speed	60 *to* 180 rpm
Cut-in	2.2 m/s
Start generate at	4.0 m/s
Diameter	2.0 m
Blade length	2.66 m
Blade chord length	0.32595 m

Source: Adapted from (ENERSUD, 2017).

The blade profile is approximated by NACA 4418. Its lift and drag coefficient curves are present in Figure 4.2, obtained using the XFoil webpage. These coefficient curves will be used to derive an aerodynamic model for this vertical-axis wind turbine.

Figure 4.2 – Lift and drag coefficients.

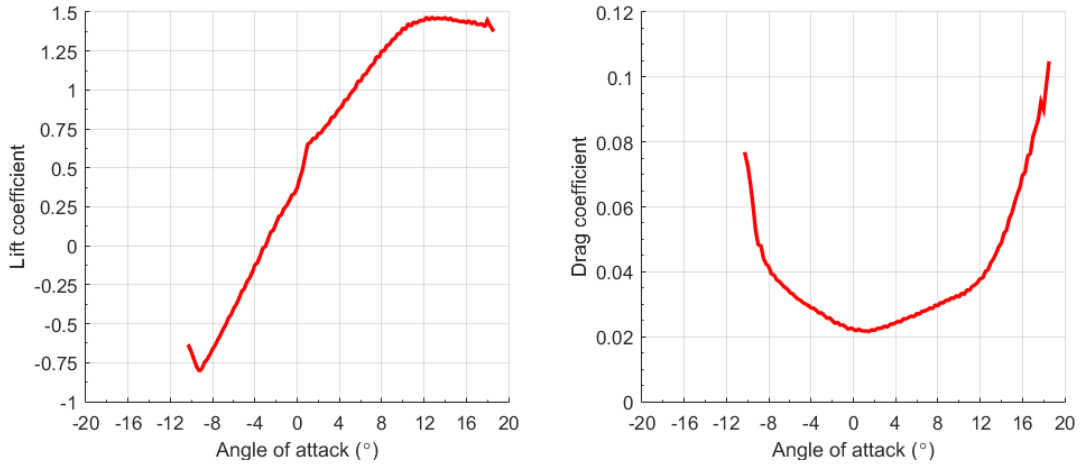

Source: Adapted from XFoil website.

In order to get the main parameters of the generator for the wind turbine simulation, a test bench (see Figure 4.3) was built. The test bench is composed by the PMSM tied in a wood structure. The generator was driven by a three phase induction motor. Information about the motor can be seen in Table 4.2.

Figure 4.3 – Test bench.

Source: Author.

Table 4.2 – Motor characteristics.

	Specifications
Model	$21MAR05BR09259$
Frequency	60 Hz
Phases	3
rotational speed	0 to 1755 rpm
Power	9.2 kW
$\frac{I_p}{I_n}$	8.7
$cos(\phi)$	0.82
Efficiency	0.885
Y	220 V/33.3 A
Δ	380 V/19.3 A

Source: Author.

First the no-load test was carried out. The study applied speed from zero to 250 rpm, and measured the RMS line voltage. With 250 rpm the measured voltage was approximately 612.58 V, converting it to RMS phase voltage dividing by 1.73 the result is 354.09 V. The hole curve obtain from this test is highlighted in Figure 4.4.

From Figure 4.4 it is possible to get the equation that relates line voltage with rotational velocity as close to a straight line. The equation is:

$$V_f = 2.4787\omega + 4.5319, \tag{4.1}$$

where the angular coefficient is the Back-EMF constant equals to 2.4787 V/rpm or 23.6743

Figure 4.4 – No load test.

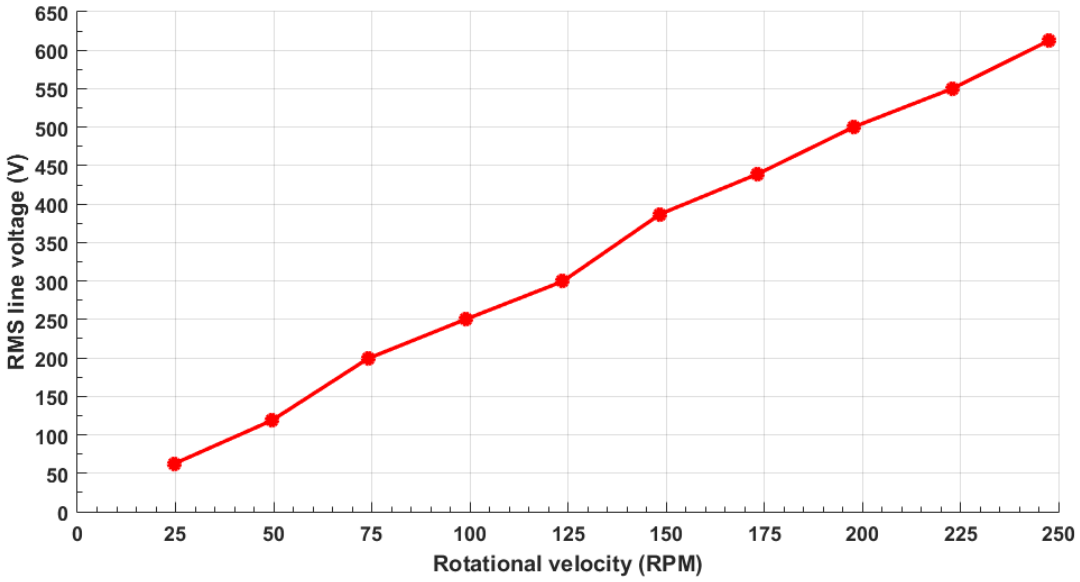

Source: Author.

Vs/rad. Having this constant, it is possible through equation (4.2) to calculate the induced voltage to each rotational velocity.

$$E_f = 23.6743\omega. \tag{4.2}$$

Now, to get the number of pole pairs, the permanent magnet synchronous machine was driven to nearly 49.5 rpm, and the line to line voltage frequency was measured, and it was found to be equal to 15 Hz. Putting these numbers into equation (4.3), 18 pole pairs was the obtained result.

$$pp = \frac{60f}{n} = \frac{60 \cdot 15}{49.5} = 18.18 \approx 18. \tag{4.3}$$

About stator resistance, initially the DC resistance was measured between phases, resulting in 33 Ω. Since this generator's topology is Y-connection, it is just necessary to divide it by two. So stator resistance is equals to 16.5 Ω.

To calculate the direct-axis inductance follow steps were executed:

In order to obtain the inductances, the procedure described in (BOBEK, 2013) was used. To calculate the direct-axis inductance, the following steps were executed:

- Align the rotor to phase A connecting phase A to positive potential of source voltage and phases B and C are grounded;
- Lock the rotor shaft;
- Apply negative step voltage. Phase A is grounded and phases B and C are connected to the positive potential of source voltage;

- Measure the step response of the current (see Figure 4.5);
- Calculate direct-axis inductance using 4.4.

$$L_d = \frac{2}{3}\tau R = \frac{2}{3}.893\ \mu.33 = 19.6\ mH, \tag{4.4}$$

where τ is the time constant took from Figure 4.5.

Figure 4.5 – Current step response for Direct-axis inductance estimation.

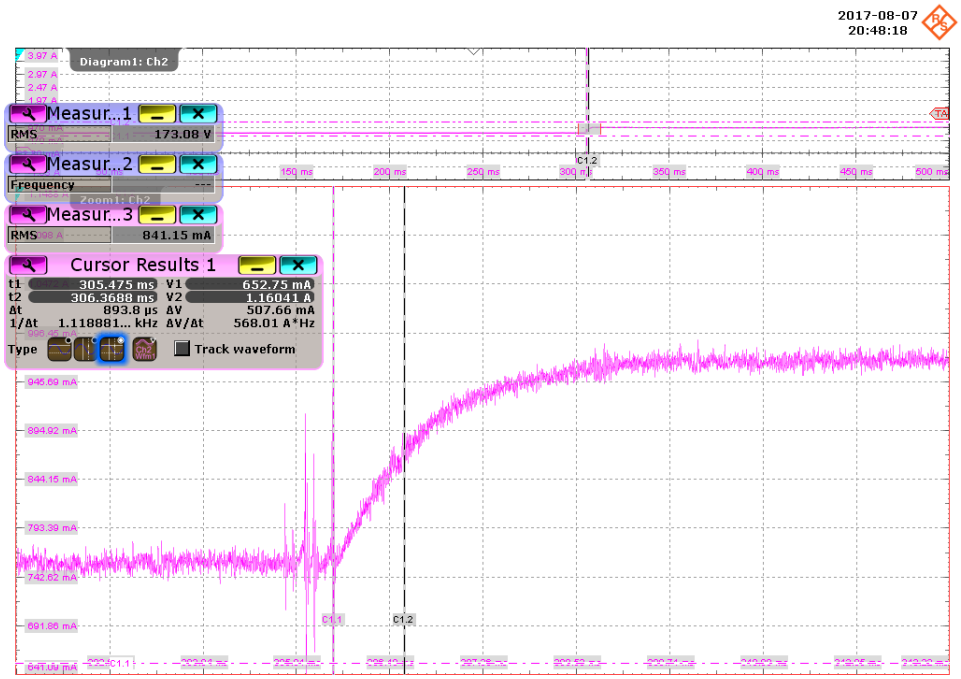

Source: Author.

Now, to calculate the quadrature-axis inductance, the steps conducted were:

- Align the rotor to the quadrature-axis connecting the phase B to the positive potential of the voltage source, and phase C is grounded while phase A is floating;
- Lock the rotor shaft firmly, because current step response in quadrature-axis creates torque; Generate a current step response (see Figure 4.6) in this configuration-phase A is connected to the positive potential of voltage source and phases B and C are grounded;
- Calculate inductance L_q in the same way as L_d.

$$L_q = \frac{2}{3}\tau R = \frac{2}{3}.1\ m.33 = 22\ mH. \tag{4.5}$$

Figure 4.6 – Current step response for Quadrature-axis inductance test.

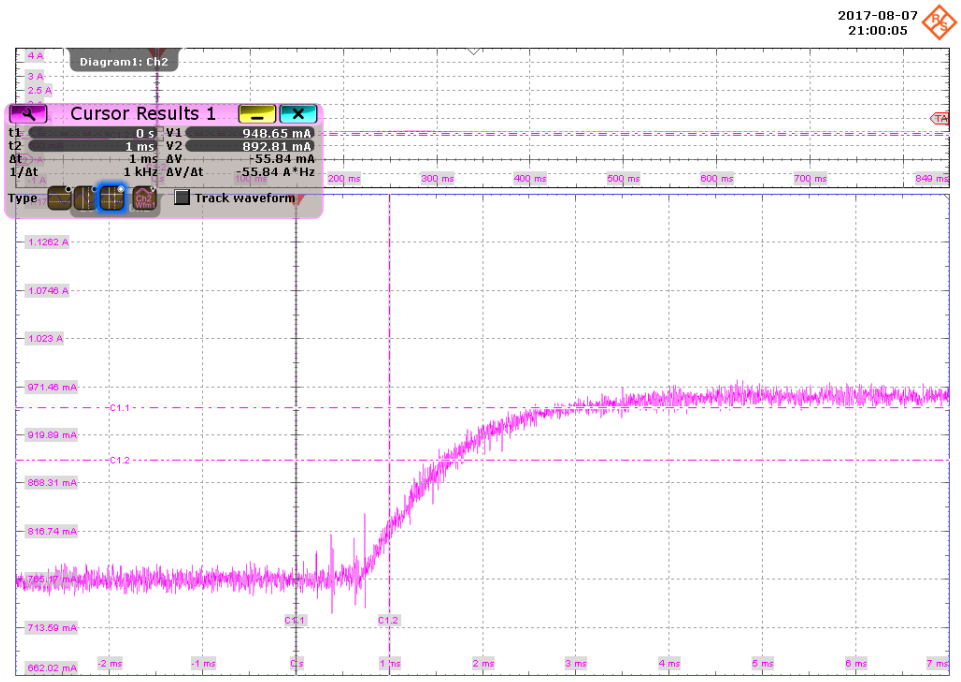

Source: Author.

Since it is a PMSM with non-salient poles, the quadrature and direct axis inductances are expected to be equal. So, let us consider the average of the estimated direct and quadrature axis inductances, which results in equation (4.6), that is:

$$L = \frac{L_d + L_q}{2} = \frac{19.6\ mH + 22\ mH}{2} = 20.8\ mH. \tag{4.6}$$

The table 4.3 presents the main PMSM required for simulation.

Table 4.3 – PMSM main parameters.

Description	Value
Power	1.5 kW (2.0 $kW short\ period$)
Phase voltage range	0 to 350 V_{ac}
Connection	$Three\ phase\ -\ Y$
Rotational speed	0 to 250 rpm
Starting torque	0.4 Nm
Moment of inertia	1.061 $kg\ m^2$
Pole pairs	18
Back-EMF constant	3505.4 $V_{peak}/krpm$
Stator resistance	16.5 Ω
Stator inductance	13.8739 mH
d-axis inductance	19.6309 mH
q-axis inductance	21.9780 mH

Source: Adapted from (ENERSUD, 2017).

The moment of inertia of WT will be estimated assuming a point mass, as a result, it is three times the mass a blade, times the square of the radius of the WT, which in this case, results in 46.8 kgm^2.

In addition, Figure 4.7 shows the power curve supplied by the manufacturer (ENERSUD, 2017).

Figure 4.7 – Manufacturer power curve of the wind turbine.

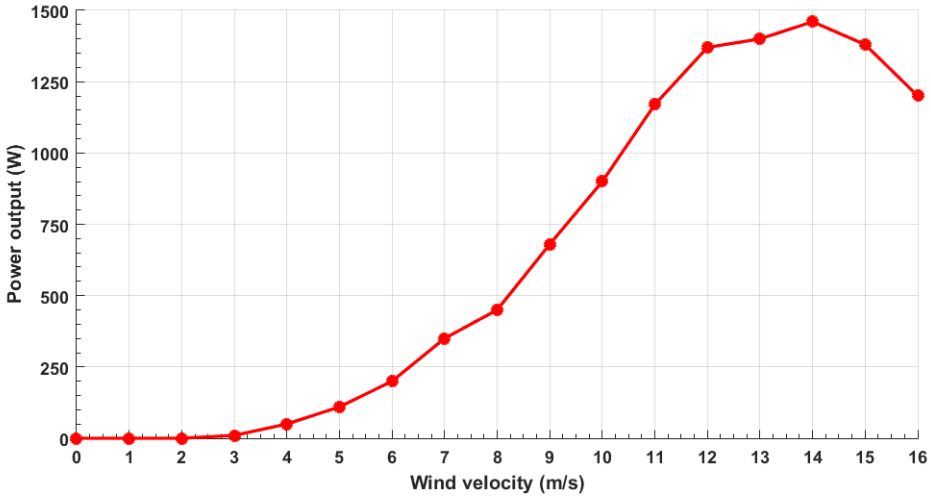

Source: Adapted from (ENERSUD, 2017).

From power curve it is possible to estimate the power coefficient (CP) of the wind

turbine (see in Figure 4.8) by ratio, between power generated by turbine (P) and power available in the wind ($P_0 = \frac{\rho s_e v_0^3}{2}$).

Figure 4.8 – Power coefficient.

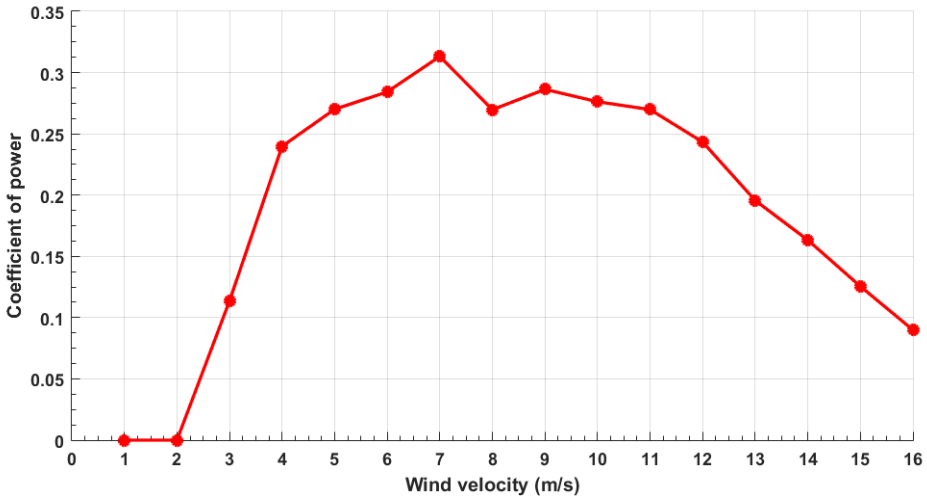

Source: Author.

4.3 WIND TURBINE SITE

The wind turbine is installed at rooftop of Federal University of Santa Maria Smart Grid Institute building (see the red circle in Figure 4.9) in Santa Maria-RS, Brazil (latitude 29°42′44.72”S longitude 53°43′10.88”O).

Figure 4.9 – UFSM campus.

Source: Adapted from Google Earth, 2018.

The average hourly wind speed in Santa Maria experiences mild seasonal variation over the course of the year. The windier part of the year lasts for 5.3 months, from July 4 to December 12, with average wind speed of 2.4 meters per second. The calmer time of the year lasts for 5.3 months, from December 12 to July 4. The wind is most often from the north for 1.2 months, from June 4 to July 10. The predominant wind direction are winds coming from east, for at least 11 months.

4.3.1 Site evaluation

Before starting the tests, it is necessary to define the local to install a weather station, in order to acquire wind direction and wind speed, and obstacles that influence the wind flux near turbine to establish which sectors around the wind turbine have to be avoided (measures to be ignored in final results).

About where to install weather station, it is necessary to observe wind direction and its frequency around the site. Looking at regional wind atlas (SCHUBERT; ELETROSUL, 2014), it was noticed high occurrence of wind coming from East and Southeast. Moreover, thinking about weather station maintenance and IEC 61400-12-1 (IEC, 2017) suggestion of installing weather station distant 2.5 times rotor diameter from wind turbine (in that case 5 meters), the local set in Figure 4.10 was chosen.

Figure 4.10 – Local evaluation.

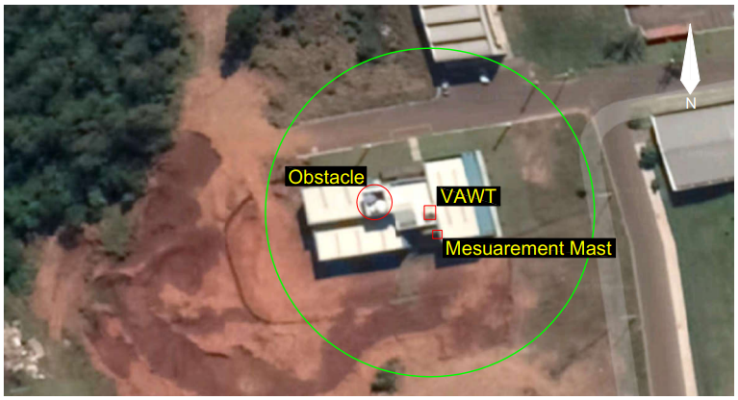

Source: Adapted from Google Earth, 2018.

In relation to obstacles and avoided sectors, the wind turbine and the meteorological mast cannot suffer influence from buildings, trees or other turbines. The obstacles should be located at certain distance in order to avoid the wake effect and measure error. For this reason, it is used a model of obstacle to evaluate the impact on wind turbine and meteorological mast, and then, it is calculate which direction should be ignored in final database. This influence is defined by IEC 61400-12-1.

The obstacles should be considered when inside a circumference twenty times rotor

diameter, 40 meters (green circle in Figure 4.10). At Northwest direction (approximately 169°), there are some building water tanks and its influence in wind flux coming from that direction needed to be analyzed. The obstacle wind flux disturbance in relation to wind turbine and meteorological mast is close to 10%. The limit allowed is less than 1%, so this obstacle needs to be counted. Other effect to take into account is the wake of wind turbine into a mast when the wind comes from north. After all considerations the avoided sectors are presented in Figure 4.11. Where the prohibited sectors (124°) are covered by red colour. The valid region is located between 18° and 254°.

Figure 4.11 – Prohibited sectors.

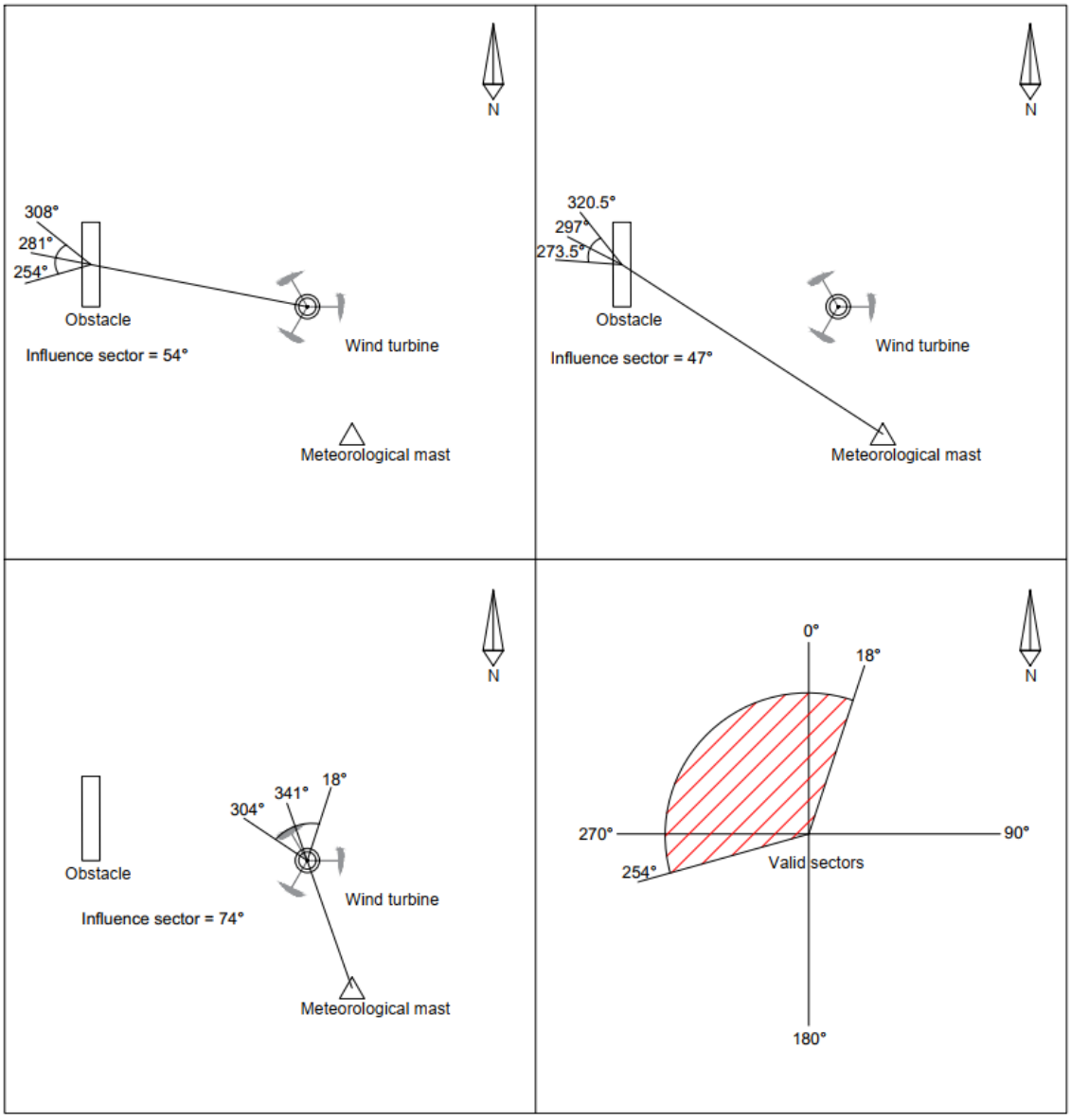

Source: Author

4.4 CONCLUSION

This chapter gives the main parameters of VAWT. Aspects about airfoil, such as lift and drag coefficients and its dimensions, were presented for the Enersud Razec266. In addition, a procedure was used to obtain the main generator parameters and the direct and quadrature inductances. Furthermore, a description of the site in which the wind turbine is installed is showed where has been identified a wind direction sector that has to be disregarded when determining the power curve experimentally.

In the next chapter, the power electronics modelling and control is presented.

5 MODELLING AND CONTROL

5.1 INTRODUCTION

This chapter will present the strategy to control the wind turbine introduced in chapter 4. First, equations of permanent magnet synchronous machine (PMSM) in abc, $\alpha\beta$, and dq coordinates are developed. A discrete-time sliding mode current observer and an adaptive electromotive force (EMF) observer to estimate PMSM rotational speed are showed. It is also showed an explanation about the method used for searching for the maximum power point of turbine, and also modelling of DC-DC converter for current and voltage control.

5.2 PROPOSED SCHEME

To accomplish the established objectives of this thesis, the scheme in Figure 5.1 is applied. Composing the project, there is a three phase wind generator connected to a non-controlled rectifier, to convert AC signals into DC ones. After that, there is a Boost converter (switches S_a and S_b) for controlling inductor current, that supplies a DC

Figure 5.1 – Proposed Scheme.

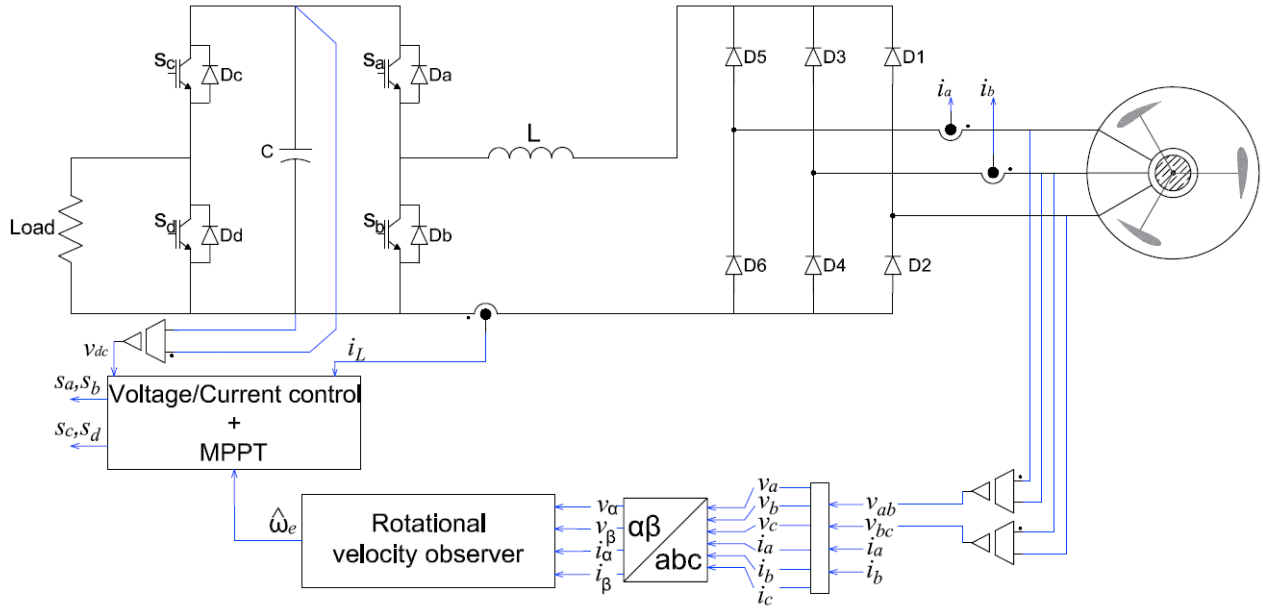

Source: Author.

bar. The capacitor voltage is controlled by switches S_c and S_d, by transferring power to the load. The MPPT technique is based on optimal torque and generator rotational speed. Using these pieces of information, it is possible to calculate the reference current for inductor current control. However, there is no way, in this case, to install mechanical sensors in order to measure generator rotational speed. So that, a speed observer is employed. In the next sections, all cited components are described in detail.

5.3 CONTINUOUS-TIME PERMANENT MAGNET SYNCHRONOUS MACHINE MODEL

5.3.1 Representation in *abc* coordinates

The Figure 5.2 shows the stator circuit of PMSM. Applying Kirchhoff's law on the circuit, the following equations are obtained in relation to stator and phase coordinates:

$$\begin{bmatrix} v_a \\ v_b \\ v_c \end{bmatrix} = \begin{bmatrix} R_s & 0 & 0 \\ 0 & R_s & 0 \\ 0 & 0 & R_s \end{bmatrix} \begin{bmatrix} i_a \\ i_b \\ i_c \end{bmatrix} + \frac{\mathrm{d}}{\mathrm{d}t} \begin{bmatrix} \varphi_a \\ \varphi_b \\ \varphi_c \end{bmatrix}, \tag{5.1}$$

$$\begin{bmatrix} \varphi_a \\ \varphi_b \\ \varphi_c \end{bmatrix} = \begin{bmatrix} L_a & M_{ab} & M_{ca} \\ M_{ab} & L_b & M_{bc} \\ M_{ca} & M_{bc} & L_c \end{bmatrix} \begin{bmatrix} i_a \\ i_b \\ i_c \end{bmatrix} + \begin{bmatrix} \varphi_a^r \\ \varphi_b^r \\ \varphi_c^r \end{bmatrix}, \tag{5.2}$$

where v_a, v_b, v_c are stator voltages, i_a, i_b, i_c are stator currents, φ_a, φ_b, φ_c are stator magnetic fluxes, φ_a^r, φ_b^r, φ_c^r are magnetic fluxes of rotor, R_s is stator resistance, L_a, L_b, L_c are stator inductances, M_{ab}, M_{bc}, M_{ca} are mutual inductances between stator phases.

Figure 5.2 – Stator circuit.

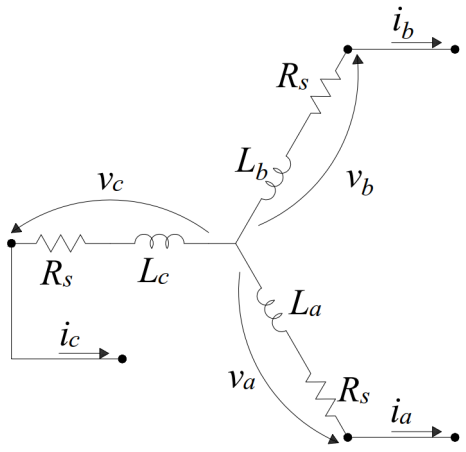

Source: Author.

Because that PMSM has non-salient poles, the definition of inductance can be simplified by neglecting the rotor lag, parameters that depends on the airgap and considering the airgap flux being constant. That action results in $\begin{bmatrix} L_a & L_b & L_c \end{bmatrix} = \begin{bmatrix} L_s & L_s & L_s \end{bmatrix}$ and $\begin{bmatrix} M_{ab} & M_{bc} & M_{ca} \end{bmatrix} = \begin{bmatrix} -\frac{1}{2}L_s & -\frac{1}{2}L_s & -\frac{1}{2}L_s \end{bmatrix}$. And according to (BOLDEA, 2005) the magnetic rotor flux can be described, disregarding its harmonics like:

$$\begin{aligned} \varphi_a^r &= \varphi_{pm} cos\left(\theta_e\right), \\ \varphi_b^r &= \varphi_{pm} cos\left(\theta_e - \frac{2\pi}{3}\right), \\ \varphi_c^r &= \varphi_{pm} cos\left(\theta_e + \frac{2\pi}{3}\right). \end{aligned} \tag{5.3}$$

To simplify the equations above, it is possible to describe then in a matrix notation as follow:

$$\mathbf{v_{abc}} = \mathbf{R_{abc}} \mathbf{i_{abc}} + \frac{d\varphi_{\mathbf{abc}}}{dt}, \tag{5.4}$$

$$\varphi_{\mathbf{abc}} = \mathbf{L_{abc}} \mathbf{i_{abc}} + \varphi_{\mathbf{abc}}^{\mathbf{r}}, \tag{5.5}$$

where $\mathbf{v_{abc}} = \begin{bmatrix} v_a & v_b & v_b \end{bmatrix}^T$, $\mathbf{i_{abc}} = \begin{bmatrix} i_a & i_b & i_c \end{bmatrix}^T$, $\varphi_{\mathbf{abc}} = \begin{bmatrix} \varphi_a & \varphi_b & \varphi_c \end{bmatrix}^T$, $\varphi_{\mathbf{abc}}^{\mathbf{r}} = \begin{bmatrix} \varphi_a^r & \varphi_b^r & \varphi_c^r \end{bmatrix}$.

After that, the power is defined by:

$$\begin{aligned} P_{in} &= \mathbf{i_{abc}^T} \mathbf{v_{abc}} \\ &= \mathbf{i_{abc}^T} \left(\mathbf{R_{abc}} \mathbf{i_{abc}} + \frac{d\theta_e}{d\theta_e} \frac{d\mathbf{L_{abc}}}{dt} \mathbf{i_{abc}} + \mathbf{L_{abc}} \frac{d\mathbf{i_{abc}}}{dt} + \frac{d\theta_e}{d\theta_e} \frac{d\varphi_{\mathbf{abc}}^{\mathbf{r}}}{dt} \right) \\ &= \mathbf{i_{abc}^T} \left(\mathbf{R_{abc}} \mathbf{i_{abc}} + \frac{d\theta_e}{dt} \frac{\partial \mathbf{L_{abc}}}{\partial \theta_e} \mathbf{i_{abc}} + \mathbf{L_{abc}} \frac{d\mathbf{i_{abc}}}{dt} + \frac{d\theta_e}{dt} \frac{\partial \varphi_{\mathbf{abc}}^{\mathbf{r}}}{\partial \theta_e} \right). \end{aligned} \tag{5.6}$$

$$P_{in} = \left(\mathbf{i_{abc}^T} \mathbf{R_{abc}} \mathbf{i_{abc}} \right) + \left[\frac{1}{2} \frac{d\left(\mathbf{i_{abc}^T} \mathbf{L_{abc}} \mathbf{i_{abc}} \right)}{dt} \right] + \left[\left(\frac{1}{2} \mathbf{i_{abc}^T} \frac{\partial \mathbf{L_{abc}}}{\partial \theta_e} \mathbf{i_{abc}} + \mathbf{i_{abc}^T} \frac{d\varphi_{\mathbf{abc}}^{\mathbf{r}}}{dt} \right) \omega_e \right]. \tag{5.7}$$

The equation (5.7) is obtained with the following equality,

$$\frac{\mathrm{d}\mathbf{i_{abc}^T}}{\mathrm{d}t} \mathbf{L_{abc}} \mathbf{i_{abc}} = \frac{1}{2} \frac{\mathrm{d}\left(\mathbf{i_{abc}^T} \mathbf{L_{abc}} \mathbf{i_{abc}} \right)}{\mathrm{d}t} - \frac{1}{2} \mathbf{i_{abc}^T} \frac{\partial \mathbf{L_{abc}}}{\partial \theta_e} \mathbf{i_{abc}} - \frac{\mathrm{d}\theta_e}{\mathrm{d}t}. \tag{5.8}$$

Note that, the equation (5.7) has three terms, which the first one is copper losses, P_{cl}, the second one is defined as stator inductances energy ratio, $\Delta E_{L_{abc}}$ and the last one means electromechanical power, P_{em}. Other form to write the electromechanical power

is:

$$P_{em} = T_{em}\omega_m, \tag{5.9}$$

where ω_m is the mechanical speed defined by, $\omega_m = \frac{\omega_e}{pp}$. pp is the number of pole pairs.

From earlier definitions the electromechanical torque is described by:

$$T_{em} = pp\left(\frac{1}{2}\mathbf{i}_{\mathbf{abc}}^{\mathbf{T}}\frac{\partial \mathbf{L}_{\mathbf{abc}}}{\partial \theta_e}\mathbf{i}_{\mathbf{abc}} + \mathbf{i}_{\mathbf{abc}}^{\mathbf{T}}\frac{d\varphi_{\mathbf{abc}}^{\mathbf{r}}}{dt}\right). \tag{5.10}$$

5.3.1.1 Notes

Some issues need be noticed regarding the presented modelling, according to (KRISHNAN, 2009):

- The stator windings in equilibrium;
- Motor magnet force has sinusoidal feature;
- Parametric changes and core losses are negligible;
- Inductances are associate with rotor position;

5.3.2 Representation in $\alpha\beta$ coordinates

In order to represent the PMSM model in $\alpha\beta$ coordinates (see Figure 5.3), the Clark transformation (CLARKE, 1948) was applied using equation (5.11) resulting at:

$$\mathbf{A}_{\alpha\beta} = \frac{2}{3}\begin{bmatrix} 1 & -\frac{1}{2} & -\frac{1}{2} \\ 0 & \frac{\sqrt{3}}{2} & -\frac{\sqrt{3}}{2} \\ \frac{1}{2} & \frac{1}{2} & \frac{1}{2} \end{bmatrix}. \tag{5.11}$$

$$\mathbf{v}_{\alpha\beta} = \mathbf{A}_{\alpha\beta}\mathbf{v}_{\mathbf{abc}}, \tag{5.12}$$

$$\mathbf{i}_{\alpha\beta} = \mathbf{A}_{\alpha\beta}\mathbf{i}_{\mathbf{abc}}, \tag{5.13}$$

$$\varphi_{\alpha\beta} = \mathbf{A}_{\alpha\beta}\varphi_{\mathbf{abc}}, \tag{5.14}$$

$$\varphi_{\alpha\beta}^{\mathbf{r}} = \mathbf{A}_{\alpha\beta}\varphi_{\mathbf{abc}}^{\mathbf{r}}, \tag{5.15}$$

where $\mathbf{v}_{\alpha\beta} = \begin{bmatrix} v_\alpha & v_\beta \end{bmatrix}^T$, $\mathbf{i}_{\alpha\beta} = \begin{bmatrix} i_\alpha & i_\beta \end{bmatrix}^T$, $\varphi_{\alpha\beta} = \begin{bmatrix} \varphi_\alpha & \varphi_\beta \end{bmatrix}^T$, $\varphi_{\alpha\beta}^{\mathbf{r}} = \begin{bmatrix} \varphi_\alpha^r & \varphi_\beta^r \end{bmatrix}^T$. And considering PMSM a balanced system $\sum_{x=a,b,c} i_x = 0$, the zero component can be ignored.

With presented equations, the PMSM can be defined as follows:

Figure 5.3 – abc to $\alpha\beta$.

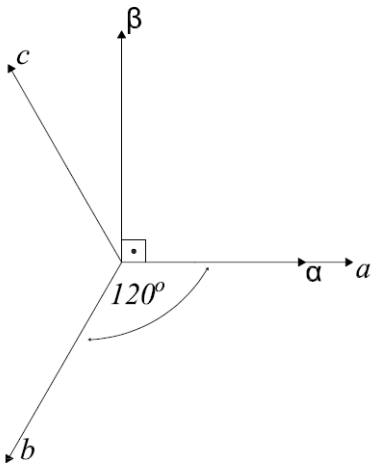

Source: Author.

$$\mathbf{v}_{\alpha\beta} = \mathbf{R}_{\alpha\beta}\mathbf{i}_{\alpha\beta} + \frac{d\varphi_{\alpha\beta}}{dt}, \tag{5.16}$$

$$\varphi_{\alpha\beta} = \mathbf{L}_{\alpha\beta}\mathbf{i}_{\alpha\beta} + \varphi^{\mathbf{r}}_{\alpha\beta}, \tag{5.17}$$

where $\varphi^{\mathbf{r}}_{\alpha\beta} = \varphi_{pm}\begin{bmatrix} cos\left(\theta_e\right) & sin\left(\theta_e\right)\end{bmatrix}^T$, $\mathbf{R}_{\alpha\beta} = \frac{3}{2}\begin{bmatrix} R_s & 0 \\ 0 & R_s\end{bmatrix}$ and $\mathbf{L}_{\alpha\beta} = \frac{3}{2}\begin{bmatrix} L_s & 0 \\ 0 & L_s\end{bmatrix}$.

The current dynamic behave is presented in equation (5.18):

$$\frac{d\mathbf{i}_{\alpha\beta}}{dt} = \eta\mathbf{i}_{\alpha\beta} + \gamma\mathbf{v}_{\alpha\beta} - \gamma\mathbf{e}_{\alpha\beta}, \tag{5.18}$$

where $\mathbf{e}_{\alpha\beta} = \varphi_{pm}\omega_e\begin{bmatrix} -sin\left(\theta_e\right) & cos\left(\theta_e\right)\end{bmatrix}^T$, $\eta = \begin{bmatrix} -\frac{R_s}{L_s} & 0 \\ 0 & -\frac{R_s}{L_s}\end{bmatrix}$ and $\gamma = \begin{bmatrix} \frac{1}{L_s} & 0 \\ 0 & \frac{1}{L_s}\end{bmatrix}$.

Similar as earlier, the power goes on:

$$P_{in} = \frac{3}{2}\mathbf{i}^{\mathbf{T}}_{\alpha\beta}\mathbf{v}_{\alpha\beta}, \tag{5.19}$$

so that, the resulting terms look like:

$$P_{cl} = \frac{3}{2}R_s\left(i_\alpha^2 + i_\beta^2\right), \tag{5.20}$$

$$\begin{aligned} P_{em} &= \frac{3}{2}\left(\frac{1}{2}\mathbf{i}^{\mathbf{T}}_{\alpha\beta}\frac{\partial\mathbf{L}_{\alpha\beta}}{\partial\theta_e}\mathbf{i}_{\alpha\beta} + \mathbf{i}^{\mathbf{T}}_{\alpha\beta}\frac{\partial\varphi^{\mathbf{r}}_{\alpha\beta}}{\partial\theta_e}\right)\omega_e \\ &= \frac{3}{2}\omega_e\left(\varphi_\alpha i_\beta - \varphi_\beta i_\alpha\right), \end{aligned} \tag{5.21}$$

and torque can be defined as:

$$\begin{aligned} T_{em} &= \frac{3}{2}pp\left(\frac{1}{2}\mathbf{i}_{\alpha\beta}^{\mathbf{T}}\frac{\partial \mathbf{L}_{\alpha\beta}}{\partial \theta_e}\mathbf{i}_{\alpha\beta} + \mathbf{i}_{\alpha\beta}^{\mathbf{T}}\frac{\partial \varphi_{\alpha\beta}^{\mathbf{r}}}{\partial \theta_e}\right) \\ &= \frac{3}{2}pp\left(\varphi_\alpha i_\beta - \varphi_\beta i_\alpha\right). \end{aligned} \tag{5.22}$$

5.3.3 Representation in dq coordinates

In order to represent the PMSM model in dq coordinates, Park transformation (PARK, 1929) was applied from equation (5.23) to convert $\alpha\beta$ to dq and converting sinusoidal objects into continuous ones as well as decoupling variables. dq PMSM model is presented below:

$$\mathbf{A_{dq}} = \begin{bmatrix} cos\left(\theta_e\right) & sin\left(\theta_e\right) \\ -sin\left(\theta_e\right) & cos\left(\theta_e\right) \end{bmatrix}. \tag{5.23}$$

$$\mathbf{v_{dq}} = \mathbf{A_{dq}}\mathbf{v}_{\alpha\beta}, \tag{5.24}$$

$$\mathbf{i_{dq}} = \mathbf{A_{dq}}\mathbf{i}_{\alpha\beta}, \tag{5.25}$$

$$\varphi_{\mathbf{dq}} = \mathbf{A_{dq}}\varphi_{\alpha\beta}, \tag{5.26}$$

where $\mathbf{v_{dq}} = [v_d\ v_q]^T$, $\mathbf{i_{dq}} = [i_d\ i_q]^T$, $\varphi_{\mathbf{dq}} = [\varphi_d\ \varphi_q]^T$.

$$\mathbf{v_{dq}} = \mathbf{R_s}\mathbf{i_{dq}} + \omega_e\mathbf{j}\varphi_{\mathbf{dq}} + \frac{d\varphi_{\mathbf{dq}}}{dt}, \tag{5.27}$$

$$\varphi_{\mathbf{dq}} = \mathbf{L_{dq}}\mathbf{i_{dq}} + \varphi_{\mathbf{dq}}^{\mathbf{r}}, \tag{5.28}$$

Figure 5.4 – $\alpha\beta$ to dq.

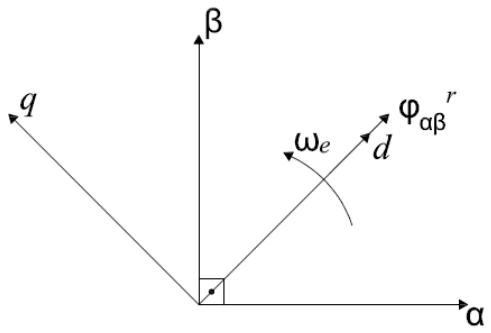

Source: Author.

where $\mathbf{j} = \begin{bmatrix} 0 & -1 \\ 1 & 0 \end{bmatrix}$, $\mathbf{L_{dq}} = \begin{bmatrix} L_d & 0 \\ 0 & L_q \end{bmatrix}$, $L_d \approx L_q = \frac{3}{2}L_s$.

Applying $\varphi_{\mathbf{dq}}$ in $\mathbf{v_{dq}}$ and after some manipulations, it is possible to define the current dynamic as presented up next:

$$\frac{di_{dq}}{dt} = \begin{bmatrix} -\frac{R_s}{L_d} & \frac{\omega_e L_q}{L_d} \\ -\frac{\omega_e L_d}{L_q} & -\frac{R_s}{L_q} \end{bmatrix} i_{dq} + \begin{bmatrix} \frac{1}{L_d} & 0 \\ 0 & \frac{1}{L_q} \end{bmatrix} v_{dq} - \begin{bmatrix} 0 \\ \frac{\varphi_{pm}}{L_q} \end{bmatrix} \omega_e. \tag{5.29}$$

The equation (5.29) introduced what is seen at Figure 5.5, where dq axis are decoupled.

Figure 5.5 – Decouple dq circuits.

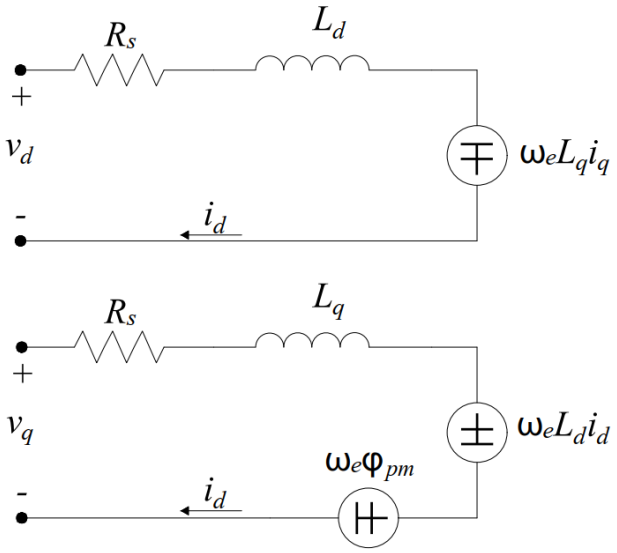

Source: Author.

The cooper losses, power and torque are defined as follows:

$$P_{cl} = \frac{3}{2}R_s\left(i_d^2 + i_q^2\right), \tag{5.30}$$

$$P_{em} = \frac{3}{2}\omega_e\left(\varphi_d i_q - \varphi_q i_d\right), \tag{5.31}$$

$$\begin{aligned} T_{em} &= \frac{3}{2}pp\left(\varphi_d i_q - \varphi_q i_d\right) \\ &= \frac{3}{2}pp\left[\varphi_{pm} + \left(L_d - L_q\right) i_d\right] i_q \\ &= \frac{3}{2}pp\varphi_{pm} i_q. \end{aligned} \tag{5.32}$$

The equation (5.32) can be simplify, because there are non-salient poles, $L_d \approx L_q$.

5.4 DISCRETE-TIME ROTATIONAL SPEED OBSERVER

To calculate the generator speed based on (BERNARDES et al., 2014; KOCH et al., 2015) works, the schemes introduced in Figure 5.6 were employed. Each block of earlier figure is explained below. However, firstly, the model of PMSM in discrete-time is presented.

5.4.1 Discrete-time $\alpha\beta$ coordinates PMSM model

The PMSM model on discrete-time can be obtained applying Euler's method to equation (5.18) resulting in:

$$\mathbf{i}_{\alpha\beta}(k+1) = \mathbf{i}_{\alpha\beta}(k) + T_s\eta\mathbf{i}_{\alpha\beta}(k) + T_s\gamma\mathbf{v}_{\alpha\beta}(k) - T_s\gamma\mathbf{e}_{\alpha\beta}(k). \tag{5.33}$$

where $\mathbf{v}_{\alpha\beta}(k) = \begin{bmatrix} v_\alpha(k) & v_\beta(k) \end{bmatrix}^T$, $\mathbf{i}_{\alpha\beta}(k) = \begin{bmatrix} i_\alpha(k) & i_\beta(k) \end{bmatrix}^T$, $\mathbf{e}_{\alpha\beta}(k) = \begin{bmatrix} e_\alpha(k) & e_\beta(k) \end{bmatrix}^T$.

The discrete-time EMF is given by:

Figure 5.6 – Rotational velocity observer

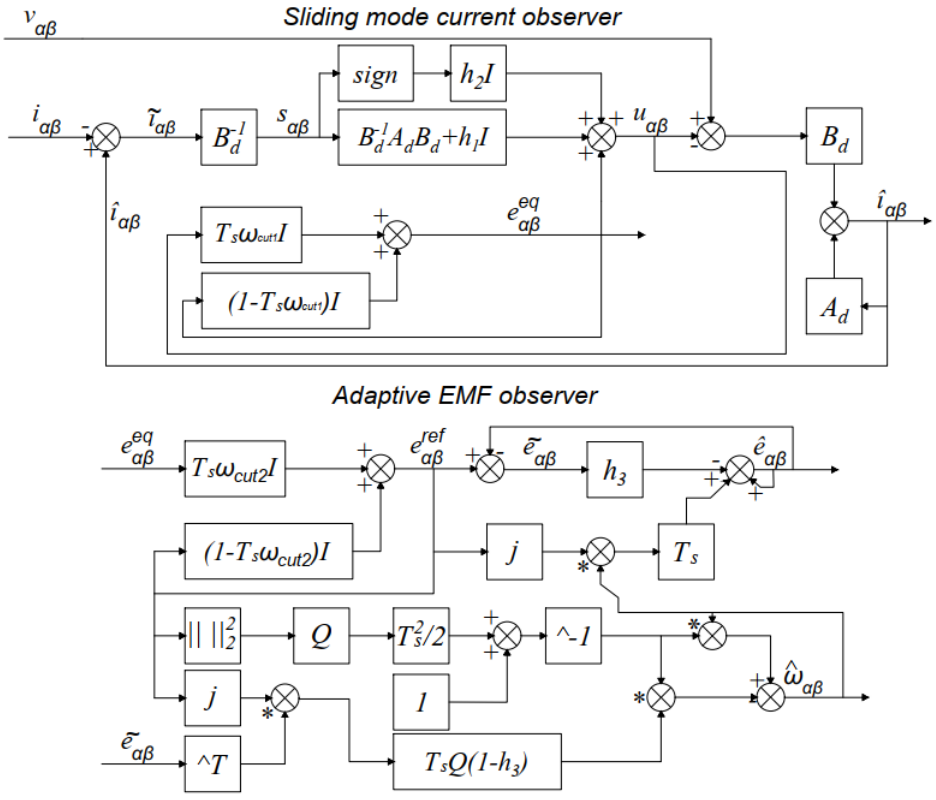

Source: Author.

$$\mathbf{e}_{\alpha\beta}(k) = \varphi_{pm}\omega_e(k) \begin{bmatrix} -sin\left(\theta_e\left(k\right)\right) \\ cos\left(\theta_e\left(k\right)\right) \end{bmatrix}. \tag{5.34}$$

Take into account that dynamic of $\Delta\omega_e\left(k\right)$ is much slower compared to electric variables, the rotor position can be defined as follows:

$$\theta_e\left(k\right) = tan^{-1}\left(-\frac{e_\alpha\left(k\right)}{e_\beta\left(k\right)}\right). \tag{5.35}$$

The next sections explain the sliding mode and adaptive observer.

5.4.2 Sliding mode current observer

The current observer is proposed as

$$\hat{\mathbf{i}}_{\alpha\beta}(k+1) = \mathbf{A_d}\hat{\mathbf{i}}_{\alpha\beta}(k) + \mathbf{B_d}\mathbf{v}_{\alpha\beta}(k) - \mathbf{B_d}\mathbf{u}_{\alpha\beta}(k) \tag{5.36}$$

with $\hat{\mathbf{i}}_{\alpha\beta}$ being the estimated current and $\mathbf{u}_{\alpha\beta}$ representing the attraction function, which is defined as follows:

$$\mathbf{u}_{\alpha\beta}(k) = \mathbf{e}_{\alpha\beta}{}^{eq}(k) + (\mathbf{B_d}{}^{-1}\mathbf{A_d}\mathbf{B_d} + h1\mathbf{I})\mathbf{s}_{\alpha\beta}(k) + h2\mathbf{I}sign(\mathbf{s}_{\alpha\beta}(k)), \tag{5.37}$$

where h_1 and h_2, $\mathbf{e}_{\alpha\beta}{}^{eq}$, $\mathbf{s}_{\alpha\beta}$ and $sign(\mathbf{s}_{\alpha\beta}(k))$ are respectively positive gains, amounts to actual EMF, sliding function and signal function.

The sliding function can be defined as

$$\mathbf{s}_{\alpha\beta}(k) = \mathbf{B_d}{}^{-1}\tilde{\mathbf{i}}_{\alpha\beta}(k), \tag{5.38}$$

which the current estimation error equals to $\tilde{\mathbf{i}}_{\alpha\beta}(k) = \hat{\mathbf{i}}_{\alpha\beta}(k) - \mathbf{i}_{\alpha\beta}(k)$.

To ensure the convergence of the current observer equation, the sliding conditions shall be verified. (SARPTURK; ISTEFANOPULOS; KAYNAK, 1987) proposes the inequalities

$$\left(s_j(k+1) - s_j(k)\right) sign\left(s_j(k)\right) < 0, \tag{5.39}$$

$$\left(s_j(k+1) + s_j(k)\right) sign\left(s_j(k)\right) \geq 0 \tag{5.40}$$

in order to assure both quasi sliding motion and convergence onto the j_{th} surface. The inequality (5.39) guarantees that the state trajectories point towards in a sliding surfaces

$s_j = 0$. On the other hand, the inequality (5.40) ensures that the chattering amplitude of the state trajectories decreases towards $s_j = 0$ or it remains limited to a sliding band. These inequalities are known as the sliding and convergence conditions. An alternative for equation (5.40) is

$$-s_j(k+1)sign\left(s_j(k)\right) < s_{jmax}, \tag{5.41}$$

for $|s_j(k)| \leq s_{jmax}$, where s_{jmax} is the sliding mode band. Therefore, whenever equations (5.39) and (5.41) are assured the state trajectories will enter and remain within the region defined by the sliding mode band.

The Theorem 1 establishes the bounds for sliding mode current observer gains the ensure quasi-sliding motion.

Theorem 1: Consider the current observer equation (5.36) subjected to the sliding function (5.38) and to the attraction function (5.37) where the low pass filter is neglected. The sliding function converges and remains in an attraction region around the surface $s_j = 0$ for a known s_{jmax} where $|s_j(k)| \leq s_{jmax}$, $i = \alpha\beta$, if the positive gain h_2 satisfies $max\left([1 \ -1-h_1]\,\mathbf{M}\right) \leq h_2 < min\left([1 \ 1-h_1]\,\mathbf{M}\right)$ where matrix M is defined by:

$$M = \begin{bmatrix} \tilde{e}_{\alpha max} & \tilde{e}_{\beta max} \\ s_{\alpha max} & s_{\beta max} \end{bmatrix} \tag{5.42}$$

for some positive gain h_1 with $\tilde{\mathbf{e}}_{\alpha\beta}(k) = \mathbf{e}_{\alpha\beta}{}^{eq}(k) - \mathbf{e}_{\alpha\beta}(k)$, where $||\tilde{e}_j(k)| \leq \tilde{e}_{j\ max}$ is the upper bound.

Proof: The difference equation of the estimated current error is given by

$$\tilde{\mathbf{i}}_{\alpha\beta}(k+1) = \mathbf{A_d}\tilde{\mathbf{i}}_{\alpha\beta}(k) + \mathbf{B_d}\mathbf{e}_{\alpha\beta}(k) - \mathbf{B_d}\mathbf{u}_{\alpha\beta}(k). \tag{5.43}$$

Hence, the dynamic behaviour of the sliding function can be calculated as

$$\mathbf{s}_{\alpha\beta}(k+1) = -\tilde{\mathbf{e}}_{\alpha\beta}(k)h_1\mathbf{I}\mathbf{s}_{\alpha\beta}(k) - h_2\mathbf{I}sign\left(\mathbf{s}_{\alpha\beta}(k)\right). \tag{5.44}$$

The conditions (5.39) and (5.41) for α-axis component that assure quasi sliding motion and convergence to the sliding mode band are:

$$-(1+h_1)||s_\alpha(k)|| - \tilde{e}_\alpha(k)sign\left(s_\alpha(k)\right) - h_2 < 0, \tag{5.45}$$

$$h_1 \parallel s_\alpha(k) + \tilde{e}_\alpha(k)sign\left(s_\alpha(k)\right) + h_2 \leq s_{\alpha max}. \tag{5.46}$$

By manipulating equations (5.45) and (5.46) is obtained

$$\tilde{e}_{\alpha max} - (1+h_1)S_{\alpha max} < h_2 \leq \tilde{e}_{\alpha max} + (1-h_1)S_{\alpha max}, \tag{5.47}$$

if $\tilde{e}_\alpha(k)$ and $s_\alpha(k)$ differ in their signs. A similar result can be obtained for β-axis compo-

nent. Hence, it is possible to infer that if $max\left([1\ \ -1-h_1]\,\mathbf{M}\right) \leq h_2 < min\left([1\ 1-h_1]\,\mathbf{M}\right)$ for some positive gain h_1, then the sliding function converges and remains in an attraction region around the $s_i = 0$ where s_{imax} is the sliding mode band.

Theorem 1 disregards the low pass filter dynamics, which can affect the observer stability. Then, in the following, its dynamic is included in the analysis.

The dynamic equation of the low pass filter is given by

$$\mathbf{e}_{\alpha\beta}{}^{eq}(k+1) = (1 - T_s w_{cut1})\mathbf{I}\mathbf{e}_{\alpha\beta}{}^{eq}(k) + T_s w_{cut1}\mathbf{I}\mathbf{u}_{\alpha\beta}(k), \tag{5.48}$$

where w_{cut1} is the cut off frequency of low pass filter 1. By using the attraction function (5.37) is becomes

$$\mathbf{e}_{\alpha\beta}{}^{eq}(k+1) = \mathbf{e}_{\alpha\beta}{}^{eq}(k) + T_s w_{cut1}\left(\mathbf{B_d}^{-1}\mathbf{A_d}\mathbf{B_d} + h_1\mathbf{I}\right)\mathbf{s}_{\alpha\beta}(k) + T_s w_{cut1} h_2 \mathbf{I} sign\left(\mathbf{s}_{\alpha\beta}(k)\right). \tag{5.49}$$

Hence, considering one axis component, the dynamic equations for sliding function and EMF, that described dynamic behaviour of the sliding mode current observer including low pass filter 1, are in matrix form

$$\begin{bmatrix} s(k+1) \\ \tilde{e}(k+1) \end{bmatrix} = \begin{bmatrix} -h_1 & -1 \\ T_s w_{cut1}\left(\mathbf{B_d}^{-1}\mathbf{A_d}\mathbf{B_d} + h_1\mathbf{I}\right) & 1 \end{bmatrix} \begin{bmatrix} s(k) \\ \tilde{e}(k) \end{bmatrix} + \begin{bmatrix} -h_2 & 0 \\ T_s w_{cut1} h_2 \mathbf{I} & -1 \end{bmatrix} \begin{bmatrix} sign\left(s(k)\right) \\ \Delta e(k) \end{bmatrix}, \tag{5.50}$$

where $\Delta e(k) = e(k+1) - e(k)$ denotes the difference between two successive samples of actual EMF and $\tilde{e}(k)$ is the estimation error of EMF. Equation (5.50) can be written in a compact form as

$$x(k+1) = \mathbf{G}x(k) + \mathbf{H_j} + \mathbf{H_2}p(k) \tag{5.51}$$

where the vector $x(k) = [s(k)\ \tilde{e}(k)]^T$ and the perturbation $p(k)$ is $\Delta e(k)$, and the matrices G, H_2 and H_i are respectively $G = \begin{bmatrix} -h_1 & -1 \\ T_s w_{cut1}\left(\mathbf{B_d}^{-1}\mathbf{A_d}\mathbf{B_d} + h_1\mathbf{I}\right) & 1 \end{bmatrix}$, $H_2 = \begin{bmatrix} 0 & -1 \end{bmatrix}^T$ and

$$H_j = \begin{cases} H_{1s+} = \begin{bmatrix} -h2 & T_s w_{cut1} h_2 \mathbf{I} \end{bmatrix}^T, s(k) > 0, \\ H_{1s-} = \begin{bmatrix} h_2 & -T_s w_{cut1} h_2 \mathbf{I} \end{bmatrix}, s(k) < 0. \end{cases} \tag{5.52}$$

The bounded input sequence $\left([1p(k)]^T\right)$ forces the switching linear system (5.51). Thus, if matrix $\mathbf{G}$ is Schur, then (5.51) is BIBO stable. Hence, the stability of sliding mode current observer is assured.

5.4.3 Adaptive EMF observer

This section describes the adaptive EMF observer using Lyapunov's Direct Method. The dynamic behaviour of EMF can be written as

$$\mathbf{e}_{\alpha\beta}(k+1) = \mathbf{e}_{\alpha\beta}(k) + T_s w_e(k+1)\mathbf{j}\mathbf{e}_{\alpha\beta}(k), \tag{5.53}$$

where the electric speed $w_e(k)$ has been considered, to vary slowly between two successive samples, i.e., $\Delta w_e(k) \approx 0$. Hence, the EMF observer can defined by

$$\hat{\mathbf{e}}_{\alpha\beta}(k+1) = \hat{\mathbf{e}}_{\alpha\beta}(k) + T_s \hat{w}_e(k+1)\mathbf{j}\mathbf{e}_{\alpha\beta}(k) - h_3\tilde{\mathbf{e}}_{\alpha\beta}(k), \tag{5.54}$$

where h_3 and $\hat{w}_e(k+1)$ denote a constant gain and the estimated rotor speed one step ahead, and $\tilde{\mathbf{e}}_{\alpha\beta}(k) = \hat{\mathbf{e}}_{\alpha\beta}(k) - \mathbf{e}_{\alpha\beta}(k)$ is the EMF estimated error, where the reference EMF ${\mathbf{e}_{\alpha\beta}}^{ref}(k)$ equals the actual EMF $\mathbf{e}_{\alpha\beta}(k)$. The reference EMF is defined by

$${\mathbf{e}_{\alpha\beta}}^{ref}(k+1) = (1 - T_s w_{cut2})\,\mathbf{I}{\mathbf{e}_{\alpha\beta}}^{ref}(k) + T_s w_{cut2}\mathbf{I}{\mathbf{e}_{\alpha\beta}}^{eq}(k), \tag{5.55}$$

where w_{cut2} is the cut off frequency low pass filter 2. Theorem 2 defines the adaptive law to estimate the rotor speed.

Theorem 2: Assuming $w_e(k)$ varies slowly between two successive samples and an adaptive law results in the following speed estimation error:

$$\tilde{w}_e(k+1) = \frac{\tilde{w}_e(k)}{1 + \frac{T_s^2}{2}Q\left\|\mathbf{e}_{\alpha\beta}(k)\right\|_2^2} - \frac{T_s Q\,(1-h_3)\left(\tilde{\mathbf{e}}_{\alpha\beta}^T(k)\mathbf{j}{\mathbf{e}_{\alpha\beta}}^T(k)\right)}{1 + \frac{T_s^2}{2}Q\left\|\mathbf{e}_{\alpha\beta}(k)\right\|_2^2}, \tag{5.56}$$

where Q denotes a positive gain. Hence, if the gain h_3 belongs to the range (0,2), then, the estimated EMF $\hat{\mathbf{e}}_{\alpha\beta}(k)$ and speed $\tilde{w}_e(k)$ converge to their actual $\mathbf{e}_{\alpha\beta}(k)$ and $w_e(k)$.

Proof: The dynamic behaviour of estimated EMF error given by

$$\tilde{\mathbf{e}}_{\alpha\beta}(k+1) = (1-h_3)\mathbf{I}\tilde{\mathbf{e}}_{\alpha\beta} + T_s\tilde{w}_e(k+1)\mathbf{j}\mathbf{e}_{\alpha\beta}, \tag{5.57}$$

where $\tilde{w}_e(k) = \hat{w}_e(k) - w_e(k)$ denotes estimated speed error. In addition, the candidate Lyapunov function

$$V(k) = \tilde{\mathbf{e}}_{\alpha\beta}^T(k)\tilde{\mathbf{e}}_{\alpha\beta}(k) + Q^{-1}\tilde{w}_e^2(k) \tag{5.58}$$

is chosen where Q is a positive constant. Then, the forward difference of Lyapunov function (5.58) can be written by

$$\Delta V(k) = \tilde{\mathbf{e}}_{\alpha\beta}^T(k+1)\mathbf{e}_{\alpha\beta}(k+1) - \tilde{\mathbf{e}}_{\alpha\beta}^T(k)\mathbf{e}_{\alpha\beta}(k) + Q^{-1}\left(\tilde{w}_e^2(k+1) - \tilde{w}_e^2(k)\right), \tag{5.59}$$

that must be negative in order to guarantee the stability of the adaptive EMF observer. Moreover, the estimated speed error variation is defined by $\Delta\tilde{w}_e(k) = \tilde{w}_e(k+1) - \tilde{w}_e(k)$ the leads to $\tilde{w}_e^2(k+1) - \tilde{w}_e^2(k) = -\Delta\tilde{w}_e^2(k) + 2\Delta\tilde{w}_e(k)\tilde{w}_e(k+1)$.

Hence, the Lyapunov function variation becomes

$$\begin{aligned}\Delta V(k) = \left[(1-h_3)^2 - 1\right] \left\|\tilde{\mathbf{e}}_{\alpha\beta}(k)\right\|_2^2 - Q^{-1}\Delta\tilde{w}_e^2(k) + \\ +2T_s(1-h_3)\tilde{w}_e(k+1)\tilde{\mathbf{e}}_{\alpha\beta}^T(k)\mathbf{j}\mathbf{e}_{\alpha\beta}(k) + T_s^2\left|\mathbf{e}_{\alpha\beta}(k)\right|_2^2\tilde{w}_e^2(k+1) + \\ +2Q^{-1}\Delta\tilde{w}_e(k)\tilde{w}_e(k+1)\end{aligned} \tag{5.60}$$

resulting in

$$\Delta V(k) = \left[(1-h_3)^2 - 1\right]\left|\tilde{\mathbf{e}}_{\alpha\beta}(k)\right|_2^2 - Q^{-1}\Delta\tilde{w}_e^2(k) \tag{5.61}$$

from the adaptive law (5.56).

In conclusion, if the gain h_3 belongs to the range (0,2), then (5.61) is negative. Therefore, the $\tilde{\mathbf{e}}_{\alpha\beta}(k)$ and $\tilde{w}_e(k)$ and the Lyapunov function (5.58) converge to zero. Hence, the adaptive EMF observer is stable.

In addition, from the speed estimation error, it is possible to write the following adaptive law:

$$\hat{w}_e(k+1) = \frac{\hat{w}_e(k)}{1 + \frac{T_s^2}{2}Q\left\|\mathbf{e}_{\alpha\beta}\right\|_2^2} - \frac{T_sQ(1-h_3)\left(\tilde{\mathbf{e}}_{\alpha\beta}^T(k)\mathbf{j}e_{\alpha\beta}(k)\right)}{1 + \frac{T_s^2}{2}Q\left\|\mathbf{e}_{\alpha\beta}\right\|_2^2}. \tag{5.62}$$

If necessary, it is possible to calculate the rotor's position as:

$$\hat{\theta}_e(k+1) = tan^{-1}\left(-\frac{\hat{e}_\alpha(k+1)}{\hat{e}_\beta(k+1)}\right) - \varsigma, \tag{5.63}$$

where

$$\varsigma = tan^{-1}\left(\frac{\hat{w}_e(k+1)}{w_{cut2}}\right) + \angle\left(\frac{\tilde{e}(z)}{w(z)}\right)_{z=e^{jT_s\hat{\omega}_e(k+1)}} \tag{5.64}$$

compensates the phase shift of both low pass filter and sliding mode current observer.

5.5 MAXIMUM POINT POWER TRACKING ALGORITHM

In order to extract the maximum performance of PMSM, the use of maximum power point tracking (MPPT) is needed. In literature, there were lots of algorithms to do it. (LI; SHI; MCLAREN, 2005; HUI; BAKHSHAI, 2008) presented respectively a neural network based and adaptive (modified hill climb) in order to extract maximum performance of wind turbines.

Another solution with good results, was proposed by (YAOQIN; ZHONGQING; BINGGANG, 2002) that showed a new MPPT control for PMSM driven by a three phase inverter and DC-BUS line. The results show that the proposed method can track as fast as 0.2 Hz wind speed variation and increases the output power by 48% considering proper comparison. (KOUTROULIS; KALAITZAKIS, 2006) showed a system based in a high efficiency DC-DC buck converter. No knowledge of the optimal characteristics of process and measurement of wind speed is required. The power increased by 11% to 50% compared to a generator connected via a rectifier to the battery bank. (TAFTICHT; AGBOSSOU; CHERITI, 2006) described a buck-boost converter used to achieve the maximum power performance of wind turbine driven a PMSM. The ratio between generation speed and the DC-BUS voltage is used to change the apparent DC-BUS voltage seen by the generator and thus the power from wind turbine settles down on the maximum power point. The efficiency is improved on average by 24%. (MOLINA; MERCADO, 2008) discussed a new control scheme of a three phase grid connected wind energy conversion system. The wind turbine generator consists of a variable speed wind turbine and the MPPT implemented via DC-DC boost converter. And (JEONG; SEUNG; LEE, 2012) proposed an method combining hysteresis control and tip speed ratio control using a power coefficient curve. Results show that the efficiency improved by 12% compared with typical tip speed ratio controller.

Here, the algorithm proposed by (HAQUE; NEGNEVITSKY; MUTTAQI, 2008) will be applied. This method is based on calculus of reference current to be controlled by boost converter. That current depends on optimal torque and PMSM speed, which in this case, is going to be observed.

Initially, toque can be defined as:

$$F_{torque} = \frac{P_{wt}}{\omega_m}, \tag{5.65}$$

where P_{wt} is the power generated described by:

$$P_{wt} = \frac{1}{2}\rho 2rhC_p v_{wind}^3, \tag{5.66}$$

with wind speed v_{wind} being calculated as:

$$v_{wind} = \frac{\omega_m r}{\lambda}. \tag{5.67}$$

So, replacing equations (5.66) and (5.67) in equation (5.65), the optimal torque F_{torque}^{ref} can be found by considering the maximum power coefficient C_{pmax}, maximum tip speed ratio $\lambda_{max}(C_{pmax})$, both obtained by aerodynamic simulation or practical tests, and also the observed speed $\hat{\omega}_e$.

$$F_{torque}^{ref} = K\hat{\omega}_e^2, \tag{5.68}$$

with the constant K given by:

$$K = \frac{\rho r^4 h C_p}{\lambda^3}. \tag{5.69}$$

Now, the power available in capacitor (see Figure 5.1) is calculated like:

$$P_{cap} = (i_L d)\, v_{dc}, \tag{5.70}$$

with d_1 being duty of switch S_a. Take into account no losses in PMSM and power converter, it is possible to match P_{wt} and P_{cap} resulting in the reference current to be controlled by boost converter:

$$i_L^{ref} = \frac{F_{torque}^{ref} \hat{\omega}_e}{d v_{dc}}. \tag{5.71}$$

The explained MPPT strategy is illustrated in Figure 5.7.

Figure 5.7 – MPPT diagram.

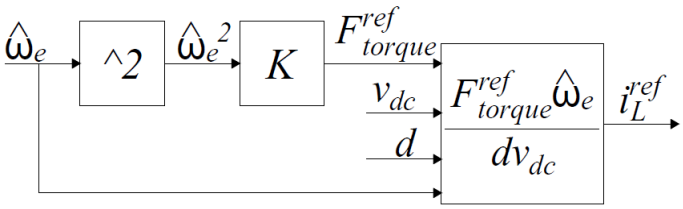

Source: Author.

5.6 MODELLING OF BOOST AND BUCK CONVERTERS

The next equations are developed according to Figure 5.8. The transfer function of boost converter (switches S_a and S_b) in function of duty cycle and inductor current is presented for later current control. Also, the transfer function of a buck converter (switches S_c and S_d) for further DC bar voltage control is illustrated.

5.6.1 Boost converter

Initially, considering switch S_a 'on' and S_b 'off', it is obtained the following equations:

$$\frac{\mathrm{d}i_L(t)}{\mathrm{d}t} = \frac{1}{L}(v_G(t) - v_{dc}(t)), \tag{5.72}$$

Figure 5.8 – Circuit.

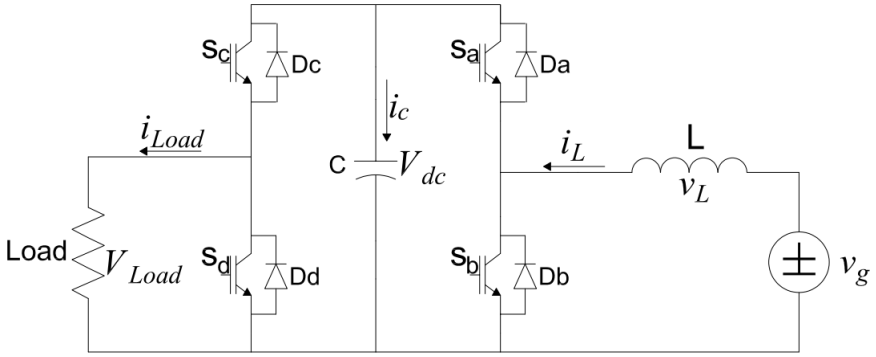

Source: Author.

$$\frac{\mathrm{d}v_{dc}(t)}{\mathrm{d}t} = \frac{1}{C}(i_L(t)). \tag{5.73}$$

Whereas switch S_a 'off' and S_b 'on', it result in:

$$\frac{\mathrm{d}i_L(t)}{\mathrm{d}t} = \frac{1}{L}v_G(t), \tag{5.74}$$

$$\frac{\mathrm{d}v_{dc}(t)}{\mathrm{d}t} = \frac{1}{C}(0). \tag{5.75}$$

Note that, switch S_a stays $d_1(t)\%$ of period 'on' and $1 - d_1(t)\%$ of period 'off', it is possible to rewrite equations (5.72) and (5.73) as function of duty cycle $d_1(t)$ as:

$$\frac{\mathrm{d}i_L(t)}{\mathrm{d}t} = \frac{1}{L}(v_G(t) - v_{dc}(t)d_1(t)), \tag{5.76}$$

$$\frac{\mathrm{d}v_{dc}(t)}{\mathrm{d}t} = \frac{1}{C}(i_L(t)d_1(t)). \tag{5.77}$$

From equations (5.76) and (5.77), it is noticed that this system is non-linear, because the duty cycle d is dependent of time. So that, it is necessary to establish an equilibrium point by assuming small oscillation around this point. Hence, the variables are composed by a steady state part and a small oscillation one. These variables are introduced below:

$$i_L(t) = I_L + \tilde{i}_L(t) \quad |I_L| \gg |\tilde{i}_L|, \tag{5.78}$$

$$v_{dc}(t) = V_{dc} + \tilde{v}_{dc}(t) \quad |v_{dc}| \gg |\tilde{v}_{dc}|, \tag{5.79}$$

$$v_G(t) = V_G + \tilde{v}_G(t) \quad |V_G| \gg |\tilde{v}_G|, \tag{5.80}$$

$$d_1(t) = D_1 + \tilde{d}_1(t) \quad |D_1| \gg |\tilde{d}_1|. \tag{5.81}$$

Substituting equations (5.78-5.81) into equations (5.76) and (5.77), it is obtained:

$$\frac{\mathrm{d}I_L}{\mathrm{d}t} + \frac{\mathrm{d}\tilde{i}_L(t)}{\mathrm{d}t} = \frac{1}{L}(V_G + \tilde{v}_{G(t)} - V_{dc}D_1 - V_{dc}\tilde{d}_1(t) - \tilde{v}_{dc}(t)D_1 - \tilde{v}_{dc}(t)\tilde{d}_1(t)), \tag{5.82}$$

$$\frac{\mathrm{d}V_{dc}}{\mathrm{d}t} + \frac{\mathrm{d}\tilde{v}_{dc}(t)}{\mathrm{d}t} = \frac{1}{C}(I_L D_1 + I_L\tilde{d}_1(t) + \tilde{i}_L(t)D_1 + \tilde{i}_L(t)\tilde{d}_1(t)). \tag{5.83}$$

In equations (5.82) and (5.83), the existence of constant term (steady state operation) is realized, first order and second order terms. Take into account that small oscillations are too small in relation to steady state, constant terms and second order ones going to be ignored, just analyzing first order terms, it results in:

$$\frac{\mathrm{d}\tilde{i}_L(t)}{\mathrm{d}t} = \frac{1}{L}(\tilde{v}_{G(t)} - V_{dc}\tilde{d}_1(t) - \tilde{v}_{dc}(t)D_1), \tag{5.84}$$

$$\frac{\mathrm{d}\tilde{v}_{dc}(t)}{\mathrm{d}t} = \frac{1}{C}(I_L\tilde{d}_1(t) + \tilde{i}_L(t)D_1). \tag{5.85}$$

Applying Laplace's transform in equations (5.84) and (5.85):

$$i_L(s) = \frac{1}{sL}(v_{G(s)} - V_{dc}d_1(s) - v_{dc}(s)D_1), \tag{5.86}$$

$$v_{dc}(s) = \frac{1}{sC}(I_L d_1(s) + i_L(s)D_1). \tag{5.87}$$

Isolating $v_c(s)$, in equation (5.87), and replacing into equation (5.86) and evaluating just the influence by duty cycle on inductor current, so $v_G(s) = 0$, it results in:

$$i_L(s) = \frac{1}{sL}\left[-V_{dc}d_1(s) - \left(\frac{I_L d_1(s)}{sC - D_1}\right)D_1\right]. \tag{5.88}$$

Putting equation (5.88) in transfer function format:

$$\frac{i_L(s)}{d_1(s)} = \frac{\left(-\frac{V_{dc}}{L}\right)s + \left[D_1\frac{(V_{dc}-I_L)}{(LC)}\right]}{s^2 - \left(\frac{D_1}{C}\right)s}. \tag{5.89}$$

Rewrite equation (5.89) in discrete-time by Euler:

$$\frac{i_L(z)}{d_1(z)} = \frac{\left(-\frac{V_{dc}}{T_s L}\right)z + \left(\frac{V_{dc}}{T_s L} + \frac{D_1 V_{dc}}{LC} - \frac{D_1 I_L}{LC}\right)}{\frac{z^2}{T_s^2} + \left(\frac{-2}{T_s^2} - \frac{D_1}{T_s C}\right)z + \left(1 + \frac{D_1 T_s}{C}\right)} \tag{5.90}$$

5.6.2 Buck converter

Considering switch S_c 'on' and S_d 'off', it is obtained:

$$\frac{\mathrm{d}v_{dc}(t)}{\mathrm{d}t} = \frac{1}{RC} v_{Load}(t), \tag{5.91}$$

with $v_{Load}(t)$ being equal to $v_{dc}(t)$.

If switch S_c is 'off' and S_d 'on':

$$\frac{\mathrm{d}v_{dc}(t)}{\mathrm{d}t} = \frac{1}{C}(0). \tag{5.92}$$

Considering switch S_c stays $d_2(t)\%$ of period 'on' and $1 - d_2(t)\%$ of period 'off', it is possible to rewrite equation (5.91) as function of duty cycle $d_2(t)$ as:

$$\frac{\mathrm{d}v_{dc}(t)}{\mathrm{d}t} = \frac{1}{RC} v_{dc}(t) d_2(t), \tag{5.93}$$

with $v_{Load}(t)$ being equal to $v_{dc}(t)d_2(t)$.

Using the same procedure applied to boost modelling, considering small oscillations, it is obtained:

$$\frac{\mathrm{d}\tilde{v}_{dc}(t)}{\mathrm{d}t} = \frac{1}{RC}\left(V_{dc}\tilde{d}_2(t) + \tilde{v}_{dc}(t) D_2\right). \tag{5.94}$$

Applying Laplace's transform in equation (5.94), it is obtained:

$$\frac{v_{dc}(s)}{d_2(s)} = \frac{\left(\frac{V_{dc}}{RC}\right)}{s - \left(\frac{D_2}{RC}\right)}. \tag{5.95}$$

Rewrite equation (5.95) in discrete-time by Euler:

$$\frac{v_{dc}(z)}{d_2(z)} = \frac{\left(\frac{T_s V_{dc}}{RC}\right)}{z - \left(1 + \left(\frac{T_s D_2}{RC}\right)\right)}. \tag{5.96}$$

5.6.3 Control schemes and nominal characteristics

Figures 5.9 and 5.10 illustrate schematics to control inductor current and capacitor voltage. The nominal characteristics of both converters are presented in Table 5.1.

The results regarding speed observer and control schemes will be discussed in chapter 6.

Figure 5.9 – Inductor current control.

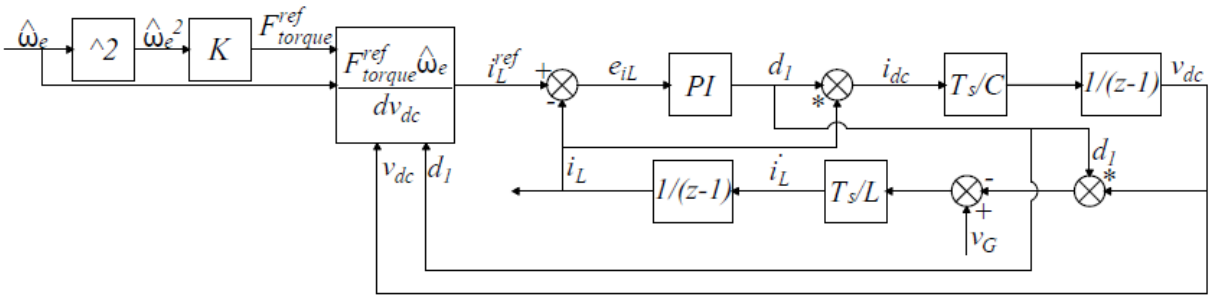

Source: Author.

Figure 5.10 – Capacitor voltage control.

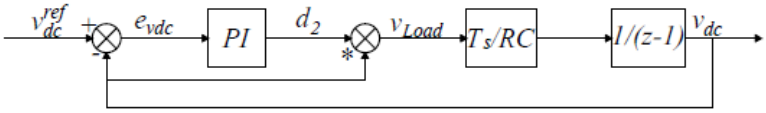

Source: Author.

Table 5.1 – Nominal parameters of converter.

Output power (P_{out})	1.5 kW
Input voltage (V_G)	350 V
Capacitor Voltage (V_C)	600 V
Switching frequency (f_s)	10 kHz
Inductor current (I_L)	2.5 A
Capacitance (C)	3300 μF
Inductance (L)	900 μH

Source: Author.

5.7 CONCLUSION

This chapter presented the utilized converter and proposed solution in order to control the wind turbine. The equations of PMSM were introduced, together with $\alpha\beta$ and dq coordinates. After that, the formulation to obtain the rotational speed and how to extract maximum performance of wind turbine were explained. In addition, modelling of power electronics were showed.

6 RESULTS AND DISCUSSION

6.1 INTRODUCTION

This section presents and analyzes the results of the contents introduced in earlier chapters. First of all, the numerical results associated with aerodynamic behavior, such as forces, velocities and output power are presented. After that, simulation of power converter is presented in order to evaluate control scheme and speed observer. Finally, a comparison among experimental, simulation and manufacturer data will be exposed. For details regarding practical assembly, see Appendix A.

6.2 AERODYNAMIC SIMULATION

This section presents the simulation results of the aerodynamic behavior that had been explained in chapter 3. The simulation uses data provided in chapter 4, such as chord length, blade length, rotor diameter and airfoil coefficients and so on. The goal is to study velocities and forces that act on turbine, in addition estimate its efficiency for further comparisons.

The simulation considers the number of streamtubes equal to 51, with the $\Delta\theta$ being approximately 0.0617 rad, hence the first azimuthal angle to be computed is 0.0308 rad. Due to lack of information about the behavior of lift and drag coefficients for high angles of attack, the tip speed ratio is simulated from 1.5 to 3. In all results, the front part of rotor is defined by azimuthal angle between 0° and 180°; and back part of rotor is defined from 180° to 360°. The wind speed is fixed at 12 m/s. This value corresponds to nominal operation of wind turbine.

6.2.1 Induction factor

The Figure 6.1 illustrates the induction factor a around 360° for various tip speed ratios. It is realized that, the higher the tip speed ratio is, minor is the induction factor. The induction factor is bigger in upstream than downstream zone. Around 180° this factor is bigger than one. This happened because the airfoil is pointed towards the wind, it would be as the wind was given an impulse to the airfoil, resulting in a rise of blade speed. Otherwise, when blade is on 0° it is completely against the wind and a tends to zero. This principle justifies the reason why induction factor is higher between 90° and

270° than 270° to 90°. Figure 6.2 shows an example of how induction factor influences other variables. It is possible to see the induced/flow velocity behaving similar to a. This effect will be noticed in subsequent results.

Figure 6.1 – Induction factor.

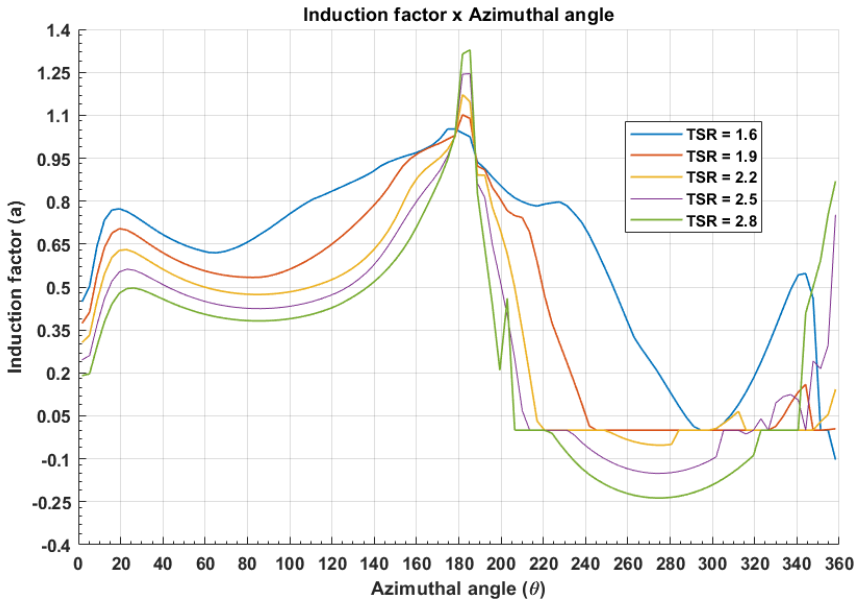

Source: Author.

Figure 6.2 – Induced/Flow velocity.

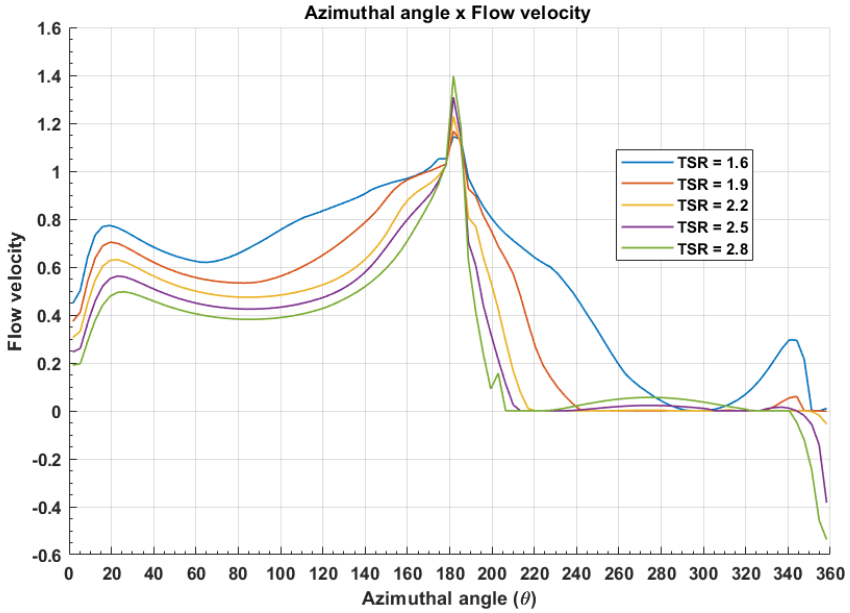

Source: Author.

6.2.2 Angle of attack

The angle of attack is strictly dependent on the blade azimuthal position and induced velocity. As can be noticed in Figure 6.3, the amplitude falls down with tip speed ratio growth.

Figure 6.3 – Angle of attack.

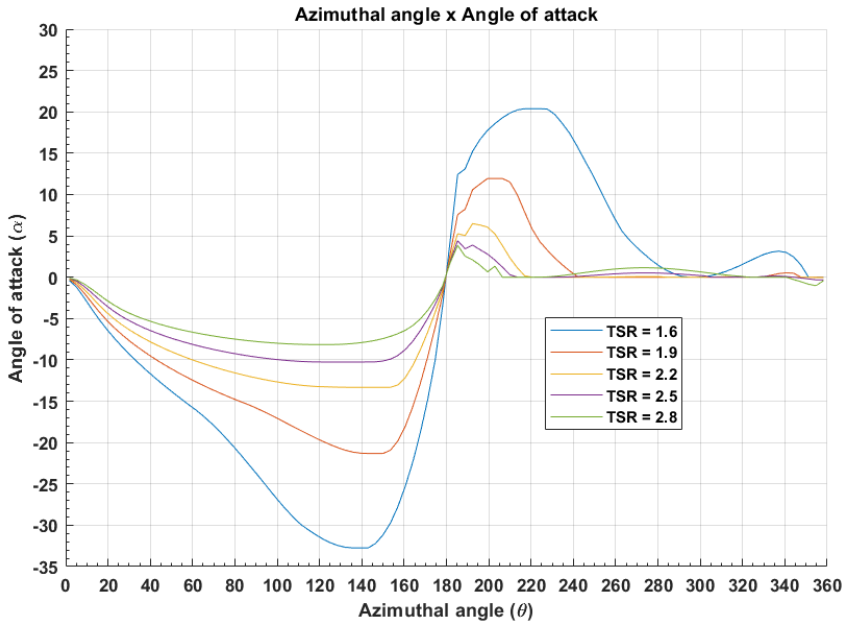

Source: Author.

The fact that the airfoil is asymmetric justifies different behaviours along azimuthal angle. It is important to emphasize the uncertainty associated with α out of available range, because this is going to influence lift and drag forces on the blade.

Figure 6.4 presents the effective angle of attack. Here, the effect of dynamic stall can be noticed. This variable is calculated by:

$$\alpha_{eff} = \frac{c_l}{c_{l\alpha}}, \tag{6.1}$$

with $c_{l\alpha}$ been the slope of linear part of lift coefficient curve. Using this variable is possible to identify non-linear zones during blade path around the rotor.

6.2.3 Forces

As cited before, induction factor and angle of attack influence whole turbine. Figures 6.5 and 6.6 show lift and drag during 360°, as well as its ratio (see Figure 6.7). The main feature is noticed in Figure 6.7, because negative part of L/D ratio is higher in mo-

Figure 6.4 – Effective angle of attack.

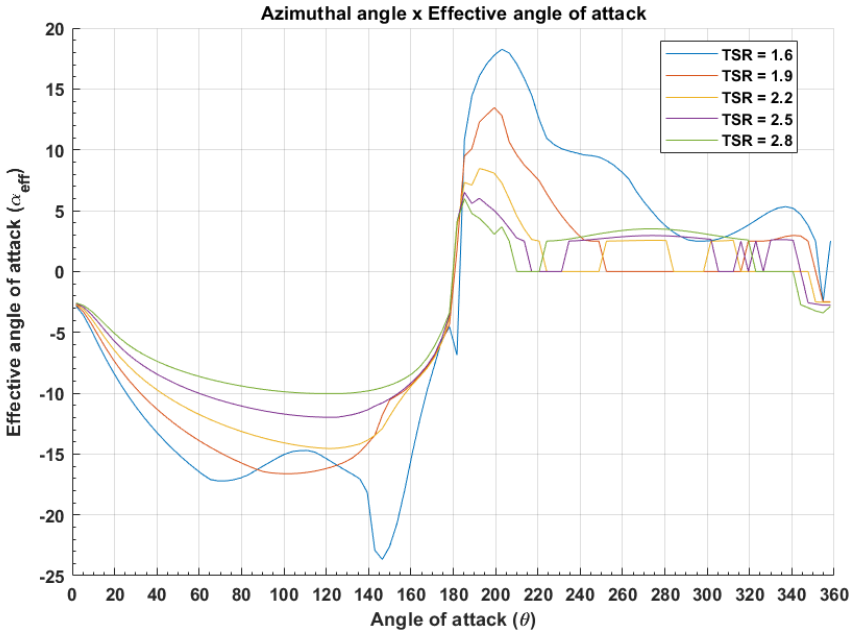

Source: Author.

dulus, than positive one. This means the turbine accelerates, because the drag influence is lower. Finally, Figure 6.8 illustrates how torque coefficient behaves for one blade at each azimuthal angle. It is realized that this turbine is able to start itself, because when each blade is between 0° and 180° the average torque coefficient is positive while the influence of downstream part of rotor is small. Also, the lower tip speed ratio is, the higher is the torque coefficient, showing the conclusion is reasonable.

6.2.4 Simulated power coefficient

Figure 6.9 presents the power coefficient in relation to tip speed ratio. As discussed, the induction factor in upstream is bigger than downstream, and this effect can be observed here. The green curve illustrates the power coefficient is higher in the front side than in the down side (blue curve). The total power coefficient is the combination of both, and it is described by the red line, which has its maximum value for tip speed ratio equals to 1.9 as 0.3972. This result was obtained by ignoring the wake effect and structural losses.

Figure 6.5 – Lift force.

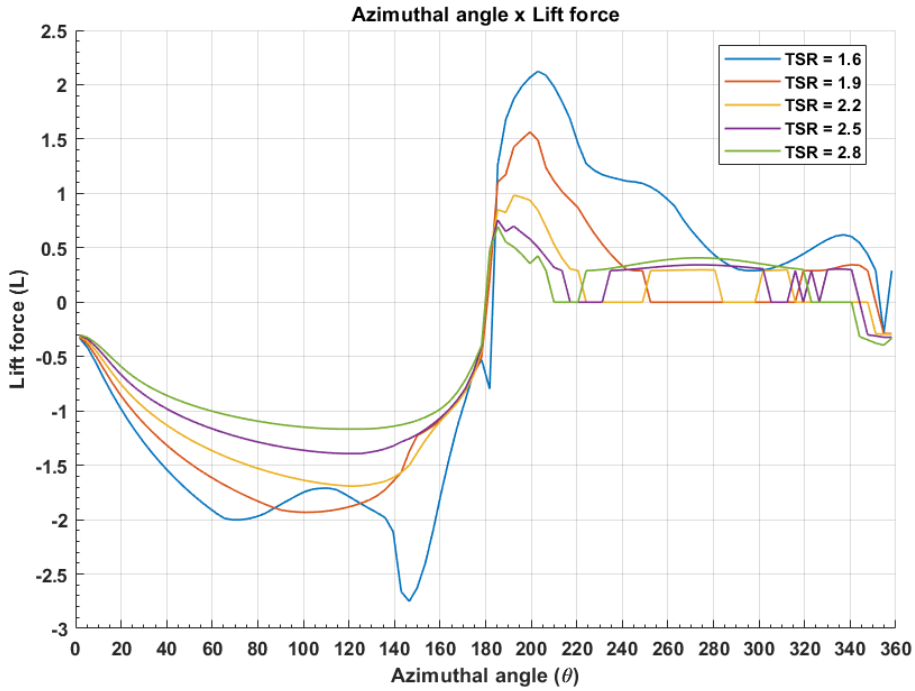

Source: Author.

Figure 6.6 – Drag force.

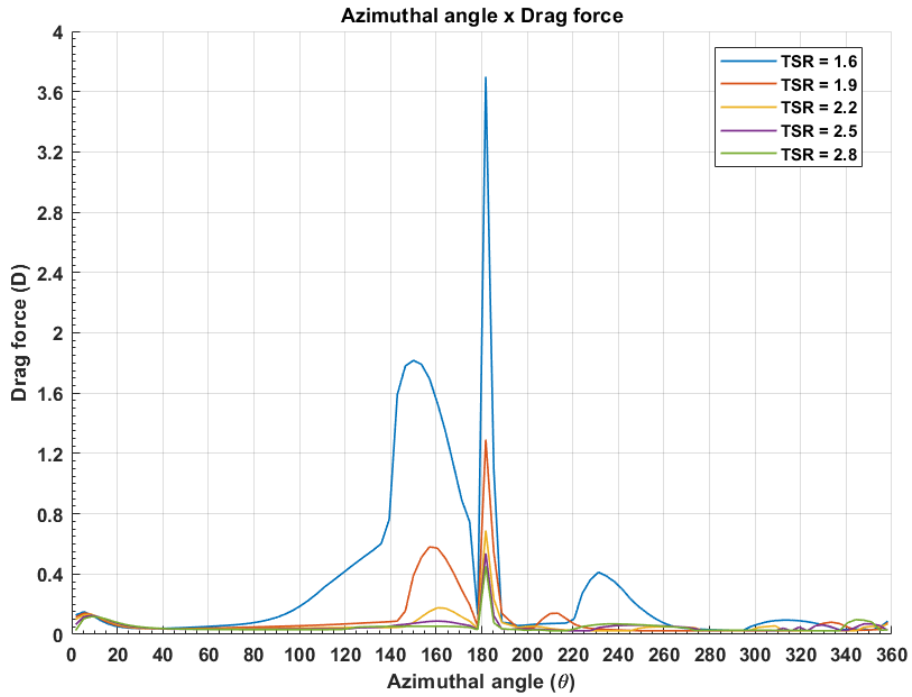

Source: Author.

Figure 6.7 – Lift/Drag.

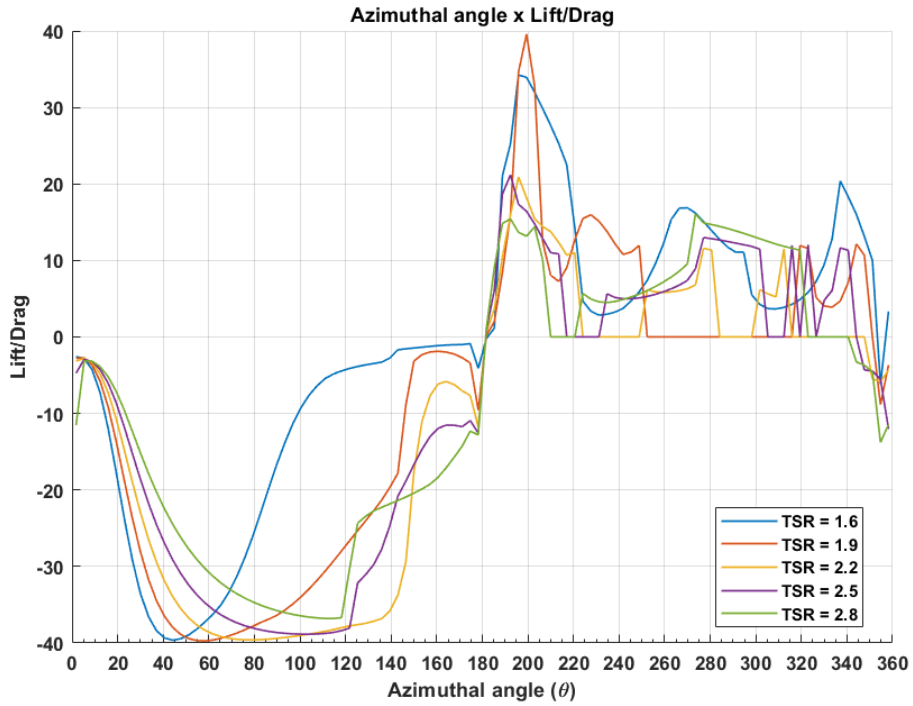

Source: Author.

Figure 6.8 – Torque coefficient.

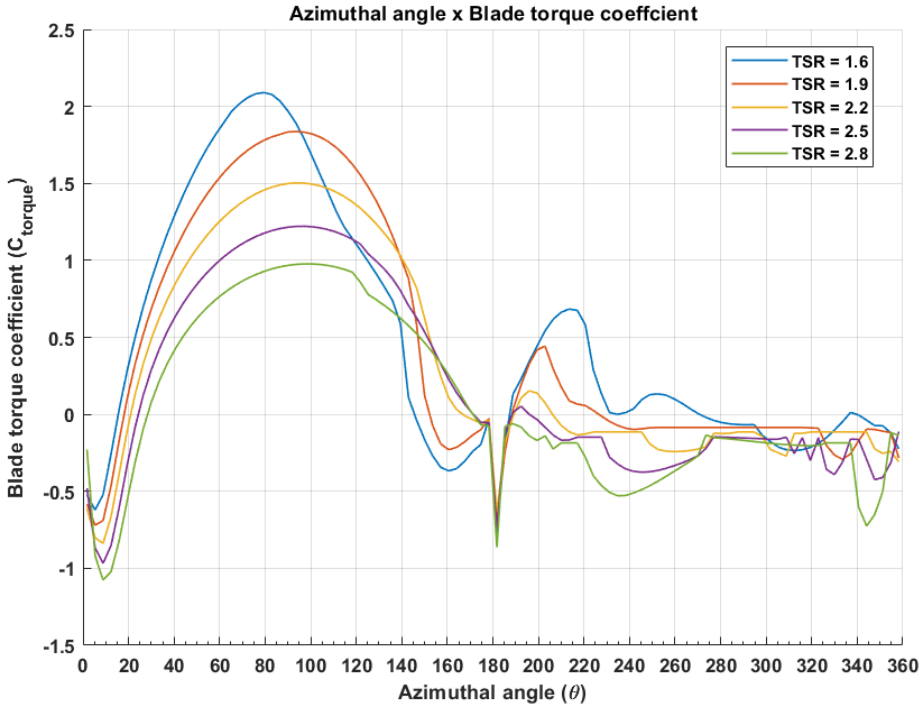

Source: Author.

6.3 POWER ELECTRONIC SIMULATION

This section will discuss the results related to the simulation of power electronic circuit using PSIM software. The simulation is presented for three different wind speeds.

Figure 6.9 – Power coefficient.

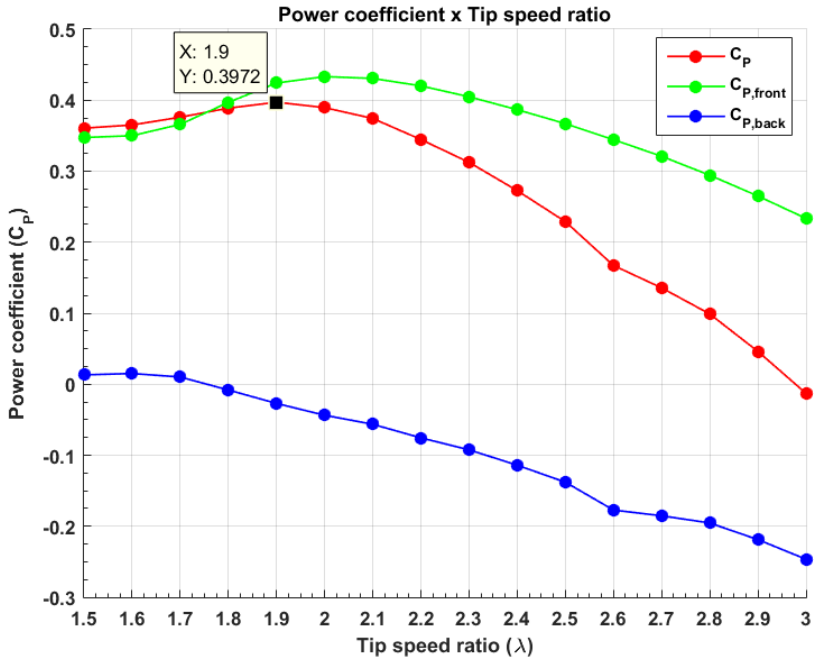

Source: Author.

Curves illustrating phase voltages and currents, generated power, observed speed/rotor position, reference torque, control of inductor current, capacitor voltage and power transferred to load will be discussed.

For this simulation, the data presented in chapters 4 and 5 are used. In addition, Table 6.1 presents speed observer gains. These gains were defined according to convergence conditions, explained during modelling of current and EMF observers, and also based on preliminary aerodynamic simulation tests.

Table 6.1 – Observer gains.

h_1	h_2	h_3	f_1	f_2	Q
2.0	1.0	1.2348	1600	30	100

Source: Author.

Aiming to operate wind turbine with its best performance, as cited in chapter 5, it is necessary to control the current draw by converter. This control is made utilizing a PI controller, which its reference current is calculated according to an available torque. This torque is proportional to square of rotational speed by a constant defined in equation (5.69).

From aerodynamic results, the maximum power coefficient is about 0.3972 for $\lambda = 1.9$. So, it is possible to obtain the optimal constant K (see equation (5.69)), that relates rotational speed to reference torque, being equal to 0.1889. After that, it is possible

to calculate the reference current (see equation (5.71)) to PI controller. Another PI is utilized to keep capacitor voltage approximately to 600 V.

Also, it is defined that PMSM is rotating at least 60 rpm before power converter starts its operation. This is the minimum speed, according to manufacturer to apply torque without making the turbine stop for a reasonable wind speed.

Figures 6.10, 6.11 and 6.12 illustrate the results for the simulation of wind turbine operation with wind speed being 5 m/s (from 0 to 20 seconds), 9 m/s (from 20 to 50 seconds) and finally $12m/s$ (from 50 to 80 seconds).

The generated power defined by P has a compatible behavior when observing Figure 4.7. The differences can be related to optimal constant, calculated based on aerodynamic simulation or small variations on parameters of PMSM measured as described in chapter 4. Looking at Figure 6.11, both estimated $\alpha\beta$ currents and estimated $\alpha\beta$ EMF are in same shape with their based variables, resulting in a good evaluation for observed speed and position.

Results associated to maximum power point tracking and v_{dc}, and power transferred to load are presented in Figure 6.12. Measured torque F_{torque} and estimated torque $\widehat{F}_{torque}$ seem to converge to the same point. The reference torque given by F^{ref}_{torque} is smaller than others, and it is correct, because it is necessary to keep the torque applied to PMSM by boost converter through current control, lower than torque applied by wind to blades in order to the wind turbine to be kept rotating and producing energy. Regarding transferring power to load, capacitor voltage must be kept in 600 V, allowing to extract the better performance as possible. In this simulation, a resistor (240Ω) is used as load to be supplied.

6.4 EXPERIMENTAL STUDIES

Below, experimental results about speed observer and performance analysis of the studied VAWT are presented. Data were recorded according to IEC 61400-12-1, hence database sample frequency is 1 Hz, the average values for power curve are divided by minute and the bins of speed are separate into intervals by 0.5 m/s.

6.4.1 Rotational speed observer

The generator speed was checked by comparing the line voltage frequency and estimated speed, by converting line voltage frequency from Hz to rpm. The test lasted approximately 10 minutes. The applied gains were defined as given in Table 6.2 by simulation and practical tests. The average wind speed during the test was about 2.7

Figure 6.10 – Line/phase voltages, phase currents and generated power.

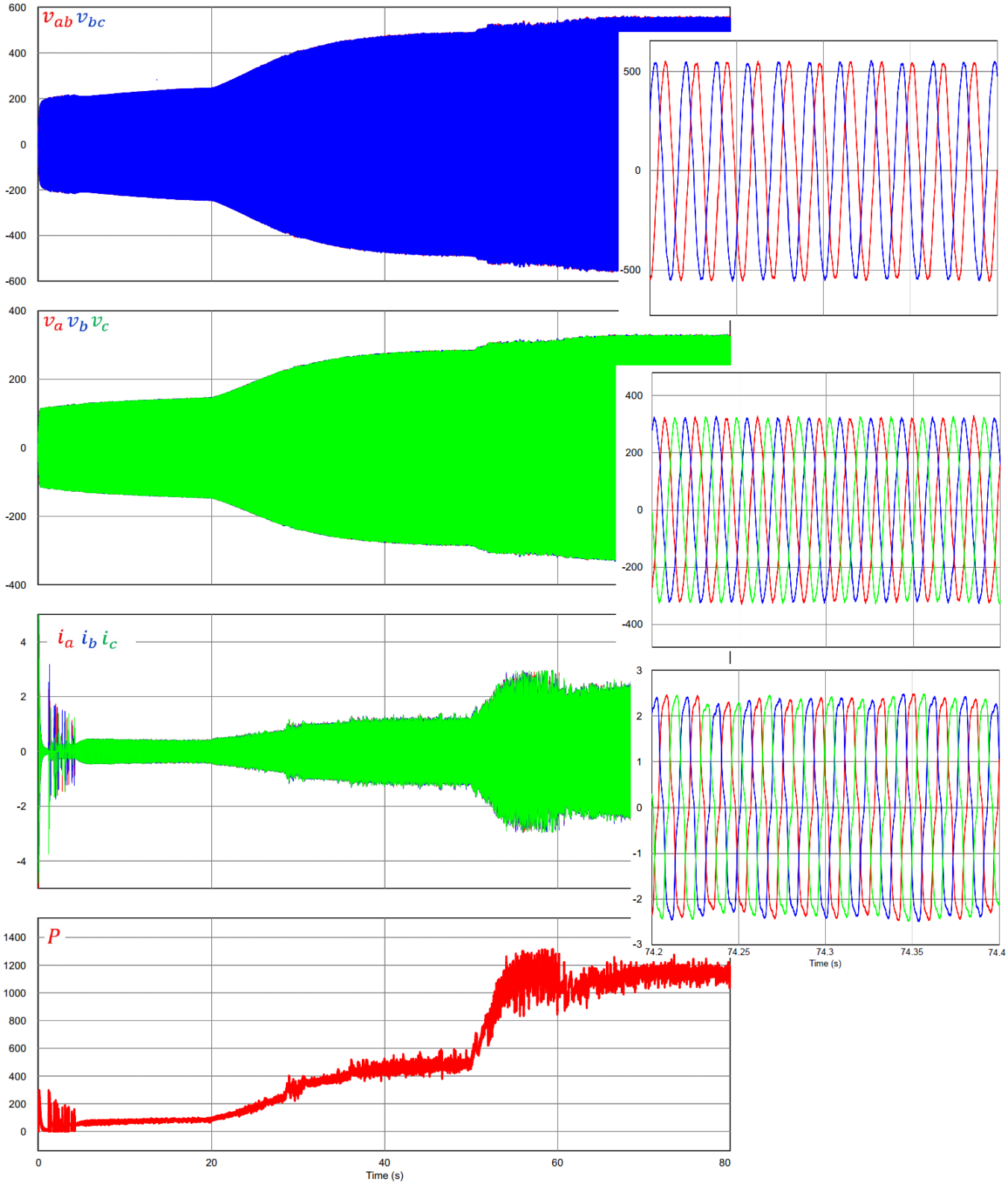

Source: Author.

Figure 6.11 – Observed currents/EMF/Speed/Position.

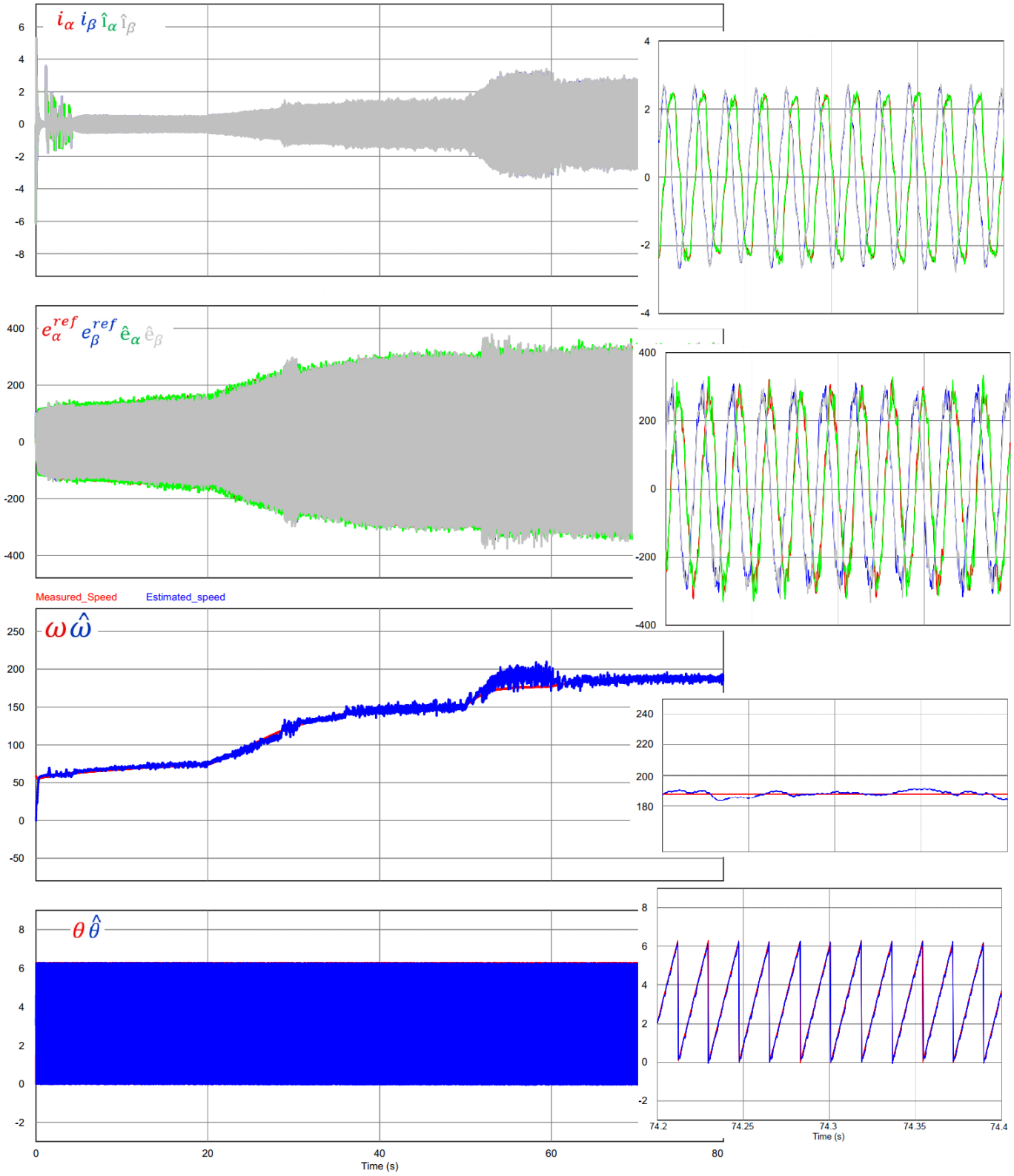

Source: Author.

Figure 6.12 – MPPT, capacitor voltage and power at load.

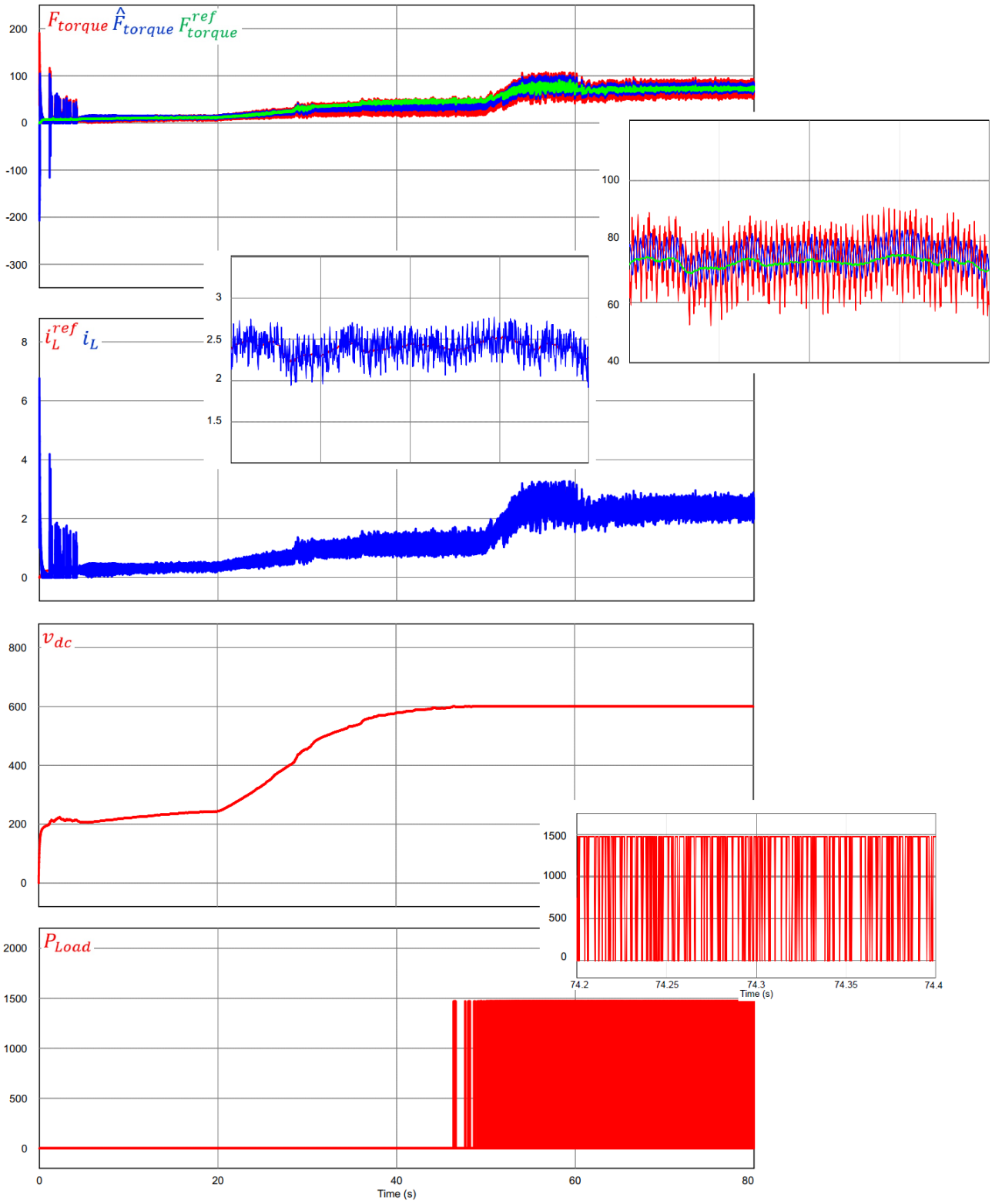

Source: Author.

m/s. Figure 6.13 illustrates this comparison, and it is noticed that these curves present a correspondence. Perhaps, differences between them could be associated with some harmonics as saw between 14:59 and 15:00.

Table 6.2 – Practical speed observer gains.

h_1	h_2	h_3	f_1	f_2	Q
2.0	1.0	1.03	1600	30	100

Source: Author.

Figure 6.13 – Speed observer verification (November, 21, 2018).

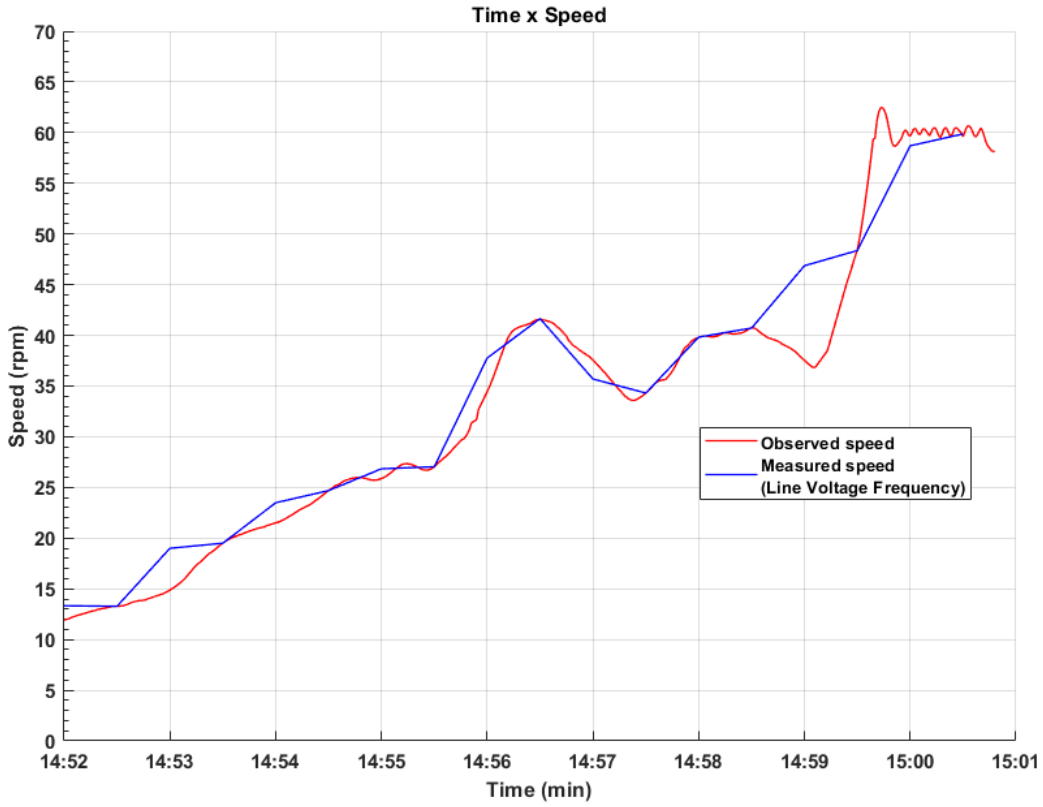

Source: Author.

6.4.2 Output power test

As described in chapter 4, the site where the wind turbine is installed presents average wind speed about 2.2 m/s along the year. Occasionally, during the year, winds of 5,6 until 7 m/s could occur at short periods. Considering that issue, Figure 6.14 shows the dispersal curves for average, maximum, minimum and standard deviation. Comparing Figures 6.14 and 6.15, it is realized a tendency related to the average values. As the wind

speed rises both curves show similar results. The standard deviation can be considered high, due to low number of measures.

Figure 6.14 – Dispersal curve (Air density 1.225 kg/m^3).

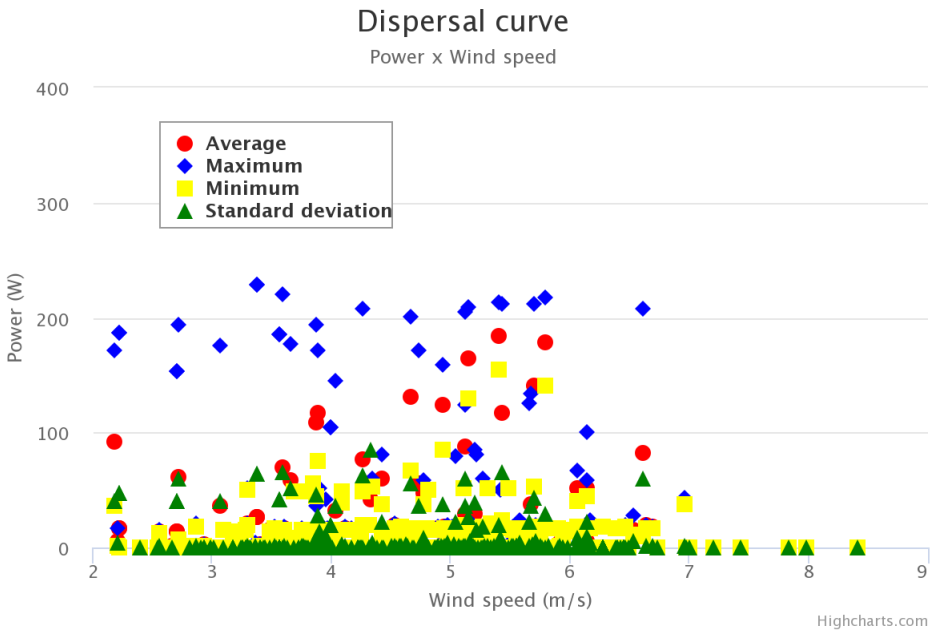

Source: Author.

Figure 6.15 – Manufacturer power curve of wind turbine.

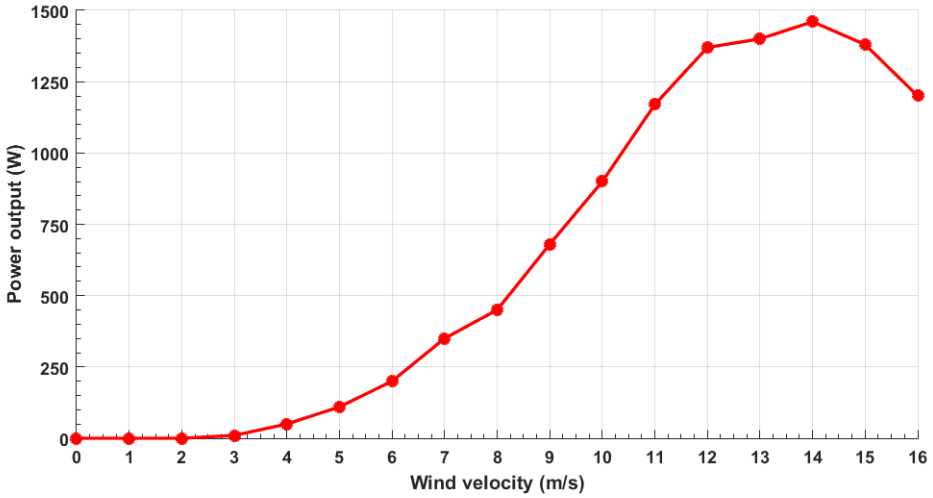

Source: Adapted from (ENERSUD, 2017).

Figure 6.16 illustrates the average output power for various wind speeds. Each speed/power pair is resultant from the average of interval $X - 0.25$ to $X + 0.25$. For instance, look at wind speed 4.5041 m/s, the values that compose this average are between 4.25 m/s and 4.75 m/s.

Figure 6.16 – Power coefficient curve (Air density 1.225 kg/m^3).

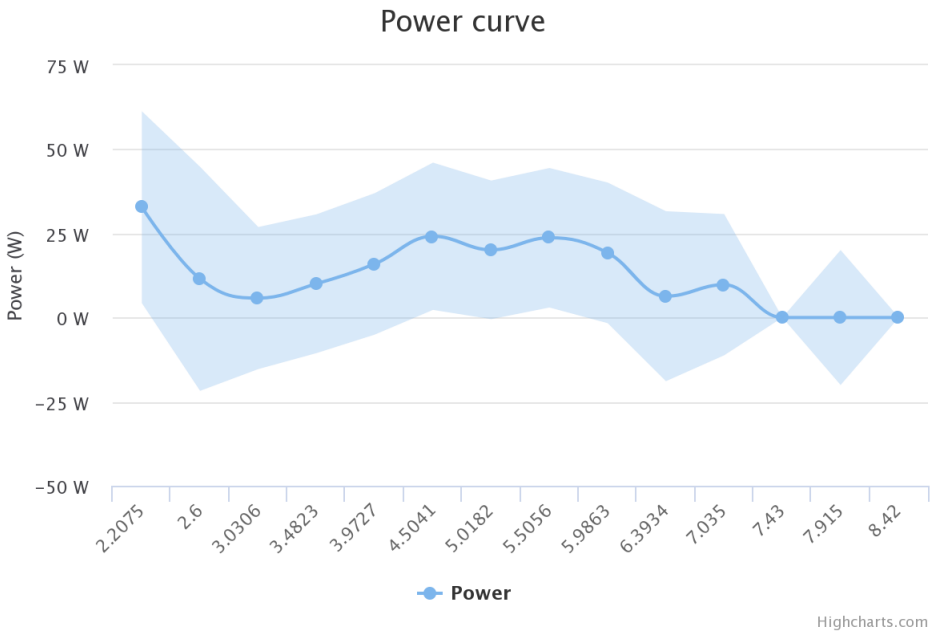

Source: Author.

The last result to be presented is the estimation of how much power, during a year, this turbine is supposed to generate. Figure 6.17 shows this prediction from 4 m/s to 11 m/s. The Annual Energy Production (AEP) is showed lower than expected. However, this is related to low number of acquired points, so the expectation is that the numbers will get higher then now, and then, allowing a better analysis about it.

Figure 6.17 – Annual energy production (Air density 1.225 kg/m^3 and cut-off speed 14 m/s).

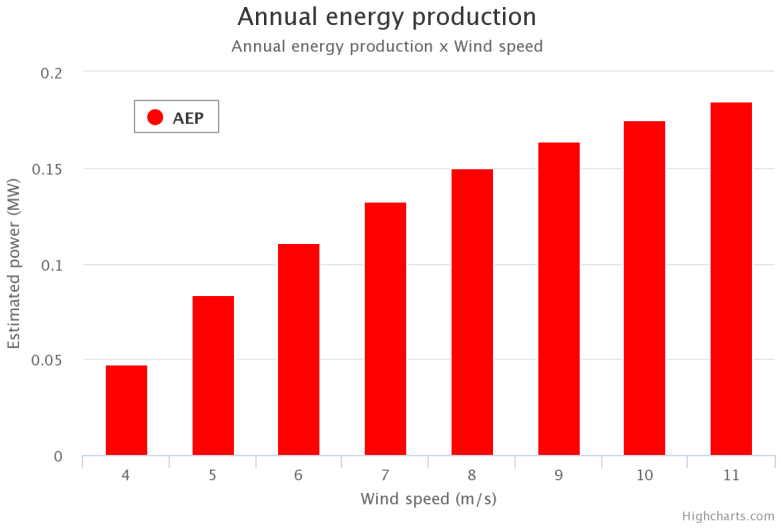

Source: Author.

6.5 CONCLUSION

In this chapter, the results for simulation about aerodynamic model and power converter control and experimental tests were presented. About aerodynamic simulation, it was observed the strong influence of tip speed ratio and induced velocity into angle of attack, torque and coefficient of power. The start-up characteristic could be observed for tip speed ratio 1.5. Regarding the overestimation associated with power coefficient 0.3972 (simulated) to 0.3132 (manufacturer), it is possibly due to having no losses related to mechanical structure, generator and power converter during the simulations. Also, it is necessary to address that the lack of information about the complete aerodynamic profile coefficients result in abrupt variations mainly between 270 to 360 degrees in all variables.

The results from the simulation of power converter illustrate the operation of wind turbine for three different phases: starting, middle range and nominal power. The generated power have presented good agreement with manufacturer data. The differences might be attached to parameter variations or the calculated optimal constant. The PMSM speed estimation followed the real one for the whole period, just presenting a small mismatching at some point, because of the abrupt variation in wind speed or some harmonics in the signal. Finally, the MPPT method applied has worked as projected, never demanding more current than the one applied by the wind.

Regarding the experimental results, it is possible to observe a tendency on the performance of VAWT when comparing the manufacturer power curve and dispersal curve. However, more data is necessary to give a consolidated conclusion for the power curve and annual energy production. About speed observer, there is a good agreement between observed speed and measured speed (Line Voltage Frequency).

7 FINAL REMARKS

This work aimed to develop a control system for evaluating a 1.5 kW VAWT performance and then, to do a comparison among experimental test, aerodynamic analysis and power electronic simulation.

A studied about VAWT designs was presented, highlighting their main features and how they developed in relation to their power coefficient. The study also shows the most relevant ways to improve VAWT performance by doing changes in parameters, such as solidity, aspect ratio, chord length, number of blades, tip speed ratio, starting torque; evaluating different airfoil profiles; adding mechanism to the blades to control airflow through themselves or use turbine's generator to start wind turbine at very low winds. Regarding what is the best place to install a VAWT, integrate them to buildings in urban areas seems to be a good possibility for small vertical axis wind turbines, because it is near the consumer and they take advantage of faster wind while reducing costs of support towers. Also, there is possibility to exploit the acceleration of the air flow on the upper corners and the sides of the buildings. Other important issue is the fact that the wind is turbulent in urban environments, and this is suitable for VAWT.

From aerodynamic simulation, it was possible to study how wind speed acts through the rotor by the induced velocity and the induction factor. They are important variables because they influence all inner rotor velocities and forces on blades, as well as power performance. The tip speed ratio between 1.5 and 3 was set to stay inside valid values of lift and drag coefficient, operating in linear zones for all azimuthal angles, as illustrated in effective angle of attack. Also, it is realised that this turbine can start up by itself due to the torque coefficient being average positive at low tip speed ratios. About power coefficient curve, it makes sense that the efficiency in the front part of the rotor is higher than efficiency in back part of the rotor. That characteristic is strictly associated with the induction factor. The fact that the power coefficient presents itself higher, 0.3972, than what presented in chapter 4, 0.3132, is possibly due to, in simulation, there were no losses related to mechanical aspects, wake effect, PMSM and power converter. It is necessary to address that the lack of information about the complete aerodynamic profile coefficients result in abrupt variations and convergence problems mainly between 270 to 360 degrees in all variables. This might be solved by doing a further numerical airfoil catalogue including 360° airfoil polars.

About the simulation of the control scheme, it possible to conclude that the generated power has presented good agreement with manufacturer data. The differences might be attached to parameter variations or the calculated optimal constant. The PMSM speed estimation followed the real one for the whole period, just presenting small mismatching at some point because the abrupt variation in wind speed. Finally, the MPPT method applied has worked as projected, never demanding more current than the one applied by

the wind.

In relation to experimental results, the speed predicting was presented for at least ten minutes and compared with line voltage frequency. This comparison just was possible because it was used an resistive load, so that there is no delay between voltage and current. Otherwise, it would necessary measure the phase current frequency. About output power test, it was observed a tendency about the performance of VAWT when comparing manufacturer power curve and dispersal curve for speeds around 5 m/s, 6 m/s and 7 m/s. The power curve and AEP presented lower values than expected. These results were harmed because site average wind speed is not high as cited before, in addition there is a necessity to acquire more data, then reducing elevated uncertainty presented in power curve and annual energy production.

Regarding experimental results, the speed predicted was presented for at least ten minutes and compared to voltage line frequency. This comparison could only be effective because a resistive load was used, so that there is no delay between voltage and current. Otherwise, it would be necessary to measure the phase current frequency. About output power test, it was observed a tendency about the performance of VAWT when comparing manufacturer power curve and dispersal curve for speeds around 5 m/s, 6 m/s and 7 m/s. The power curve and AEP presented lower values than expected. These results were harmed because the site average wind speed is not high as cited before, in addition, there is a necessity to acquire more data, then reducing elevated uncertainty presented in power curve and annual energy production.

7.1 FURTHER WORKS

- Test other aerodynamic method and compare their efficiency;
- Establish a model, combining mechanical and electrical parts;
- Pitch angle evaluation in aerodynamic simulation;
- Test other control techniques;
- Connect VAWT to the grid and battery bank;
- Apply VAWT's generator as motor to studied how this affect the dynamic at start up.

7.2 PUBLISHED PAPERS

During this work the follow papers have been published, related or not with the thesis theme:

- RAMOS, A. J. et al. *Ensaio de aerogerador de 3 kW segundo normal IEC 61400-12-1.* **Brazil Windpower**, 2017.
- TESTON, S. A.; RAMOS, A. J.; RECH, C. *Inversor multinível com capacitor flutuante para conexão de geração fotovoltaica e banco de baterias à rede.* **Seminar on Power Electronics and Control**, 2017.
- RAMOS, A. J. et. al. Performance simulation of vertical axis wind turbine. ***Congresso Nacional de Engenharia Mecânica***, 2018.

REFERENCES

ABU-EL-YAZIED, T. G. et al. Effect of number of blades and blade chord length on the performance of darrieus wind turbine. **American Jounal of Mechancal Enginnering and Automation**, v. 2, n. 1, p. 16–25, 2015.

AGGRAWAL, A. Optimization of vertical axis wind turbine on individual blade pitch control. **Journal of Chemical and Pharmaceutical Sciences**, v. 9, n. 4, dez. 2016. ISSN 0974-2115.

AHMADI, F. **VAWT wind turbine what are the 3 biggest pros**. 2012. Http://maketurbine.blogspot.com/2012/12/vawt-wind-turbine-what-are-3-biggest.html.

AMBROSIO, M. D.; MEDAGLIA, M. **Vertical Axis Wind Turbines: History, Technology and Applications**. Dissertação (Mestrado) — Halmstad University, 2010.

ANAYA-LARA, O. et al. **Wind Energy Generation: Modelling and Control**. [S.l.]: John Wiley & Sons, Ltd., 2009.

ARMSTRONG, S.; FIEDLER, A.; TULLIS, S. Flow separation on a high reynolds number, high solidity vertical axis wind turbine with straight and canted blades and canted blades with fences. **Renewable Energy**, Elsevier BV, v. 41, p. 13–22, may 2012.

ASHWILL, T. D.; SUTHERLAND, H. J.; BERG, D. E. **A retrospective of VAWT technology.** [S.l.], 2012.

ASR, M. T. et al. Study on start-up characteristics of h-darrieus vertical axis wind turbines comprising NACA 4-digit series blade airfoils. **Energy**, Elsevier BV, v. 112, p. 528–537, oct 2016.

AYMANE, E. Savonius vertical wind turbine: Design, simulation, and physical testing. Graduation work. 2017.

BATTISTI, L. et al. Analysis of different blade architectures on small VAWT performance. **Journal of Physics: Conference Series**, IOP Publishing, v. 753, p. 062009, sep 2016.

BELLER, C. **Urban Wind Energy**. Tese (phdthesis) — Technical University of Denmark, 2011.

BERG, D. E. Improved double-multiple-streamtube model for the darrieus-type vertical-axis wind turbine. **Am. Solar Energy Soc. Meeting**, v. 1, jun. 1983.

_____. Vertical-axis wind turbines – the current status of an old technology. 1996.

BERNARDES, T. et al. Discrete-time sliding mode observer for sensorless vector controle of permanent magnet synchronous machine. **IEEE Transactions on Industrial Electronics**, v. 61, n. 4, abr. 2014.

BHUTTA, M. M. A. et al. Vertical axis wind turbine - a review of various configurations and design techniques. **Renewable and Sustainable Energy Reviews**, Elsevier BV, v. 16, n. 4, p. 1926–1939, may 2012.

BIADGO, A. M. et al. Numerical and analytical invertigation of vertical axis wind turbine. **FME Transactions**, v. 41, p. 49–58, dez. 2013.

BOATNER, B. **A Summary Overview of the Blackhawk Wind Turbine**. [S.l.], 2010.

BOBEK, V. **PMSM Electrical Parameters Measurement**. Rev. 0. [S.l.], 2013.

BOLDEA, I. **Variable Speed Generators**. [S.l.]: CRC Press, 2005.

BOUZAHER, M. T.; HADID, M. Active control of the vertical axis wind turbine by the association of flapping wings to their blades. **Procedia Computer Science**, Elsevier BV, v. 52, p. 714–722, 2015.

CASINI, M. Small vertical axis wind turbines for energy efficiency of buildings. **Journal of Clean Energy Technologies**, EJournal Publishing, v. 4, n. 1, p. 56–65, 2016.

CHOUGULE, P.; NIELSEN, S. Overview and design of self-acting pitch control mechanism for vertical axis wind turbine using multi body simulation approach. **Journal of Physics: Conference Series**, IOP Publishing, v. 524, p. 012055, jun 2014.

CLARKE, E. **Circuit Analysis of A-C Power System**. third. [S.l.]: John Wiley & Sons, Inc, 1948. v. 1.

DANAO, L. A.; EBOIBI, O.; HOWELL, R. An experimental investigation into the influence of unsteady wind on the performance of a vertical axis wind turbine. **Applied Energy**, Elsevier BV, v. 107, p. 403–411, jul 2013.

Georges Jean Marie Darrieus. **Turbine Having Its Rotationg Shaft Transverse To the Flow Of The Current**. 1931. 1835018.

DEBNATH, B. K.; BISWAS, A.; GUPTA, R. Computational fluid dynamics analysis of a combined three-bucket savonius and three-bladed darrieus rotor at various overlap conditions. **Journal of Renewable and Sustainable Energy**, AIP Publishing, v. 1, n. 3, p. 033110, may 2009.

DOUAK, M.; AOUACHRIA, Z. Starting torque study of darrieus wind turbine. **International Journal of Physical and Mathematical Sciences**, v. 9, n. 8, 2015.

DRAGOMIRESCU, A. Performance assessment of a small wind turbine with crossflow runner by numerical simulations. **Renewable Energy**, Elsevier BV, v. 36, n. 3, p. 957–965, mar 2011.

ELLIOTT, D. Assessing the world's wind resources. In: **2002 IEEE Power Engineering Society Winter Meeting. Conference Proceedings (Cat. No.02CH37309)**. [S.l.]: IEEE, 2002.

ENERSUD. **Manual of Instructions of Vertical Turbine Razec**. [S.l.], 2017.

ERIKSSON, S.; BERNHOFF, H.; LEIJON, M. Evaluation of different turbine concepts for wind power. **Renewable and Sustainable Energy Reviews**, Elsevier BV, v. 12, n. 5, p. 1419–1434, jun 2008.

FERREIRA, C. S. et al. Visualization by PIV of dynamic stall on a vertical axis wind turbine. **Experiments in Fluids**, Springer Nature, v. 46, n. 1, p. 97–108, aug 2008.

FUJISAWA, N.; SHIBUYA, S. Observations of dynamic stall on darrieus wind turbine blades. **Journal of Wind Engineering and Industrial Aerodynamics**, Elsevier BV, v. 89, n. 2, p. 201–214, feb 2001.

GMP, G. M. P. L. **Small Wind Turbine Market to be Worth 1.79 Billion by 2025**. 2017.

GORELOV, D. N.; KRIVOSPITSKY, V. P. Prospects for development of wind turbines with orthogonal rotor. **Thermophysics and Aeromechanics**, Pleiades Publishing Ltd, v. 15, n. 1, p. 153–157, mar 2008.

Alexander M. Gorlov. **Unidirectional helical reaction turbine operable under reversible fluid flow for power systems**. 1995. 5,451,137.

GORMONT, R. E. **A Mathematical Model of Unsteady Aerodynamics and Radial Flow for Application to Helicopter Rotors**. [S.l.], 1973.

GUPTA, R.; DAS, R.; SHARMA, K. K. Experimental study of a savonius-darrieus wind machine. **International Conference on Renewble Energy for Developing Contries**, 2006.

GWEC. **Global Wind Statistics 2017**. [S.l.], 2018.

HAMEED, M. S.; AFAQ, S. K. Design and analysis of a straight bladed vertical axis wind turbine blade using analytical and numerical techniques. **Ocean Engineering**, Elsevier BV, v. 57, p. 248–255, jan 2013.

HANSEN, M. O. L. **Aerodynamics of Wind Turbines**. [S.l.]: Routledge, 2015. ISBN 978-1-138-77507-7.

HAQUE, M. E.; NEGNEVITSKY, M.; MUTTAQI, K. M. A novel control strategy for a variable speed wind turbine with a permanent magnet synchronous generator. In: **2008 IEEE Industry Applications Society Annual Meeting**. [S.l.]: IEEE, 2008.

HEIER, S. Wind power [a review of grid integration of wind energy conversion systems (s. heier 2006) book review]. **IEEE Power and Energy Magazine**, Institute of Electrical and Electronics Engineers (IEEE), v. 6, n. 3, p. 95–97, may 2008.

HOGBERG, L. **Automated electric control of a vertical axis wind turbine in island operation**. Tese (phdthesis) — Uppsala Universitet, fev. 2009.

HUI, J.; BAKHSHAI, A. A new adaptive control algorithm for maximum power point tracking for wind energy conversion systems. In: **2008 IEEE Power Electronics Specialists Conference**. [S.l.]: IEEE, 2008.

IEC. **Wind energy generation systems - Part 12-1: Power performance measurements of electricity producing wind turbines**. [S.l.], 2017.

INSTITUTE, A. 2018.

ISLAM, M. et al. Designing straight-bladed vertical axis wind turbine using the cascade theory. **12th AIAA/ISSMO Multidisciplinary Analysis and Optimization Conference**, p. 10–12, set. 2008.

ISLAM, M.; TING, D.; FARTAJ, A. Aerodynamic models for darrieus-type straight-bladed vertical axis wind turbines. **Renewable and Sustainable Energy Reviews**, Elsevier BV, v. 12, n. 4, p. 1087–1109, maio 2008.

JAIN, P.; ABHISHEK, A. Performance prediction and fundamental understanding of small scale vertical axis wind turbine with variable amplitude blade pitching. **Renewable Energy**, Elsevier BV, v. 97, p. 97–113, nov 2016.

JAMIESON, P. **Innovation in Wind Turbine Design**. Wiley, 2011. ISBN 978-0-470-69981-2. Disponível em: <https://www.amazon.com/Innovation-Turbine-Design-Peter-Jamieson/dp/0470699817?SubscriptionId=AKIAIOBINVZYXZQZ2U3A&tag=chimbori05-20&linkCode=xm2&camp=2025&creative=165953&creativeASIN=0470699817>.

JEONG, H. G.; SEUNG, R. H.; LEE, K. B. An improved maximum power point tracking method for wind power systems. **Energies**, MDPI AG, v. 5, n. 5, p. 1339–1354, may 2012.

JI, X.; SCHLUTER, J. Design and analysis of small-scale vertical axis wind turbine. In: **IET Conference on Renewable Power Generation (RPG 2011)**. [S.l.]: IET, 2011.

JIN, X. et al. Darrieus vertical axis wind turbine: Basic research methods. **Renewable and Sustainable Energy Reviews**, v. 42, p. 212–225, fev. 2015. Elsevier BV.

KIRKE, B. K. **Evaluation of Self-Starting Vertical Axis Wind Turbines For Stand-Alone Applications**. Tese (Doutorado) — Griffith University, 1998.

KJELLIN, J. **Vertical Axis wind Turbines**. Tese (phdthesis) — Uppsala University, nov. 2012.

KOCH, G. et al. Sensorless technique applied to pmsg of wecs using sliding mode observer. **Power Electronics Conference and 1st Southern Power Electronics Conference (COBEP/SPEC), 2015 IEEE 13th Brazilian**, 2015.

KORPRASERTSAK, N.; LEEPHAKPREEDA, T. Analysis and optimal design of wind boosters for vertical axis wind turbines at low wind speed. **Journal of Wind Engineering and Industrial Aerodynamics**, Elsevier BV, v. 159, p. 9–18, dec 2016.

KOUTROULIS, E.; KALAITZAKIS, K. Design of a maximum power tracking system for wind-energy-conversion applications. **IEEE Transactions on Industrial Electronics**, Institute of Electrical and Electronics Engineers (IEEE), v. 53, n. 2, p. 486–494, apr 2006.

KOZAC, P. A.; VALLVERDU, D. Modeling vertical-axis wind turbine performance: Blade element method vs. finite volume approach. **12th International Energy Conversion Engieering Conference**, jul. 2014.

KRISHNAN, R. **Permanent Magnet Synchronous and Brushless DC Motor Drives (Mechanical Engineering (Marcel Dekker))**. CRC Press, 2009. ISBN 978-0-8247-5384-9. Disponível em: <https://www.amazon.com/Permanent-Synchronous-Brushless-Mechanical-Engineering-ebook/dp/B00866H3NM?SubscriptionId=0JYN1NVW651KCA56C102&tag=techkie-20&linkCode=xm2&camp=2025&creative=165953&creativeASIN=B00866H3NM>.

LAPLIN, E. E. Theoretical performance of vertical axis wind turbines. **ASME paper, 75-WA/Ener-1. Houston, TX, USA: The Winter Annual Meeting**, 1975.

LAZAUSKAS, L. Three pitch control systems for vertical axis wind turbines compared. **Wind Engineering**, v. 16, n. 5, 1992.

LI, H.; SHI, K.; MCLAREN, P. Neural network based sensorless maximum wind energy capture with compensated power coefficient. In: **Conference Record of the 2004 IEEE Industry Applications Conference, 2004. 39th IAS Annual Meeting.** [S.l.]: IEEE, 2005.

LI, Q. et al. Study on power performance for straight-bladed vertical axis wind turbine by field and wind tunnel test. **Renewable Energy**, Elsevier BV, v. 90, p. 291–300, may 2016.

LIANG, Y. bin et al. Blade pitch control of straight-bladed vertical axis wind turbine. **Journal of Central South University**, Springer Nature, v. 23, n. 5, p. 1106–1114, may 2016.

MANWELL, J. F.; MCGOWAN, J. G.; ROGERS, A. L. **Wind Energy Explained: Theory, Design and Application**. Wiley, 2010. ISBN 978-0-470-01500-1. Disponível em: <https://www.amazon.com/Wind-Energy-Explained-Theory-Application/dp/0470015004?SubscriptionId=0JYN1NVW651KCA56C102&tag=techkie-20&linkCode=xm2&camp=2025&creative=165953&creativeASIN=0470015004>.

MARQUES, T. A. dos S. **Control and Operation of a Vertical Axis Wind Turbine**. Dissertação (mathesis) — TÃ©cnico Lisboa, nov. 2014.

MASTERS, G. M. **Renewable and Efficient Electric Power Systems**. [S.l.]: John Wiley & Sons, Inc., 2004.

MCCONNELL, R. D. **Giromill Overview**. [S.l.], 1979.

MCLAREN, K.; TULLIS, S.; ZIADA, S. Measurement of high solidity vertical axis wind turbine aerodynamic loads under high vibration response conditions. **Journal of Fluids and Structures**, Elsevier BV, v. 32, p. 12–26, jul 2012.

MERTENS, S. The energy yield of roof mounted wind turbines. **Wind Engineering**, v. 27, n. 6, p. 507–518, 2003.

MIAU, J. et al. Design and test of a vertical-axis wind turbine with pitch control. **Applied Mechanics and Materials**, Trans Tech Publications, v. 225, p. 338–343, nov 2012.

MOLINA, M. G.; MERCADO, P. E. A new control strategy of variable speed wind turbine generator for three-phase grid-connected applications. In: **2008 IEEE/PES Transmission and Distribution Conference and Exposition: Latin America**. [S.l.]: IEEE, 2008.

MULLER, G.; JENTSCH, M. F.; STODDART, E. Vertical axis resistance type wind turbines for use in buildings. **Renewable Energy**, Elsevier BV, v. 34, n. 5, p. 1407–1412, may 2009.

NEMOTO, Y.; ANZAI, A.; USHIYAMA, I. A study of the twisted sweeney-type wind turbine. **Wind Engineering**, v. 27, n. 4, p. 317–322, 2003.

NICOLINI, A. M. **Desenvolvimento de um Sistem de Controle e Supervisao de Inversor para Turbinas Eolicas**. Dissertação (mathesis) — Universidade Federal de Santa Maria, fev. 2017.

OKPUE, A. S. **Aerodynamic analysis of vertical and horizontal axis wind turbines**. Dissertação (mathesis) — Michigan State University, 2011.

PARASCHIVOIU, I. Double-multiple streamtube model for darrieus wind turbines. **Second DOE/NASA wind turbines dynamics workshop, NASA CP-2186**, p. 19–25, fev. 1981.

PARASCHIVOIU, I.; TRIFU, O.; SAEED, F. H-darrieus wind turbine with blade pitch control. **International Journal of Rotating Machinery**, Hindawi Limited, v. 2009, p. 1–7, 2009.

PARFIT, M.; LEEN, S. Powering the future. **National Geographic**, 2005.

PARK, R. H. Two-reation theory of synshonous machines. **American Institute of Electrical Engineers**, v. 48, n. 3, p. 716 – 727, jul. 1929. ISSN 0096-3860.

PRICE, T. J. Uk large-scale wind power programme from 1970 to 1990: The carmarthen bay experiments and the musgrove vertical-axis turbines. **Wind Engineering**, SAGE Publications, v. 30, n. 3, p. 225–242, may 2006.

RATHOD, P. et al. A review on combined vertical axis wind turbine. **International Journal of Innovative Research in Science, Engineering and Technology**, v. 5, n. 4, abr. 2016.

REUK. **Savonius Wind Turbine**. 2006.

REYALA, A. S. A. **Load Reduction in wind Energy Converters Using Individual Pitch Control**. Dissertação (mathesis) — The Islamic University of Gaza Deanery of Graduate Studies Faculty of Electrical Engineering Department, maio 2012.

RISHMANY, J. et al. Optimization of a vertical axis wind turbine using fea, multibody dynamics and wind tunnel testing. **Athens Journal of Technology and Engineering**, 2017.

S., R.; UK, S. Review on the numerical inverstigations into the design and development of savonius wind rotors. **Reneawable Sustainable energy**, 2013.

SARPTURK, S.; ISTEFANOPULOS, Y.; KAYNAK, O. On the stability of discrete-time sliding mode control systems. **IEEE Transactions on Automatic Control**, Institute of Electrical and Electronics Engineers (IEEE), v. 32, n. 10, p. 930–932, oct 1987.

Sigurd Johannes Savonius. **Rotor Adapted To Be Driven By Wind Or Flowing Water**. 1929. 1697574.

Sigurd J. Savonius. **Wind Rotor**. 1930. 1766765.

SCHEURICH, F. **Modelling the aerodynamics of vertical-axis wind turbines**. Tese (phdthesis) — University of Glasgow, set. 2011.

SCHUBERT, C.; ELETROSUL. **Atlas Eolico**. [S.l.], 2014.

SHIRES, A. Design optimisation of an offshore vertical axis wind turbine. **Proceedings of the Institution of Civil Engineers - Energy**, Thomas Telford Ltd., v. 166, n. 1, p. 7–18, feb 2013.

SINGH, M.; BISWAS, A.; MISRA, R. Investigation of self-starting and high rotor solidity on the performance of a three s1210 blade h-type darrieus rotor. **Renewable Energy**, Elsevier BV, v. 76, p. 381–387, apr 2015.

STRICKLAND, J. H. A performance prediction model for the darrieus turbine. **International symposium on wind energy systems, Cambridge, UK**, p. 39–54, set. 1976.

SUNNY, K. A.; KUMAR, N. M. Vertical axis wind turbine: Aerodynamic modelling and its testing in wind tunnel. **Procedia Computer Science**, Elsevier BV, v. 93, p. 1017–1023, 2016.

SVENDSEN, H. G.; MERZ, K. O. Control system for start-up and shut-down of a floating vertical axis wind turbine. **Energy Procedia**, Elsevier BV, v. 35, p. 33–42, 2013.

TAFTICHT, T.; AGBOSSOU, K.; CHERITI, A. DC bus control of variable speed wind turbine using a buck-boost converter. In: **2006 IEEE Power Engineering Society General Meeting**. [S.l.]: IEEE, 2006.

TCHAKOUA, P. et al. A new approach of rmodelling darrieus-type vertical axis wind turbine rotors using electrical equivalent circuit analogy: Basis of theoretical formulations and model development. **Energies**, 2015.

TEMPLIN, R. J. **Aerodynamic performance theory for the NRC vertical-axis wind turbine**. [S.l.], 1974.

TESCIONE, G. et al. Near wake flow analysis of a vertical axis wind turbine by stereoscopic particle image velocimetry. **Renewable Energy**, Elsevier BV, v. 70, p. 47–61, oct 2014.

THOENNISEN, F. et al. A numerical analysis to evaluate betz's law for vertical axis wind turbines. **Journal of Physics: Conference Series**, IOP Publishing, v. 753, p. 022056, sep 2016.

THOMSEN, S.; NIEMANN, H.; POULSEN, N. Individual pitch control of wind turbines using local inflow measurements. **IFAC Proceedings Volumes**, Elsevier BV, v. 41, n. 2, p. 5587–5592, 2008.

TJIU, W. et al. Darrieus vertical axis wind turbine for power generation i: Assessment of darrieus VAWT configurations. **Renewable Energy**, Elsevier BV, v. 75, p. 50–67, mar 2015.

VAAHEDI, E.; BARNES, R. Dynamic behaviour of a 25m variable-geometry vertical-axis wind-turbine generator. **IEE Proc.**, v. 129, n. 6, nov. 1982.

VALLVERDU, D. **Study on Vertical-Axis Wind Turbine Using Streamtube and Dynamic Stall Models**. [S.l.], 2014.

VANDENBERGHE, D.; DICK, E. A free vortex simulation method for the straight bladed vertical axis wind turbine. **Journal of Wind Engineering and Industrial Aerodynamics**, Elsevier BV, v. 26, n. 3, p. 307–324, jan 1987.

WILSON, R. E.; LISSAMAN, P. B. S.; WALKER, S. N. **Aerodynamic Performance of Wind Turbines**. [S.l.: s.n.], 1976.

WINDPOWER.ORG, D. W. I. A. The wind energy pioneer - poul la cour. **DWIA**, maio 2003.

WOOD, D. **Small Wind Turbines**. Springer Verlag London, 2011. ISBN 1849961743. Disponível em: <https://www.ebook.de/de/product/10394886/david_wood_small_wind_turbines.html>.

WORASINCHAI, S.; INGRAM, G.; DOMINY, R. Unsteady surface pressures and airload of a pitching airfoil. **Energy Procedia**, Elsevier BV, v. 34, p. 407–416, 2013.

YAOQIN, J.; ZHONGQING, Y.; BINGGANG, C. A new maximum power point tracking control scheme for wind generation. In: **Proceedings. International Conference on Power System Technology**. [S.l.]: IEEE, 2002.

APPENDICES

Appendix A – Practical Assembly

A.1 INTRODUCTION

Here, it is described which components the practical assembly was built from. First, the power converter and its control board are presented, and then the developed data communication and acquisition systems, in order to manage all recorded data from weather and electrical and mechanical variables.

A.2 POWER CONVERTER AND CONTROL BOARD

The converter is composed by two IGBT SEMix202GB12E4s modules (see Figure A.1). One is utilized to control the capacitor voltage, and the other is responsible for doing the MPPT. In relation to the measures, it had access to six variables that are two line voltages (LV25-P sensors), two phase currents (LA25-NP sensors), the current on inductor (LA55-P sensor) and the voltage applied to capacitor (LV25-P sensor) and one board to generate PWM signal to switches. The manufactured boards are presented in Figure A.2.

The DSP (Data Signal Processor) used in this work is a C28xTMSF335. It is

Figure A.1 – Power converter.

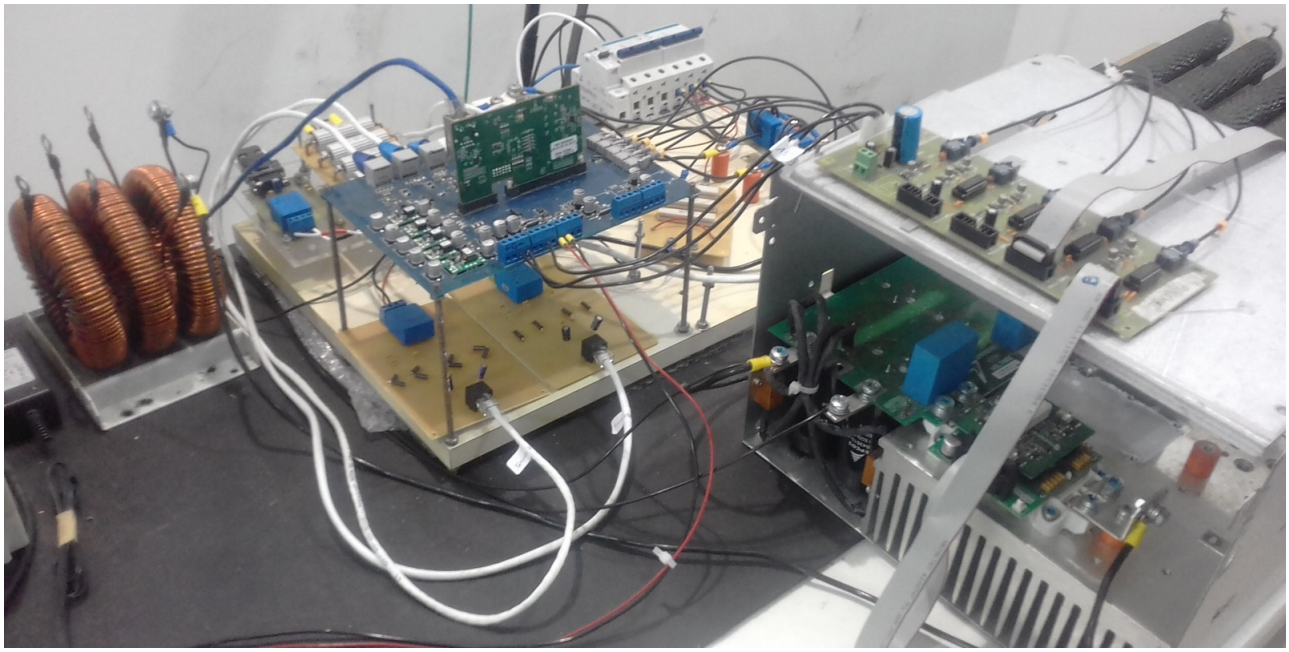

Source: Author.

Figure A.2 – Measuring boards (voltage-left, current-centre, PWM-right).

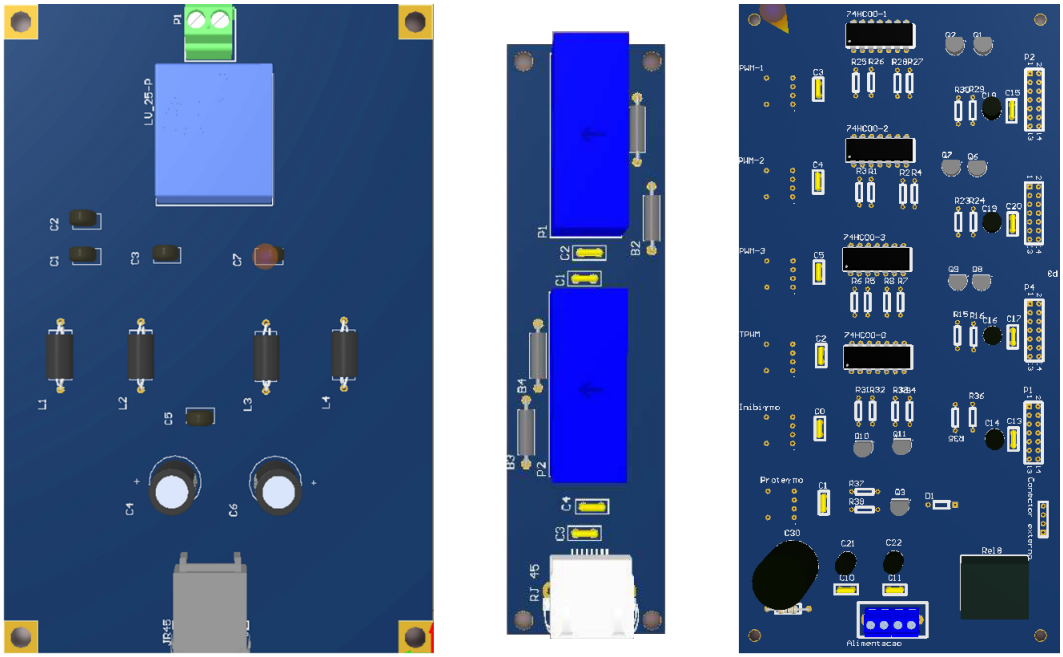

Source: Author.

a dual core microcontroller system-on-chip with independent communication and real time control subsystems, suitable for this project. To connect sensors and actuator to microcontroller it was the board presented in Figure A.3 was employed.

Figure A.3 – Interface board.

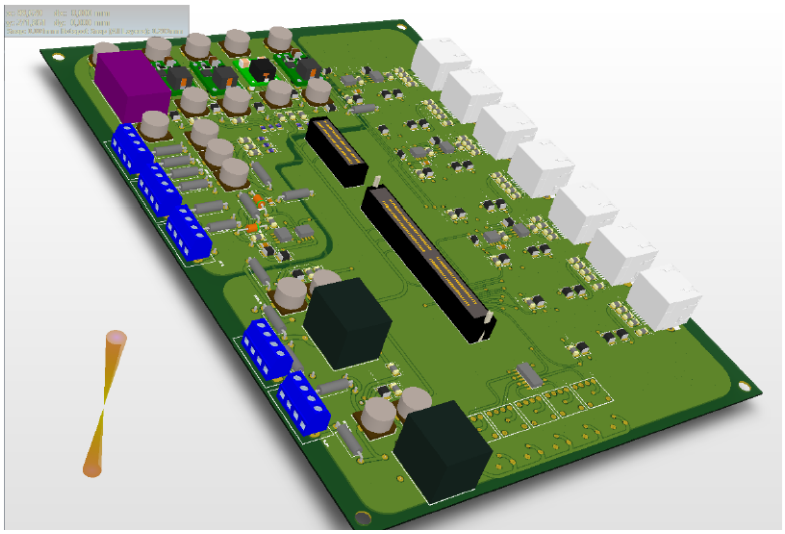

Source: (NICOLINI, 2017).

A.3 DATA COMMUNICATION AND ACQUISITION SYSTEMS

The Figure A.4 presents the diagram of communication scheme where *Process* block represents the turbine and power converter. A weather station was used, in order to measure speed and direction of wind at the turbine hub. The collected data from the weather station was sent to an embedded PC through wireless connection (Modbus TCP/IP protocol); the information from the process, such as voltages, currents, velocity, torque and other status were also sent to the embedded PC from DSP through Ethernet using TCP/IP based protocol.

The data were received by the embedded PC once per second, and saved into a MySQL database. Inside the database, information is separated in maximum, minimum, standard deviation and average, depending on the operation status of the converter and wind turbine. Finally, to present these assembly results, a supervisory using PHP language was developed allowing to see tests results in real time.

Figure A.4 – Data communication system.

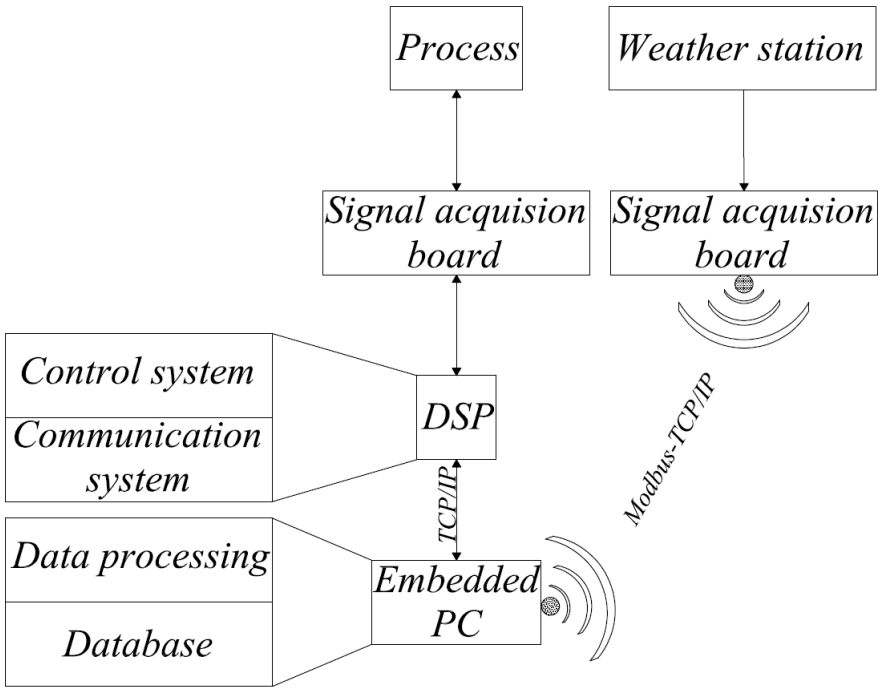

Source: Author.

A.4 CONCLUSION

This appendix presented the system used in order to manage the information on the whole project, and give better understanding about the applied tools in the thesis.